PHYSIK DEPARTMENT

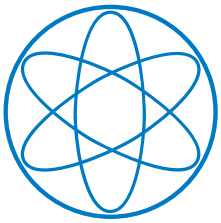

Static and dynamic structure formation of DNA coated colloids far from equilibrium

Dissertation
von

Fabian Hecht

TECHNISCHE UNIVERSITÄT MÜNCHEN

PHYSIK DEPARTMENT
Lehrstuhl für Zellbiophysik - E27

Static and dynamic structure formation of DNA coated colloids far from equilibrium

Fabian M. Hecht

Vollständiger Abdruck der von der Fakultät für Physik der Technischen Universität München zur Erlangung des akademischen Grades eines

Doktors der Naturwissenschaften (Dr. rer. nat.)

genehmigten Dissertation.

Vorsitzender:	Prof. Dr. U. Gerland
Prüfer der Dissertation:	1. Prof. Dr. A. Bausch 2. Prof. Dr. F. Simmel

Die Dissertation wurde am 20.02.2017 bei der Technischen Universität München eingereicht und durch die Fakultät für Physik am 13.04.2017 angenommen.

Abstract

As self-organization of colloidal structures is predicted to result in a myriad of applications, it has become a well-studied approach to create nanoscale colloidal structures under equilibrium conditions. However, as equilibration times scale with the size of the structures, producing mesoscale-sized objects remains a major challenge. In contrast to equilibrium structure formation, structure formation far from equilibrium offers an effective pathway to create self-similar objects, rapidly bridging length scales from the nano- to the meso- and macroscale. In this thesis, a multicomponent system of micrometer-sized DNA coated colloids is used to control and stir the process of diffusion-limited cluster aggregation, a process that is known for its rapid non-equilibrium nature. The specific control over the binding affinities of the components by DNA-hybridization was used to study binary and ternary heterocoagualtion processes that lead to a hierarchical self-organization of a five component system into asymmetric objects. To show the scale-free applicability of the developed approach, nanometer-sized gold particles were assembled into different structures to control the optical properties of the particle dispersion and the macroscopic mechanical properties of polyacrylamide-DNAcc hybrid gels were investigated. In order to render the colloidal structure formation processes dynamic, the enzymes T7 RNA polymerase and RNAseH were deployed. It was shown that the enzymes were able to polymerize and degrade RNA strands to enable formation and disintegration of colloidal structures. Combining these two functionalities lead to a controlled transient self-organization of colloidal structures far from equilibrium, further broadening the spectrum of applications for colloidal self-organization.

Acknowledgments

Auch wenn am Ende nur mein Name auf dem Einband dieser Arbeit zu finden sein wird, ist sie doch nur durch die Zusammenarbeit und Unterstützung vieler anderer Menschen ermöglicht worden. An oberster Stelle möchte ich mich bei meinem Betreuer Prof. Dr. Andreas Bausch bedanken, dem ich eine steile Lernkurve in vielen Bereichen der Wissenschaft zu verdanken habe. Weiterhin möchte ich Matthaeus Schwarz-Schilling und Jonathan List (beide Lehrstuhl Simmel) danken, die mich mit den experimentellen Grundlagen bzgl. Enzymkinetik und Gold-Nanopartikeln vertraut gemacht haben. In diesem Zuge möchte ich mich ebenfalls bei Timo Krüger (Lehrstuhl Frey) bedanken, der die hier gezeigte Strukturbildung mithilfe von Simulationen untersucht und so für interessante Diskussion gesorgt hat. Prof. Dr. Alessio Zaccone danke ich für die fruchtbaren Diskussionen über die analytische Modellierung in dieser Arbeit.

Ich danke allen Mitarbeitern der Gruppen E27 und E22, die die Arbeit im Labor auch an frustrationsreichen Tagen und Wochen zu einer schönen Zeit gemacht haben. An dieser Stelle möchte ich insbesondere meinen Bürokollegen Benedikt Buchmann und Henry Dehne, sowie Joanna Deek nicht nur für die wissenschaftliche Zusammenarbeit sondern vor allem für die überragende Atmosphäre im Büro danken. Dank euch und anderer Leidensgenossen – Katharina Henneberg, Leone Rossetti, Felix Keber, Ryo Suzuki, Matthias Schuppler – wird diese Zeit am Lehrstuhl für mich unvergesslich bleiben.

Aus meinem Freundeskreis möchte ich meinen Dank insbesondere an Jochen Müller richten, der nach Studium und Masterarbeit auch während der Promotionsphase ein ständiger Begleiter war. Der gegenseitige Austausch von Wissen und Erfahrungen war gerade in schwierigen Situationen von unschätzbarem Wert.

Neben meinen Eltern Roman und Eveline, ohne deren Unterstüztzung ich nicht da stehen würde, wo ich heute bin, möchte ich vor allem meiner Frau Paula danken. Unsere gemeinsame Familie bildet das Fundament meines Lebens und ist ohne sie nicht denkbar.

Contents

1. Preface: Structure Formation far from Equilibrium **1**

2. Theoretical and Experimental Framework **3**
2.1. Colloidal structure formation far from equilibrium 3
2.1.1. Colloids and fractality 3
2.1.1.1. Fractals and structure formation far from equilibrium . . 3
2.1.1.2. Limits for the fractal dimension of colloidal coagulates . . 5
2.1.2. Fast coagulation theory 8
2.2. Colloidal structure formation *via* DNA hybridization 9
2.3. Dynamic structure formation *via* synthetic biochemical reactions 12
2.3.1. Synthetic biochemical reaction networks 12
2.3.2. Transient structure formation 14
2.3.3. Enzyme kinetics of T7 RNA polymerase and RNAseH 15
2.4. Motivation: Nucleic acids to stir colloidal structure formation 16

3. Materials and Methods **21**
3.1. Static structure formation 21
3.1.1. Polystyrene colloids 21
3.1.1.1. DNA sequences and coating 21
3.1.1.2. Sample preparation 23
3.1.1.3. Purfication of colloidal structures 24
3.1.1.4. Confocal microscopy 24
3.1.1.5. Image analysis and structure quantification 24
3.1.2. Nano gold colloids 27
3.1.2.1. DNA sequences and coating 27
3.1.2.2. Sample preparation 28
3.1.2.3. UV/VIS spectroscopy 29
3.1.2.4. Electron microscopy 29
3.1.2.5. Dark field microscopy 29
3.1.3. Macroscopic hybrid polymer-colloid DNA gels 29
3.1.3.1. Rheology 29

3.1.3.2. Printable gels . . . 30
3.1.4. Light scattering . . . 31
3.2. Dynamic structure formation . . . 32
3.2.1. DNA sequences and coating . . . 32
3.2.2. Sample preparation . . . 32
3.2.3. Fluorescence measurements . . . 32
3.2.4. Bright field light microscopy . . . 33
3.2.5. Gel electrophoresis . . . 33

4. Static Structure Formation by DNA coated colloids 35
4.1. Binary heterocoagulation . . . 35
4.1.1. Fractal growth . . . 35
4.1.2. Controlling cluster size and geometry . . . 37
4.1.3. Time-evolution in binary systems . . . 39
4.1.4. Analytical model . . . 42
4.2. Ternary heterocoagulation . . . 45
4.2.1. Equally sized colloids . . . 45
4.2.2. Differently sized colloids for asymmetry . . . 46
4.3. Hierarchical self-organization of complex structures . . . 48
4.4. Applications . . . 50
4.4.1. Light scattering by mesoscopic colloidal structures . . . 50
4.4.2. Macroscopic hybrid polymer-DNA coated colloid gels . . . 51
4.4.3. Scaling down to gold nanoparticles for optical applications . . . 54
4.5. Discussion and Outlook . . . 56

5. Dynamic Structure Formation by DNA Coated Colloids 59
5.1. RNA polymerization and degradation for colloidal aggregation . . . 59
5.1.1. Controlling RNA polymerization by T7 polymerase . . . 59
5.1.1.1. Controlling the rate of RNA polymerization . . . 59
5.1.1.2. Quantity and specificity of RNA polymerization . . . 61
5.1.2. RNA degradation by RNASeH . . . 63
5.1.3. Competition of polymerization and degradation yields a tunable RNA Pulse . . . 65
5.2. Coupling the RNA signal to structure formation . . . 67
5.2.1. Colloidal structure formation by RNA polymerization . . . 67
5.2.2. Colloidal structure disintegration by RNA degradation . . . 70
5.3. Transient colloidal structure formation . . . 72
5.4. Discussion and Outlook . . . 74

A. Appendix **i**

A.1. Polymerization of RNA by T7 RNA polymerase i

A.2. Clustering algorithm i

A.3. List of publications xv

List of Figures

Bibliography

1. Preface: Structure Formation far from Equilibrium

Clouds are not spheres, mountains are not cones, coastlines are not circles, and bark is not smooth, nor does lightning travel in a straight line.
- Benoit Mandelbrot, "The fractal geometry of nature" (1982)

Structures can be organized in an active or passive fashion. While an active organization requires active transport of the building blocks to reach precise spatial and temporal control of the evolving structure, passive organization takes advantage of a phenomenon that is especially prominent on the nanoscale: self-organization.
Self-organization is a process by which a complex macromolecule or a supra-molecular system spontaneously assembles itself from its components. In order to move the components of such a system to the desired location, self-organization crucially relies on two things: random motion to drive structure formation and defined inter-component interactions to control structure formation. These interactions allow the components to reach their final location and configuration. In equilibrium self-organization it is assumed, that in order to create structures by rational design, all possible configurations have to be sampled in time so that the energetically most favorable configuration can be found and a thermodynamical equilibrium state is reached. This primary concept of self-organization is also the basis of many natural occurring structures on the nano- and microscale, from DNA to proteins, the construction plan and the building blocks of all living matter. However, although reaching a state of thermodynamic equilibrium is a promising and well-understood approach to artificially program structure formation processes on the nanoscale, it is not strictly required for self-organization. Self-organization can also be dominated by kinetic traps, leading to structure formation far from equilibrium, a mechanism that is ubiquitous in nature on larger scales.
In 1967, Benoit Mandelbrot first described a class of symmetry in a myriad of mesoscopic and macroscopic structures, namely self-similarity. Self-similar objects show an invariance to scaling, meaning an invariance with multiplicative changes of scale. They can be described by a power-law with a fractal exponent, referred to as the Hausdorff or fractal dimension.

As they are scale-free, those structures offer a pathway to bridge length scales from the micro- to the meso- and macroscale. Consequently, they have been found on many scales in nature, ranging from neurofilament networks and cytoskeletal networks in eukaryotic cells, to tissue formation, to the growth of tree branches, coast lines and even mountains. As these structures are predominantly formed far from equilibrium, it is presumed that there exists a strong connection between fractals and non-equilibrium processes.
In colloidal sciences it was found, that also the irreversible aggregation of colloidal particles results in self-similar structures that can be classified as fractals. At low densities, they form clusters and gels with a well-defined fractal dimension. As colloidal suspensions can be found everywhere in nature and industry ranging from paints, inks and foams to ceramics, clay and food, the fundamental mechanisms leading to colloidal structure formation have been studied intensively. Remarkably, the value of the fractal dimension found in colloidal sciences is comparable to those found in biological samples, indicating that also mesoscopic biological systems exhibit similar fundamental mechanisms of non-equilibrium structure formation.
However, there are significant differences between classically studied colloidal systems and biological non-equilibrium system. Firstly, in colloidal sciences mainly homoaggregation has been studied, where only one aggregation species is available, highly limiting the complexity of the resulting structures. In contrast to that, in biological systems multiple different objects are simultaneously interacting in time and space to build complex structures. Secondly, self-organization in colloidal sciences is a rather static process, where structure formation is triggered by a single event and terminated by the depletion of material. In contrast to that, biological structure formation processes such as cytoskeletal structure formation are driven by continuous energy transformations that are substantially supported by enzymatic activity. This enables the cell to manipulate also non-equilibrium structure formation in time in order to maximize functionality for changing environmental challenges.
It is the aim of this thesis to expand the known mesoscopic colloidal structure formation far from equilibrium to a higher level of complexity. In order to do so, in the first part, colloidal structure formation will controlled by using DNA hybridization to provide for specific interactions between micrometer sized colloidal particles. This allows for studying the non-equilibrium structure formation of a multi-component colloidal system up to five different differently sized and coated particles, leading to a well-controlled static structure formation far from equilibrium.
In the second part of this thesis, enzymes will be deployed to produce or degrade RNA signals that drive the found structure formation processes dynamically. This leads not only to a timely control of the processes but also to a transient self-organization of colloidal structures far from equilibrium, demonstrating the dynamic functionality of the investigated system.

2. Theoretical and Experimental Framework

2.1. Colloidal structure formation far from equilibrium

2.1.1. Colloids and fractality

2.1.1.1. Fractals and structure formation far from equilibrium

Fractal structures are part of a symmetry class that is commonly referred to as self-similarity. Self-similar structures are invariant to changes in size, thus called scale-free [1]. As a result of their scale-free nature, Euclidean measures such as volume, area and perimeter often diverge when applied. This can easily be seen by looking at a classical fractal structure such as the Koch curve, that has been proposed in 1904 by the Swedish mathematician Helge von Koch [1]. To create a self-similar structure an initiator and a generator is used (see figure 2.1A). The Koch generator fractures a straight line (initiator) of length 1 in a triangular shape of length $\frac{4}{3}$. Applying the generator to the initiator n-times will also fracture the initiator in a length of $\frac{4}{3}^n$, thus yielding an infinitely long undifferentiatable Koch curve or Koch snowflake (see figure 2.1B) for $n \to \infty$. Thus a central question emerges: If a curve has no defined length or curvature, how can it be characterized?
It was found by Felix Hausdorff [2] that while the length L of a Koch curve $L = N \cdot r$ diverges, there is a critical exponent D_H for which the product $N \cdot r^{D_\mathrm{H}}$ stays finite. This critical exponent is called the Hausdorff dimension and can be calculated for a Koch curve as

$$D_\mathrm{H} = \lim_{r \to 0} \frac{\log N}{\log 1/r} = \frac{\log 4}{\log 3} = 1.26\ldots \quad . \tag{2.1}$$

This simple construct shows that besides the limits of Euclidean geometry ($D_{\mathrm{H,\ line}} = 1$, $D_{\mathrm{H,\ area}} = 2$, $D_{\mathrm{H,\ volume}} = 3$) there exist critical exponents that are fractions of natural numbers, thus called fractals.
Over 60 years later Benoit Mandelbrodt first applied this idea of self-similarity to coastlines of different countries and therefore naturally occurring objects [3]. He showed, that also coastlines are scale-free and that their measured length therefore depends on the length

of the ruler used in the measurement. He extracted the fractal dimension of the coastlines from the data, showing that the Hausdorff dimension universally characterizes the data (see. Figure 2.1C, D). Consequently, Mandelbrodt's discovery lead to a quick spreading of fractal

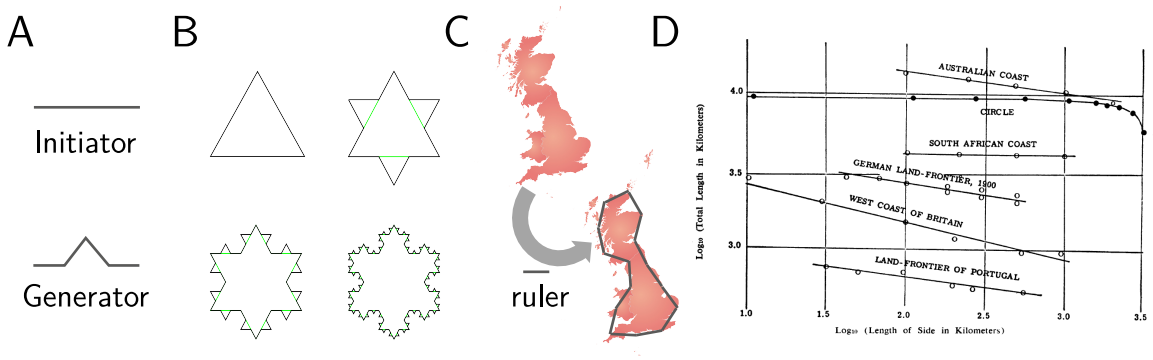

Figure 2.1.: Fractals in theory and experiment. (A) Initiator and generator of a Koch curve. (B) Different numbers of n iterations of the generator applied to an initial construct, resulting in a Koch snowflake, a fractal indifferentiatable structure with an infinite perimeter for $n \to \infty$. (C) Concept of the first application of fractality to experimental data, the coastline of Britain. The length of the ruler used to measure the length of the coastline yields different results. (D) Results of the measurement in (C) by B. Mandelbrodt [3]. Shorter ruler lengths result in longer coastline lengths, showing that the coastline length is ill-defined. In contrast to that, a clear power-law dependency of coastline length to ruler length is found that relates to the Hausdorff or fractal dimension, thus enabling to universally characterize different coastlines and land frontiers.

analysis, where structures are characterized by their Hausdorff dimension [4][5][6][7][8]. To characterize scale-free structures quantitatively and robustly, different mathematical measures have been developed [1]. However, the widely used term fractal dimension D_f, is an umbrella term for all these measures, that is in an exact sense only identical with the Hausdorff dimension in certain mathematical limits. For details of the calculation of D_f in this thesis, see section 3.1.1.5.

Fractals in colloidal sciences first appeared, when the aggregates of colloidal nanoparticles where studied with electron microscopy techniques. Forrest and Witten showed that smoke aggregates exhibit long-range correlations and power-law scaling [9]. To explain these experimental findings, they subsequently developed a simple diffusion based model that was sufficient to qualitatively describe the morphology of the observed aggregates. This model was consequently termed DLA (Diffusion-Limited Aggregation). It resembles the following process. A single spherical particle is placed in the center of an on-lattice simulation. Subsequently, a second spherical particle is released at an infinite distance and diffuses randomly until it meets the first particle, modeling an irreversible binding of the particles at first contact. Another particle is released at an approximately infinite distance from the emerging structure and the process is repeated for a certain amount of times. This sim-

plified model leads to the formation of dendritic fractal structures, yielding a Hausdorff or fractal dimension of $D_{\text{f, DLA 2D}} = 1.7$ and $D_{\text{f, DLA 3D}} = 2.5$ in 2 and in 3 dimensions [10], respectively. It is important to note, that D_f in general is different for 2D and 3D processes. However, if $D_f \leq 2$, fractal dimensions extracted from 2D projections of 3D images should stay unchanged [11][12].
Despite the obvious oversimplification of the underlying physical processes and the lack of an analytic fundament, the DLA model shows, that colloidal structure formation far from equilibrium directly yields fractal structures. It therefore not only indicates the deep connection between out-of-equilibrium structure formation and fractality, but also hints to the fact that the fractal dimension D_f is an adequate measure for the morphology of these structures.

2.1.1.2. Limits for the fractal dimension of colloidal coagulates

Soon it was found using gold nanoparticles precipitated with salt that the fractal dimension of colloidal coagulates is about $D_f \approx 1.75$ [11]. This significantly lower fractal dimension than the DLA limit just reflects the oversimplification of the aggregation process by the DLA model. While the DLA model only describes the diffusion of single particles, real colloidal systems also exhibit cluster-cluster interactions. Taking these cluster-cluster interaction into account, further simulation studies could show that the limit of $D_{f,DLCA} = 1.78 \pm 0.1$ [13] is indeed universal for many materials [11][14][15][16][17][18], experimentally verified by light scattering techniques and was consequently termed DLCA (Diffusion-Limited Cluster Aggregation). This model is based on simulations and has been investigated for different simulation conditions [19][20][21].
Besides the DLCA limit, which represents the irreversible binding of sticky particles at first contact, there also exists a second universal limit for aggregation processes that are not limited by diffusion, but by reaction times, thus referred to as Reaction-limited Cluster Aggregation (RLCA). The difference between both limits can be described as follows. In a solution of stabilized colloids a certain repulsion barrier E_B prevents the particles from precipitating (see figure 2.2). According to DLVO theory [22][23], this repulsion barrier can be modeled by the superposition of an attractive van-der-Waals potential and a repulsive electrostatic potential originating from the overlapping of the electric double layers that surround the charged particles. If this energy barrier is reduced to much less than $k_B T$, particles coagulate on first contact, reflecting the DLCA limit (see figure 2.2A). The resulting structure is highly branched and uncondensed (see figure 2.2C). If E_B is comparable or larger than $k_B T$, the probability to overcome this energy barrier can be written as $P \propto \exp\left(-\frac{E_b}{k_B T}\right)$. At high E_B this leads to the RLCA, limit where $P \ll 1$ (see Figure 2.2B). In this limit, a significantly higher fractal dimension is observed, $D_{f,RLCA} = 2.1 \pm 0.5$ [24][25], reflecting more

compact structure formation (see figure 2.2D). In both cases, DLCA and RLCA, the binding is irreversible and does not allow for rearrangements. However, in contrast to DLCA, the binding probability of a particle in RLCA increases significantly when encountering multiple binding partners at the same time. This leads to denser packed coagulates and therefore to a larger fractal dimension.

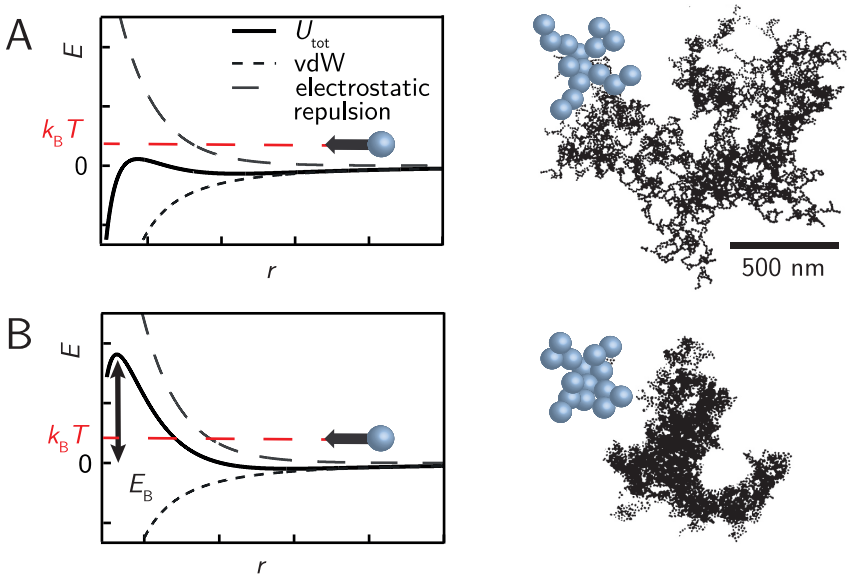

Figure 2.2.: Comparison of the two established colloidal structure formation regimes far from equilibrium: diffusion-limited cluster aggregation (DLCA) and reaction-limited cluster aggregation (RLCA). (*A*) Qualitative inter-particel potential assumed in a DLCA process. According to DLVO theory, charged particles in a solution are stabilized by the electrostatic repulsion generated by the overlapping of the electric double layers of the particles. If the repulsion is weak compared to the van-der-Waals attraction, the thermal energy of the particles suffice to reach van-der-Waals binding on first contact, resulting in a branched, uncondensed structure. (*B*) Qualitative inter-particel potential assumed in a RLCA process. If the electrostatic repulsion is sufficiently large, the particles have to overcome an energy barrier E_B in order to bind. This reduces the binding probability significantly, leading to a preferred binding of multiple particles and therefore condensed structure formation. Electron microscopy micrographs taken from [26].

Besides these two established limits DLCA and RLCA, also other values for the fractal dimension for colloidal aggregation are reported in literature. First of all it is important to note, that in experiments as well as in simulations fractal growth is always confined by the chamber size. At low volume fractions Φ, the aggregation takes place in the so-called flocculation regime [27]. In this regime, the coagulates can diffuse freely and follow the discussed DLCA or RLCA process. However, when the cluster sizes become comparable to the dimensions of the sample chamber, the aggregation behavior changes. When these critical cluster sizes are reached, the clusters lose their ability to rotate and diffuse freely and interpenetrate each other, thus being arrested in their position and orientation. This re-

sembles a process known from percolation theory [28] and is thus called percolation regime. Similar to percolation theory, a fractal dimension of $D_{f,\text{perc.}} = 2.5$ was found in the percolation regime [29][30]. Consequently, the transition from the flocculation to the percolation regime depends on the volume fraction Φ. For large Φ, the onset of percolation will be at smaller cluster sizes, while at small Φ percolation will be only detectable at large cluster sizes. Thus, it was shown by simulations, that DLCA and RLCA processes only lead to the discussed fractal dimension in dilute suspensions up to a volume fraction of $\Phi_{\text{limit}} \approx 2\ \%$ [30]. Determining the fractal dimension above Φ_{limit} leads to a strong dependency of D_f on Φ due to a dominance of the percolation regime, thus yielding higher fractal dimensions [31][32]. Other authors motivate the transition from RLCA or DLCA to $D_f = 2.5$ without percolation theory [13]. They refer to these aggregates as "superaggregates", that are composed of a short range fractal dimension in the RLCA or DLCA limit and a long range fractal dimension of $D_{f,\text{perc.}} = 2.6$. However, both approaches confirmed by simulations or experiments that the canonical DLCA and RLCA are only valid on certain length scales depending on the concentration of the particles.

Additionally, there exists a third limit in literature. This limit describes irreversible aggregation that is not caused by freely diffusing particles, but rather particles that show ballistic motion. This limit is therefore referred to as ballistic limited cluster aggregation (BLCA) with $D_{f,BLCA} = 1.9$ [25].

Using oppositely charged colloids, also lower fractal dimensions than the DLCA limit have been found and investigated experimentally and theoretically. It was shown that the fractal dimension can be tuned from 1.3 to 1.7, depending on the electrolyte concentration of the buffers [33]. However, Brownian dynamics simulation that where part of this study could not reproduce fractal dimensions lower than 1.6. A different study confirmed by static light scattering, optical microscopy and Brownian dynamics simulations, that using oppositely charged colloids, a fractal dimension of 1.21 ± 0.15 can be reached in a buffer containing no electrolytes [34]. This lowest known fractal dimension that is reasonably close to the linear limit $D_f = 1$ is a consequence of the electrostatic repulsion caused by the charged colloids that have been used in these studies. If the long range electrostatic forces are screened by using a sufficiently high concentrated electrolyte, the canonical limit of DLCA is reached [33]. Consequently, lowering the electrolyte concentration leads to a strengthening of the long range electrostatic forces, giving rise to significant dipole and quadrupole moments of the emerging clusters. This directly leads to a biased cluster growth at the exposed cluster ends that exhibit the lowest electrostatic potential.

System	Fractal Dimension D_f	Reference
charged colloids	1.21–1.7	[35]
DLCA	1.78 ± 0.1	[13]
BLCA	1.9	[25]
RLCA	2.1 ± 0.5	[24]
Percolation/Superaggregates	2.5–2.6	[36][37]

Table 2.1.: Established limits for the fractal dimension D_f of colloidal coagulates.

2.1.2. Fast coagulation theory

Fast coagulation theory (FCT) has been developed by Smoluchowski in 1916 [38] to describe the aggregation behavior of monodisperse spherical particles of a single type into larger coagulates, termed homocoagulation. It is purely diffusion based and does not take into account any physical potentials or chemical reactions. It is therefore considered a kinetic theory that does only apply to non-equilibrium structure formation processes. Thus, it is suitable to describe simple aggregation systems, where particles of one species bind on first contact, such as it is found in DLCA.
In summary, Smoluchwoski tackled the following question: How big is the probability that a diffusing particle adsorbes to a central particle until a certain time t in a dilute homocoagulation system?
To calculate this, he derived the influx of particles to a central particle by using Fick's first law under spherical conditions, gaining the influx of a single particle over time. This in turn yields the binding probability with time, which can also be expressed as the so-called fast coagulation rate

$$W_k = 8\pi DRc \quad , \tag{2.2}$$

where D is the diffusion coefficient, R the radius of the central particle and c the concentration of particles. Note that this equation is only valid for dilute monodisperse systems. As the inverse of fast coagulation rate gives the average time before two particles first meet, it can subsequently be used to calculated coagulation processes of single particles over time. As a result, fast coagulation theory yields differential equations that describe the development of the cluster size distributions $n_i(t)$ in time

$$V\frac{\mathrm{d}n_i}{\mathrm{d}t} = \frac{1}{2}\sum_{j=1}^{i-1} = k_{j,i-j}n_j n_{i-j} - n_i \sum_{j=1}^{\infty} \quad ,k_{ij}n_j \quad , \tag{2.3}$$

where V is the total volume of the system, n_i is the number of coagulates containing i particles and k_{ij} are the rate constants that are considered to be the kernel of the system.

It is important to note that FCT does not bear any information of the geometry of the structure that is built.

In contrast to homocoagulation, the term heterocoagulation is commonly used to describe processes that lead to an irreversible binding in mixed particulate systems of different sizes, shapes and functionalities [35]. However, also the terms heteroaggregation, heteroassociation and heteroflocculation are found in literature to describe similar phenomena [39]. Although FCT is made for describing homoaggregation systems, it can in principle be expanded to binary heterocoagulation that takes into account two different species of particles that can only bind each other but not themselves. In order to describe a binary process equation 2.3 becomes

$$V\frac{\mathrm{d}n_i^l}{\mathrm{d}t} = \frac{1}{2}\sum_{j=1}^{i-j}\sum_{m=0}^{j} k_{j,i-j}^{m,l-m} n_j^m n_{i-j}^{l-m} - n_i^l \sum_{j=1}^{\infty}\sum_{m=0}^{j} k_{ij}^{lm} n_j^m \quad . \tag{2.4}$$

Due to the complexity of equation 2.4, most theoretical work on heterocoagulation procceses has been done by performing simulations [40][41][33]. However, equation 2.4 was used to derive an approximation for the monomer number evolution in the zero time limit, known as the HHF approximation [42]

$$V\frac{\mathrm{d}n_1}{\mathrm{d}t} = -k_s(n_1)^2 \quad , \tag{2.5}$$

where k_s is an effective dimer formation rate constant

$$k_s = 2x(1-x)k_{11}^{10} \tag{2.6}$$

and k_{11}^{10} is often referred to as the absolute heteroaggregation constant k_{AB} [43][44]. This indicates that FCT can in principle be applied to heteroaggragtion processes. Hence, it is used in this thesis to model fundamental processes involved in binary heterocoagulation of DNAcc and to predict and explain experimental phenomena. This is of high importance, as it lays the fundamental groundwork for future applications of the multi component colloidal aggregation processes shown herein.

2.2. Colloidal structure formation via DNA hybridization

In general, DNA coated colloids (DNAcc) are particles of any size, shape or material that are coated with single-stranded or double-stranded DNA in order to provide and control binding affinities between the particles and another DNA coated substrate [47]. The basic

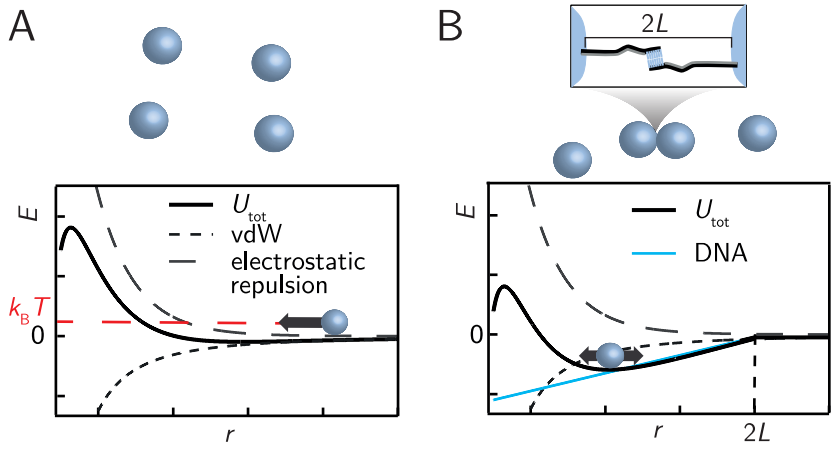

Figure 2.3.: Principle of structure formation by DNA coated colloids. (*A*) In a stabilized solution of particles, the electrostatic repulsion of the overlapping electric double layers of the particles keeps the particles in a monodisperse state. (*B*) Coating the particles with complementary DNA creates another potential by Watson-Crick base pairing [45]. It can be approximated by a linearly increasing function [46], thus generating a local minimum in $U_{\mathbf{tot}}$ and allowing the particles to bind specifically.

idea is to facilitate the well-understood Watson-Crick base pairing [45] of single-stranded DNA (ssDNA) in order to stir colloidal structure formation processes by tailoring the inter-particle potentials (see figure 2.3). Watson-Crick base pairing is not only highly specific and reversible, but can also be arbitrarily designed, as sequences of lengths up to $\approx$ 200 nucleotides can be synthesized and purchased.

Since they first appeared in 1996 [48][49], DNA coated colloids (DNAcc) have gained much attention throughout the scientific community. They are thought to be the key players in assembling complex meta-materials that are connected to the development of integrated electronics, photonics, optoelectronics and quantum computation [50][51][52]. This high potential for applications is mainly provided by the rapid developments in DNA technology [53]. Consequently, many groups developed ways to coat colloids of different materials and sizes with DNA to investigate their self-assembly behavior (see figure 2.4).

In the original realization, gold nanoparticles (AuNP) with a diameter of 10 nm were coated with single-stranded DNA (ssDNA) by thiol chemistry [49]. As thiol chemistry is a rather universal tool for modifying metal surfaces, this approach can also be applied to other metal nanoparticles [58][59]. On larger scales, preferably polystyrene beads are used. These can directly be coated by amine labeled ssDNA in combination with carboxyl modified polystyrene beads [60]. However, another wide-spread method is to use ssDNA that is end-functionalized with biotin and polystyrene beads that are coated with streptavidin. The biotin-streptavidin bond is the strongest non-covalent bond and therefore guarantees high affinity binding ($K_d \approx 10^{-14}$ M) for most experimental conditions [61]. As nowadays

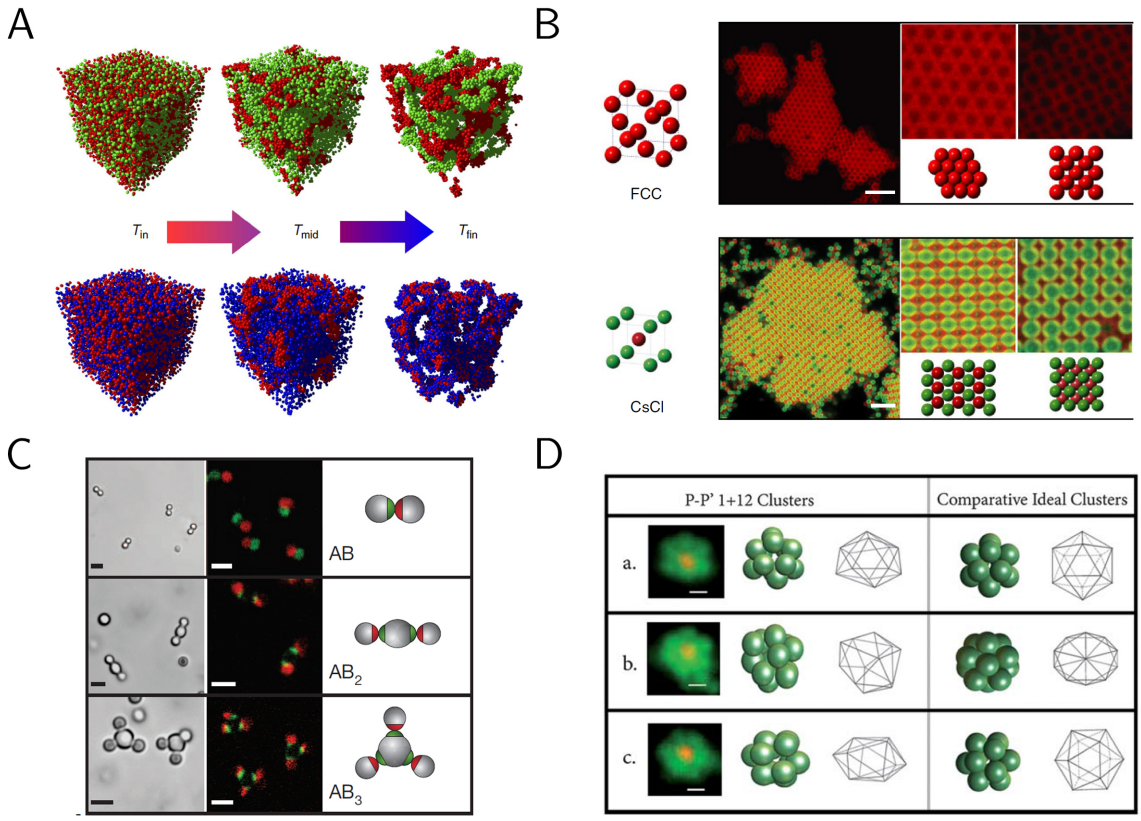

Figure 2.4.: Examples for structures self-assembled with micron sized DNA coated colloids. (*A*) Gelation of a binary system of DNA coated colloids [54]. The time dependent quenching of the DNA interactions leads to different gel structures. (*B*) Equilibrium self-organization of DNA coated colloids into different crystal structures [55]. (*C*) Patchy particles coated with DNA. Creating spherical particles with DNA patches allows for the self-organization of small molecule like structures [56]. (*D*) Self-organization of compact crystal-like clusters [57].

a myriad of polystyrene beads of different sizes and coatings as well as other modifications, such as fluorescent and ferromagnetic properties can be purchased, the usage of polystyrene DNAcc has become a valuable experimental tool for investigations of the self-organization of micron sized particles.

The first self-assembly of micron sized DNAcc was experimentally reported in 2005 [46], showing that ssDNA can also be used to link micron sized particles in a reversible aggregation process. However, it was also shown that the greatly enhanced local concentration of DNA strands at the colloidal interfaces leads to a steep increase in melting temperatures compared to expected bulk experiments [46][62]. This often renders the binding of DNAcc pseudo-irreversible at experimentally reasonable temperatures. Since then, studies have focused on tayloring and measuring the inter-particle potentials by adding surface polymers that act as entropic springs, creating an additional repulsive potential to reduce interparticle binding energies [60][63]. This lead to the formation of small particle crystals [60][64][55]

as it has been reported before only for DNAcc on the nanoscale [65][66]. To create compact structures in the equilibrium regime different strategies have been applied. These strategies either rely on the manipulation of single particles [56] or on the reduction of crystal growth [57] and result in single crystal- or molecule-like clusters of two components.

2.3. Dynamic structure formation via synthetic biochemical reactions

2.3.1. Synthetic biochemical reaction networks

Biochemical reaction networks have a long tradition in shaping our understanding of dynamic non-equilibrium systems. Since the first chemical oscillators have been developed in the 1960s [67], a myriad of new *in vivo* and *in vitro* biochemical reaction networks have been found and designed [68]. These can be categorized as:

- Biological reaction networks within living organisms
- Biological reaction networks reconstituted *in vitro*
- Synthetic reaction networks engineered into living organisms
- Synthetic reaction networks in cell free *in vitro* reactions

While biological networks within living organisms (see figure 2.5A) [69] can only be observed and barely controlled, biological networks reconstituted *in vitro* yield the opportunity to control and also manipulate oscillations of certain biochemical components (see figure 2.5B) [70][71]. This in turn facilitates e.g. the biological studies of the circadian cycle that plays an important role in the daily routine of all mammals.
Moreover it has been shown, that biologically occurring oscillations cannot only be reconstituted *in vitro*, but that also synthetic networks can be introduced into living organisms to create an oscillatory expression of a specific protein (see figure 2.5C) [72][73][74].
Besides these mostly biologically motivated biochemical oscillators also synthetic reaction networks in cell free *in vitro* reactions have been developed. These reaction networks are designed rationally on a single molecule basis *in vitro* and therefore promise an excellent control over all their components (see figure 2.5D). They are usually based on DNA strand displacement reactions [75][76][77], DNA/RNA transcription [78][68][79] or transcription and translation networks [80]. The advanced control of these systems furthermore allows for mathematical modeling of the biochemical processes involved [81][82][83], which makes them especially attractive for computational purposes [79].

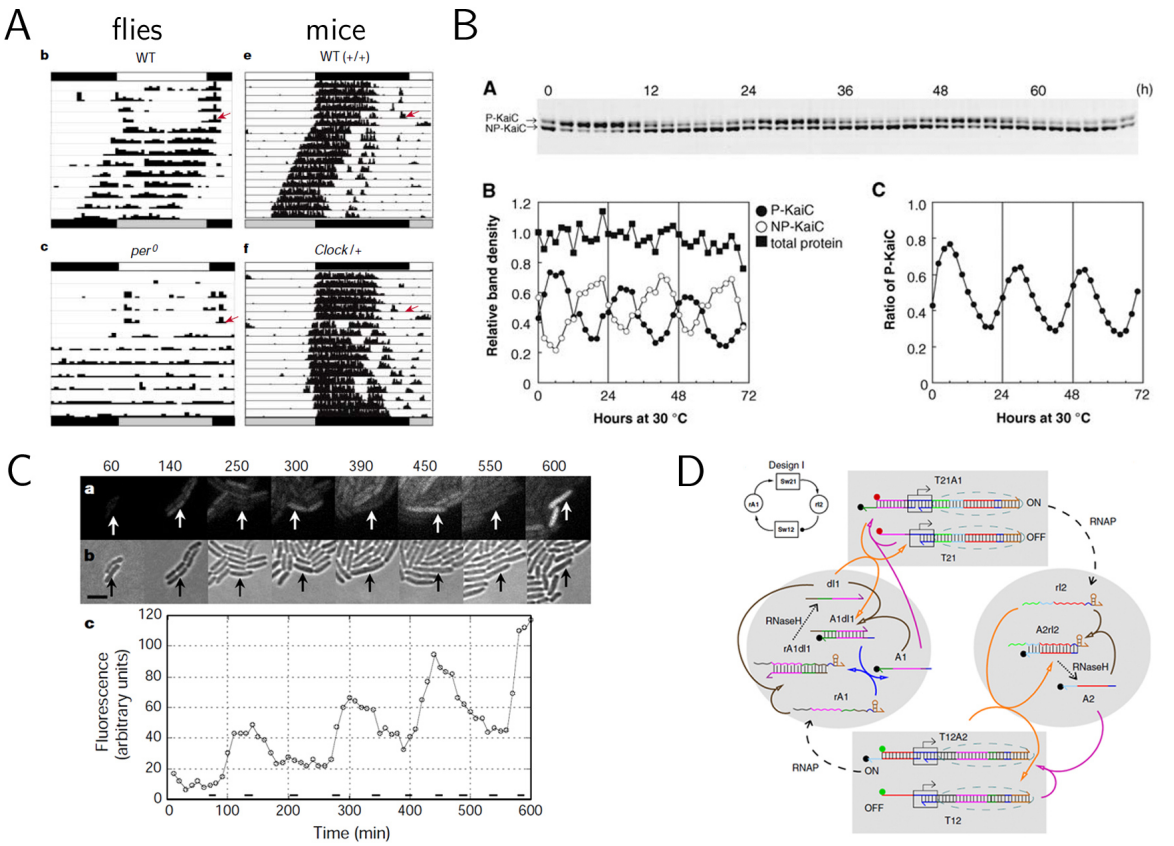

Figure 2.5.: Overview of biochemical reaction networks. (*A*) Biological oscillator within living organisms. Wild-type flyes and mice show a disturbance in their carcadian rhythm upon mutation of the *Clock* gene [69]. (*B*) Biological oscillators reconstituted *in vitro*. Oscillation of KaiC phosphorylation [70]. (*C*) Synthetic biochemical reaction network engineered into a living organism. Timecourse of GFP expression for a single cell of *E.coli* containing repressilator plasmids [72]. (*D*) Synthetic biochemical reaction network in a cell free *in vitro* reaction. Schematic for a transcriptional oscillator that makes use of enzymes to polymerize and degrade RNA signals [68].

Additionally, biochemical reaction networks exhibit fundamental properties for studying not only temporal oscillations, but also spatial trigger waves and oscillations [84]. Spatial oscillations of microbiological components have been demonstrated for reconstituted biological systems [85][86]. These oscillations are known from reaction-diffusion based systems [87][88], that translate mathematically into

$$\frac{\partial C_i}{\partial t} = \nabla \cdot (D_i \nabla C_i) + R_i \quad , \tag{2.7}$$

where C_i is the concentration of species i, D_i is their diffusion coefficient and R_i is the reaction term governed by the biochemical reaction network. Reaction-diffusion systems of this kind are fundamental for our understanding from symmetry breaking in mirco-biological systems [89][90] to the pattern formation in macroscopic organisms [91].

2.3.2. Transient structure formation

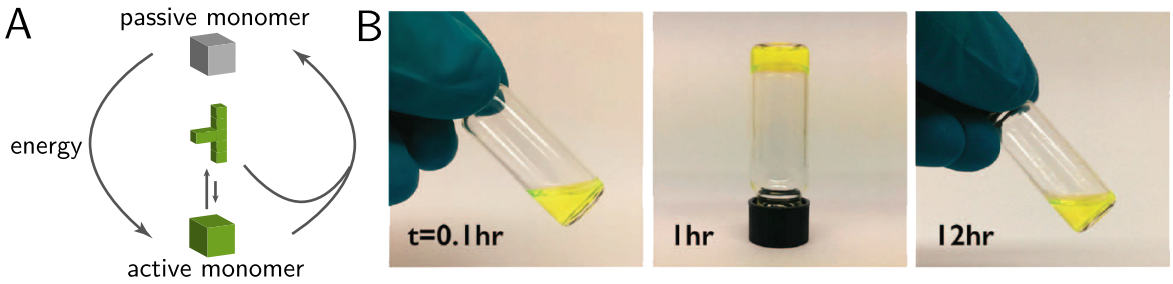

Figure 2.6.: Transient structure formation. (*A*) Principle of transient structure formation. Passive, stabilized monomers are transformed into active monomers that are involved in structure formation. The formed structures are subsequently disintegrated into passive monomers in a relaxation process. (*B*) Example for a transient structure formation process. Chemically fueled structure formation that results in a solid-like gel after 1h and relaxes into a fluid-like state after 12h. [92]

Besides from this intrinsic functionality, synthetic biochemical reaction networks *in vitro* also offer the possibility to trigger and control processes that are not part of the biochemical process itself, but are coupled to it as a load, sometimes referred to as active self-assembling systems. It is thought to be helpful in developing active separation and drug delivery techniques, designing adaptive materials [93][92] or creating autonomously working nanomechanical devices without the necessity of external operations [83]. It has been shown for chemical oscillators, that the conformation of a DNA molecule can be changed in an oscillatory manner [94] as the pH of the buffering medium was changed in time by the chemical oscillator. In a more sophisticated approach, tweezers-like DNA nanodevices [95] were driven by a nucleic acid engine [96][97] in order to open and close the device.
Additionally, there are a few other active self-assembling systems that either use DNA [98] or proteins [99] as building blocks. Using a chemically fueled active self-assembling system, a transient assembly of a synthetic gel could be demonstrated [92]. This synthetic gel autonomously switched from a fluid, to solid-like phase and back, thus capable of bearing mechanical stress in the solid-like phase (see figure 2.6). This transient self-assembling system is thought to constitute a key step in the development of synthetic out-of-equilibrium systems.
Only recently, a nanoparticle system has been introduced that can be switched between an aggregated and a non-aggregated change by a periodic change in pH [100]. This active self-assembling system represents a first step towards a dynamic structure formation of colloids. This indicates that coupling biochemical reaction networks to structure formation processes is a promising approach to create dynamic systems by rational design.
However, it has not been demonstrated how a colloidal system can be driven by a syn-

thetic biochemical reaction network, to create a colloidal system of transient or oscillating self-organization.

2.3.3. Enzyme kinetics of T7 RNA polymerase and RNAseH

T7 RNA polymerase is an enzyme with a molecular weight of 99 kDa [101] found in T7 bacteriophages. It is often used in biotechnological protein expression due to its low basal transcription rate. Like other polymerases, T7 RNA polymerase binds to double stranded DNA templates for transcription of mRNA, requiring $MgCl_2$ for its enzymatic reaction. However, it has a very high affinity for a specific template sequence, the so-called promoter sequence (consensus sequence: `TAATACGACTCACTATAGGG`, $K_D \approx 10$ nM [102]). This specificity allows the T7 bacteriophage to transcribe nearly exclusively the phages genetic code inside the host cell, leading to an effective replication of the phage. This feature is exploited in biotechnology, where the purity of protein expression strongly benefits from this high level of specificity in mRNA transcription and consequently high level of target protein expression. After binding to the promoter sequence, T7 RNA polymerase enters an initiation phase. This initiation phase is dominated by a conformational change at a comparably low rate of 0.01–0.03 $\frac{1}{\mathrm{s}}$ [103]. After initiation and NTP binding, elongation is induced, starting transcription with the bases `GGG` [104] of the promoter sequence and continuing downstream with a rate of 200–260 $\frac{\text{nucleotides}}{\mathrm{s}}$ [101][103]. Due to these properties that allow for enhanced control, T7 RNA polymerase has also been applied within synthetic biochemical reaction networks [68].

Ribonuclease H (RNAse H) is a family of enzymes that specifically degrades RNA strands that are bound in a RNA/DNA duplex, producing 5'-phopsphate and 3'-hydroxil termini [105]. It is thought to remove the RNA primer in DNA replication. Moreover, it has a molecular weight of 17.56 kDa [106] and has been found in many cells and organisms ranging from *Escherichia coli* to yeast to calf thymus [107][108][109]. It has a turn over number of 7.1 $\frac{\text{cleavages}}{\text{monomer}\cdot\mathrm{s}}$ [105], requiring $MgCl_2$ as a co-factor for hydrolysis. In biotechnology it is commonly used in DNA amplification [110] or nucleic acid identification [111] where unwanted residual RNA strands are removed from DNA substrates.

In general, the kinetics of enzymes can be described by the Michaelis-Menten model [112]

$$\frac{dc_P}{dt} = v_{\max}\frac{c_S}{K_M + c_S} = k_{\text{cat}}c_E\frac{c_S}{K_M + c_S} \quad , \tag{2.8}$$

where c_P is the product concentration of the enzymatic reaction, c_S the enzyme substrate concentration, K_M the Michaelis constant, k_{cat} the turnover number, c_E the enzyme concentration and $v_{\max} = k_{\text{cat}}c_E$ the maximum rate. However, this model represents a simplification of the enzymatic reactions. In case of T7 RNA polymerase, the above described complex

template binding and initiation of elongation is not taken into account. Nevertheless, as the binding affinity for the template is very high in comparison to typical NTP binding affinities (K_D = 200 µM [103]), in this thesis it will be assumed that polymerase and template instantaneously form a stable complex that will be treated as an active enzyme.

2.4. Motivation: Nucleic acids to stir colloidal structure formation

Structure formation by DNA coated colloids is a promising approach to create novel structures and materials. It is thought to play a decisive role in the development of integrated electronics, photonics, optoelectronics and quantum computation. Since DNA coated colloids were first reported in 1996, protocols to coat colloids of different materials and sizes from the nanoscale up to the microscale have been developed. Studies have been focusing on equilibrium self-organization of colloidal crystals and small structures made up of two components. In contrast to that, conventional colloidal structure formation that is driven by electrostatic forces is occurring far from equilibrium and is well-established in the regimes of diffusion-limited cluster aggregation (DLCA) and reaction-limited cluster aggregation (RLCA). In these two regimes, especially homocoagulation processes of charged colloids have been studied in experiments and simulations, yielding colloidal gels of a defined fractal dimension D_f. Fast coagulation theory (FCT) has been used to model aggregation processes of also binary systems of oppositely charged colloids. However, it still remains elusive, whether or how the found structure formation processes could be used to produce complex mesoscopic structures by rational design. Furthermore, despite the promising advances concerning synthetic biochemical reaction networks, there have been no studies to combine colloidal structure formation of DNA coated colloids with the appealing molecular dynamics of such biochemically driven systems.

In this thesis, the static and dynamic structure formation of DNA coated colloids are studied. Spherical streptavidin and neutravidin coated polystyrene particles are used to study structure formation far from equilibrium of multiple components (see figure 2.7). In stark contrast to equilibrium self-organization techniques, kinetic traps are not avoided but exploited to control and guide mesoscopic structure formation. To achieve that, the particles are coated with ssDNA that is composed of a 40 nucleotide long spacer sequence and a specific "sticky end" sequence that is designed to interact with other ssDNA during the assembly process in a pseudo-irreversible manner. In static structure formation experiments, the self-assembly of particles of different sizes (1-6 µm) and fluorescent dyes is triggered by adding another ssDNA that links two differently coated particle species, thus called linker strand (see figure 2.7B). This enables a specific control over the aggregation behavior

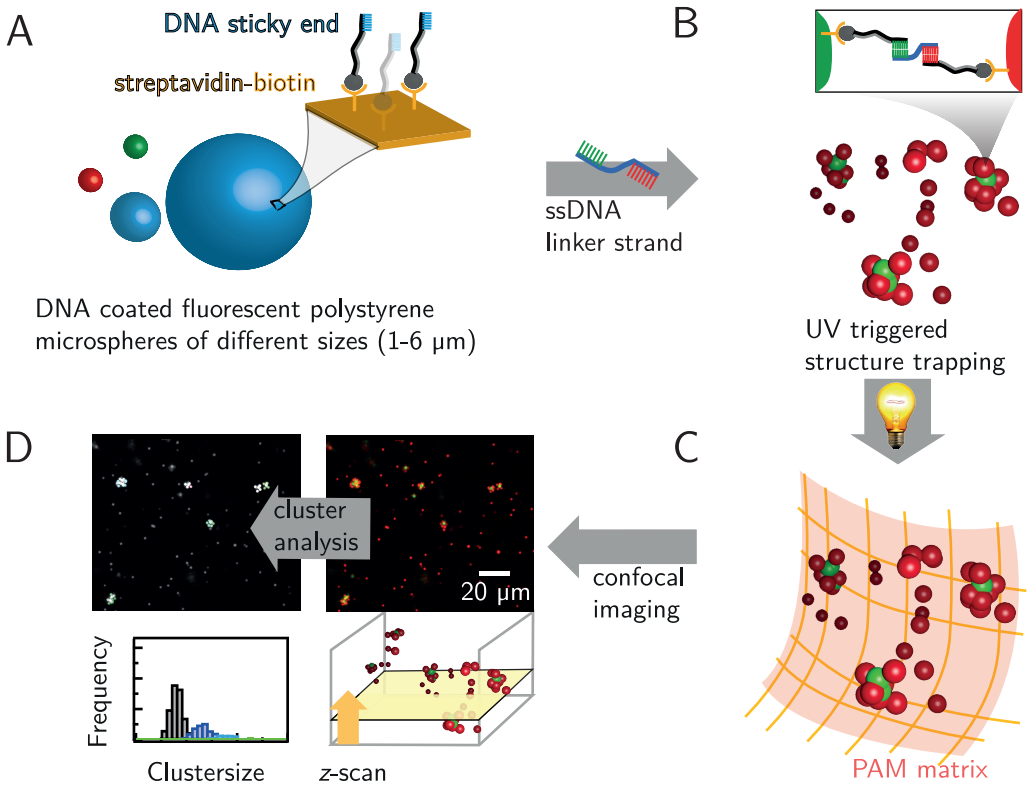

Figure 2.7.: Schematic of the static structure formation processes investigated in this thesis. (*A*) Fluorescent particles between 1-6 µm in diameter are coated with DNA *via* streptavidin-biotin coupling. The DNA is designed to have a "sticky" end that allows the particles to bind their substrates specifically and irreversibly on first contact. (*B*) The structure formation process is triggered by addition of an appropriate linker strand that is complementary to both "sticky" ends of the particle species (here: binary system of green and red particles). (*C*) At an arbitrary point in time the structure formation process can be terminated by light illumination, which triggers the gelation of a polyacrylamide (PAM) matrix, thus inhibiting any further diffusion of the particles. (*D*) The samples are imaged by 3D confocal microscopy and quantitatively analyzed by home-made scripts.

of each component in time. After the structure formation process is finished, the formed structures are fixated by embedding them in a polyacrylamide (PAM) gel. The gelation of PAM can be triggered at an arbitrary point in time by light exposure (see figure 2.7C). This terminates the structure formation process allows for precise 3D confocal imaging and subsequent quantitative image analysis (see figure 2.7D).

The presented rapid structure formation far from equilibrium inherently represents a pseudo-irreversible process. Formed structures are kinetically trapped in energetic minima that are so deep that they cannot be overcome thermally under reasonable experimental conditions. This irreversibility of structure formation by DNA coated colloids is a well-known phenomenon in literature [113]. It is mainly caused by two effects. Firstly, the localization of the DNA strands on the surface of the colloids leads to an extremely increased local DNA

concentration upon contact of two DNA coated colloids. This in turn shifts the on-rate of DNA binding and therefore the equilibrium binding constants of the inter-particle DNA strands to higher association rates. Additionally, the DNA coated colloids are bound in a cooperative manner by the DNA strands. Only if all DNA strands between two particles remain unbound for sufficiently long time that allows the particles to separate *via* diffusion the structure will be disintegrated.

In order to overcome these limitations and to render the structure formation dynamic, a setup is introduced that controls structure formation of DNA coated colloids by enzymatic reactions (see figure 2.8). T7 RNA polymerase is used to produce RNA linker strands

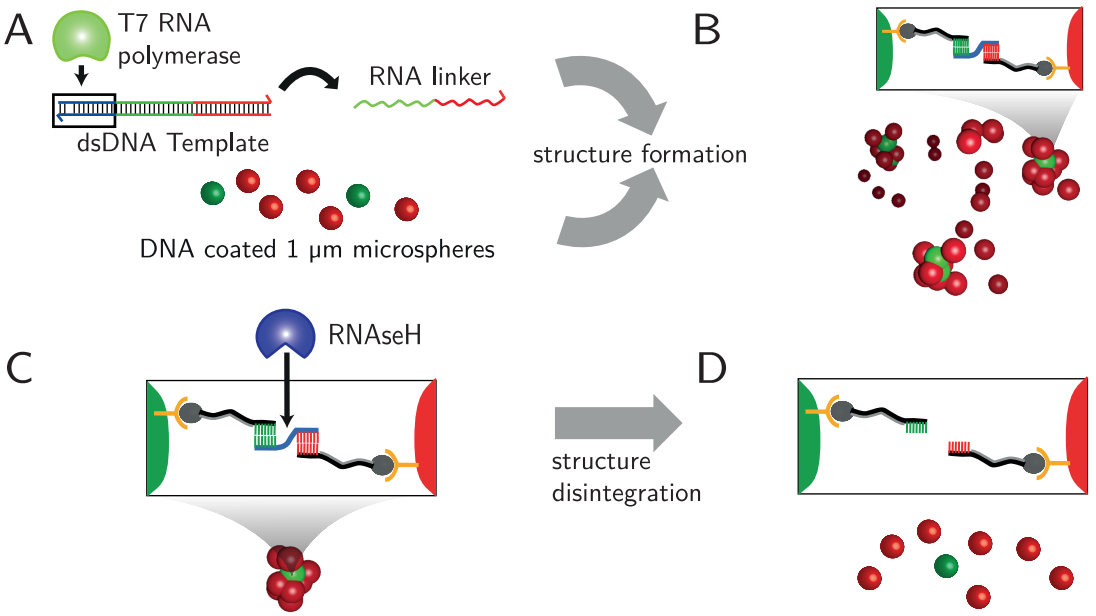

Figure 2.8.: Schematic of the dynamic structure formation processes investigated in this thesis. (*A*) Two types of polystyrene microspheres with 1 µm in diameter are coated with DNA *via* streptavidin-biotin coupling. In contrast to static structure formation samples, the linker strand is autonomously generated inside the sample by T7 RNA polymerase. (*B*) The polymerized RNA linker strand changes the interparticle potential of the microspheres dynamically, thus leading to structure formation. (*C*) This structure formation process can be reverted by introducing the enzyme RNASeH, which degrades RNA strands that are bound in RNA-DNA hybrids. (*D*) After RNA degradation, the structure is disintegrated and set back to the status of (*A*).

that are designed to link two species of DNA coated colloids, resulting in fractal growth. By controlling the enzymatic activity also the colloidal structure formation process can be stirred. To disintegrate the colloidal mesoscopic structures the enzyme RNAseH is deployed. As RNaseH only degrades ssRNA strands that are bound to ssDNA in RNA-DNA duplex, RNAseH is capable of removing the RNA linker strands from the DNA coated colloids, therefore effectively disintegrating the colloidal structures. To show the potential of this ap-

proach, a RNA pulse caused by the two enzymes is coupled to the colloidal system, which results in tunable transient structure formation of the DNA coated colloids. This in total represents an effective coupling of a biochemical reaction network to a system of colloidal structure formation.

3. Materials and Methods

3.1. Static structure formation

3.1.1. Polystyrene colloids

3.1.1.1. DNA sequences and coating

Unless otherwise specified, the chemicals used in this thesis were purchased from Sigma-Aldrich and used without further purification. Streptavidin-coated polystyrene microspheres *A* and α (CP01F, ex/em: 660/690 nm), *B* and β (CP01F, ex/em: 480/520 nm) were purchased from Bangs Laboratories, Γ- and Δ-microspheres (Fluoresbrite YG, ex/em: 441/486 nm) from Polysciences Europe, and Neutravidin-coated polystyrene microspheres γ (FluoSpheres, ex/em: 505/515 nm) from Life Technologies. They were incubated with biotinylated ssDNA docking strands purchased at Integrated DNA Technologies Europe and biomers for at least 12h (DNA sequences see table 3.1). The concentration of docking strands was chosen such that $\approx 6 \cdot 10^4$ docking strands were present in the incubation solution per 1 µm particle. Consequently, 2 µm microspheres were incubated with $\approx 2.4 \cdot 10^5$ strands per microsphere and 6 µm microspheres with $\approx 2.16 \cdot 10^6$ strands per microsphere to preserve docking strand area density on all microspheres. All docking and linker combinations used were checked with NUPACK [114] before experiments to minimize cross-talk. After incubation the particle were centrifuged at 1200 relative centrifugal force, the supernatant was removed, and the sample was resuspended in low-Tris low-salt buffer (150 mM NaCl, 10 mM Tris, pH 8.8). This washing step was performed three times before resuspending the microspheres in a density-matched buffer (450 mM sucrose, 150 mM NaCl, 10 mM Tris, pH 8.8) to prevent the microspheres from fast sedimentation during sample preparation. To gain high monodispersity of the coated mircospheres (polydispersity index ≈ 1.04, see figure 3.1A), the stocks were vortexed and sonicated for 30 s before storage. In between experiments, the microspheres were stored on a rotating device at 4°C. To guarantee sufficient stability for the coated microspheres, they were used for experiments for not longer than a week.

Gels	Sequence
Docking A	5'- CAC CCA CCC ACA CCA CAC AAC $(T)_{40}$ - /3BioTinTEG/ - 3'
Docking B	5'- /5BioTinTEG/ - $(T)_{40}$ CCC CAA ACC CCA AA - 3'
$\overline{AB}_{14}$	5'- GTT GTG TGG TGT GGG TGG GTG TTT GGG GTT TGG GG - 3'
$\overline{AB}_{13}$	5'- GTT GTG TGG TGT GGG TGG GTG TTT GGG GTT TGG G - 3'
$\overline{AB}_{12}$	5'- GTT GTG TGG TGT GGG TGG GTG TTT GGG GTT TGG - 3'
$\overline{AB}_{11}$	5'- GTT GTG TGG TGT GGG TGG GTG TTT GGG GTT TG - 3'
$\overline{AB}_{10}$	5'- GTT GTG TGG TGT GGG TGG GTG TTT GGG GTT T - 3'
$\overline{AB}_{9}$	5'- GTT GTG TGG TGT GGG TGG GTG TTT GGG GTT - 3'
$\overline{AB}_{8}$	5'- GTT GTG TGG TGT GGG TGG GTG TTT GGG GT - 3'
$\overline{AB}_{7}$	5'- GTT GTG TGG TGT GGG TGG GTG TTT GGG G - 3'
$\overline{AB}_{6}$	5'- GTT GTG TGG TGT GGG TGG GTG TTT GGG - 3'
$\overline{AB}_{5}$	5'- GTT GTG TGG TGT GGG TGG GTG TTT GG - 3'
Binary/ternary	**Sequence**
Docking α	5'- CAC CCA CCC ACA CCA ACC AAC $(T)_{40}$ - /3BioTinTEG/ - 3'
Docking β	5'- /5BioTinTEG/ - $(T)_{40}$ A TCT AAT ACA TTA C - 3'
$\overline{\alpha\beta}$	5'- GTT GGT TGG TGT GGG TGG GTG TTT GTA ATG TAT TAG AT - 3'
Docking γ,Γ	5'- /5BioTinTEG/ - $(T)_{40}$ ACTTACTATATAAC - 3'
$\overline{\gamma\beta}$, $\overline{\Gamma\beta}$	5'- GTT GGT TGG TGT GGG TGG GTG TTT GTT ATAT AGT AAG T - 3'
Hierarchical	**Sequence**
Docking α	5'- /5BioTinTEG/ - $(T)_{40}$ ACTTACTATATAAC - 3'
Docking β	5'- CAC CCA CCC ACA CCA ACC AAC $(T)_{40}$ - /3BioTEG/ - 3'
Docking Γ	5'- /5BioTinTEG/ - $(T)_{40}$ ATC TAA TAC ATT AC - 3'
Docking Δ	5'- CTC ATC ATT AAG TCT TAT TTC $(T)_{40}$ - /3BioTEG/ - 3'
Docking ϵ	5'- /5BioTinTEG/ - $(T)_{40}$ CTA TAT CTC TAA TC - 3'
$\overline{\alpha\beta}$	5'- GTT GGT TGG TGT GGG TGG GTG TTT GTT ATA TAG TAA GT - 3'
$\overline{\Gamma\beta}$	5'- GTT GGT TGG TGT GGG TGG GTG TTT GTA ATG TAT TAG AT - 3'
$\overline{\alpha\Delta}$	5'- GAA ATA AGA CTT AAT GAT GAG TTT GTT ATA TAG TAA GT - 3'
$\overline{\Gamma\epsilon}$	5'- GTA ATG TAT TAG ATT TTG ATT AGA GAT ATA G - 3'

Table 3.1.: DNA sequences used in sections 4.1, 4.2 and 4.3.

3.1.1.2. Sample preparation

All samples were prepared in a final buffer of 450 mM sucrose, 150 mM NaCl, 10 mM Tris, and 10 mg/mL BSA. To enable high signal-to-noise ratio (SNR) imaging, 4.5% (w/v) Acrylamide 4K solution (29:1) (Applichem), 0.4% ammonium persulfate, and 140 µM Tris(2,2'-biprydidyl) dichlororuthenium(II) were added to each sample.
Tris(2,2'-biprydidyl) dichlororuthenium(II) is a photoactivatable catalyzator for the polyacrylamide (PAM) polymerization (λ_{max} = 450 nm [115]) and can therefore be used to trigger PAM polymerization at an arbitrary point in time, effectively stopping any diffusion and further aggregation of the particles by white-light illumination for ≈ 3 min with a Schott KL 1600 light-emitting diode lamp. All binary samples were prepared at a fixed majority microsphere volume fraction of 2500 ppm. All ternary and hierarchical aggregation samples were prepared at a fixed minority microsphere concentration of 25 ppm. The specific aggregation in all samples was induced by adding the appropriate linker strands (see table 3.1) at a final concentration of 58 nM, followed by short pipette mixing. After

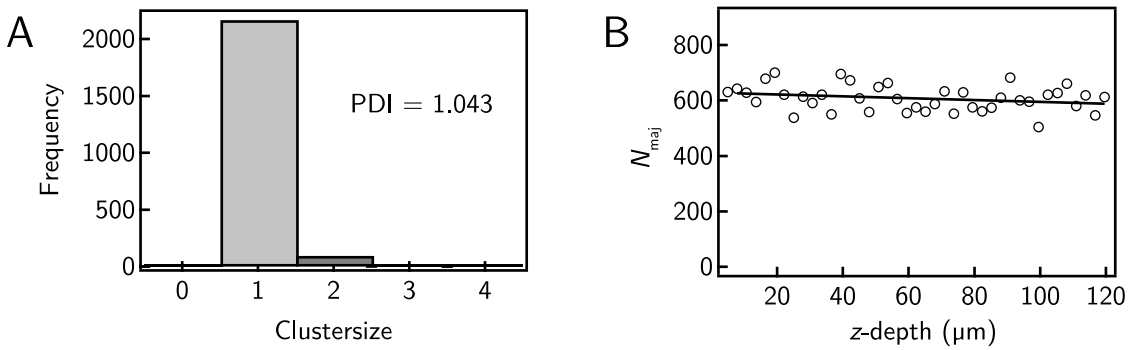

Figure 3.1.: Monodispersity and sedimentation. (*A*) Monodispersity of DNA coated microspheres. After coating, the microspheres were immobilized in PAM and imaged. The clustering algorithm identified 95.72% free spheres, yielding a polydispersity index of 1.043. (*B*) Sedimentation of clusters at $X = 18$ after 6h in the rotating device setup. The majority spheres are nearly equally distributed across the sample, there is only a slight tendency of the spheres towards the top of the chamber (slope: 5% change in density per 100 µm).

linker addition the samples were pipetted into a glass microscopy chamber and mounted on a rotating device at 21°C (≈ 0.3 Hz rotating frequency). The use of a rotating device is necessary to avoid any sedimentation due to imperfect buoyancy matching during the self-organization process (see figure 3.1B). This is especially important where larger structures (> 10 microspheres) are assembled and therefore small buoyancy mismatches already lead to significant sedimentation. All samples were incubated for at least 3 h, unless stated otherwise, followed by PAM immobilization and 3D confocal imaging.

3.1.1.3. Purfication of colloidal structures

Purification of junction-type coagulates was performed by exchanging the central β microsphere with a ProMag HC 1 microsphere (Bangs Laboratories) that was coated in analogy with the above-described protocol with β-docking strands. After 3 h of sample incubation, where the junctions were formed, the Eppendorf tube containing the sample was held close to a neodymium magnet for 30 min. After pellet formation, the supernatant was exchanged three times with final buffer, pipetted into a glass microscopy chamber, and subsequently immobilized by illumination-induced cross-linking of the PAM.

3.1.1.4. Confocal microscopy

Confocal imaging was conducted with a Leica SP5 scanning confocal microscope (Leica Microsystems) at a 3D voxel resolution of $(120 \times 120 \times 460)$ nm^3 with a 63$\times$ water immersion objective (Leica HCPL APO CS2 1.2 63$\times$). The resolution limit of this objective was 163 nm (xy) and 290 nm (z) at a free working distance of 300 µm. This ensured that tens of voxels could be imaged per pixel and that the entire sample chamber could be imaged in z. As the particles and clusters were immobilized for imaging by a PAM gel, imaging was performed at low line rates ($<$ 700 Hz) to maximize the SNR. For every sample 4 z-stacks $(123.02 \times 123.02 \times 80 - 140)$ µm^3, depending on the microsphere density were recorded. The linear compensation mode of the Leica Advanced Fluorscence software package was used to compensate for intensity loss due to light scattering of the particles.
For fluorescence excitation the Argon laser was applied at 488 nm (at 100% intensity) and the Helium-Neon laser was applied at 633 nm (at 100% intensity). The PMT emission sensors were set to the bandwidths 490-560 nm and 659-711 nm, respectively.

3.1.1.5. Image analysis and structure quantification

Historically, the quantification of fractal structures in colloidal physics is dominated by light scattering techniques. Experimental fractal dimensions are extracted from the structure factor $S(q)$ by fitting modeled structure factors to the data [37]. In recent experiments these scattering techniques have also been applied in single cluster measurements, thus termed single-cluster light scattering (SCLS) [35], to monitor the cluster growth of small cluster of up to 8 particles per cluster.
In contrast to that, the fractal analyses presented in this thesis are based on measurements made in three-dimensional real space by confocal microscopy (see section 3.1.1.4 for technical details), an approach that is only applicable due to recent developments in technology [116]. Confocal microscopy is capable of imaging three-dimensional fluorescently labeled samples in time close to the Abbe resolution limit (here:$\approx$ 100 nm). As in this thesis

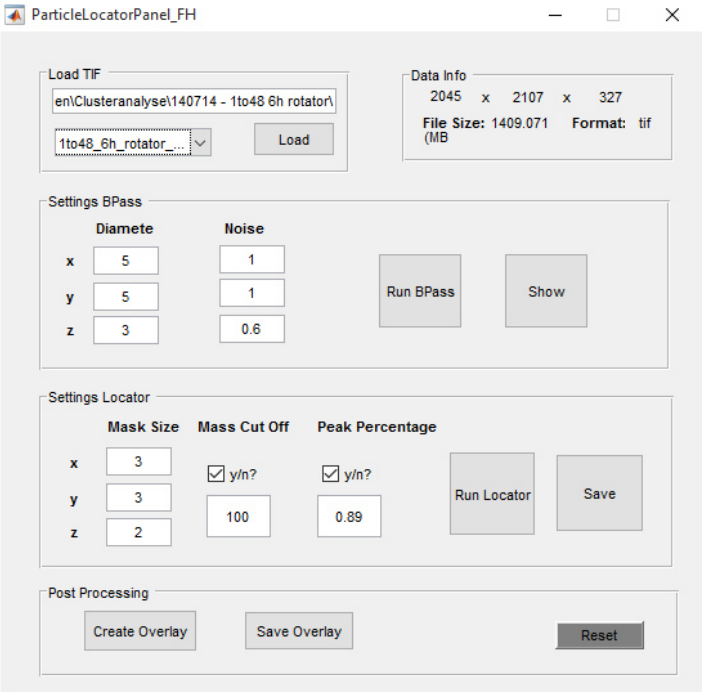

Figure 3.2: Graphical User Interface (GUI) for the Matlab particle counting algorithm. After loading a TIF stack, basic information is displayed on the right. At first, the background substraction and noise reduction parameters have to be defined (Settings BPass). After optimization of the mask size, mass cut off and peak percentage have to be declared, so that the locator can be started. After completion, the results can be saved in a *.txt file. To validate the results, a TIF overlay can be created and saved that shows the determined particle centroid position in 3D.

only polystyrene beads with a diameter of at least 1 µm are used in combination with confocal microscopy, tens of pixels are acquired for each microsphere. This yields raw data that is suitable for particle counting analysis [117] to determine the centroid position of each particle for further quantitative analysis. The Matlab script used in this thesis to extract centroid positions is derived from subpixel resolution algorithm developed by Gao and Kilfoil [118]. It follows the same working principles as the pioneering work of Crocker and Grier [117] that builds the fundament of many particle tracking algorithms. In a two-dimensional image the first step is the reduction of random noise and background subtraction. The background is determined by calculating the boxcar average over a certain region of extent that is larger than a single particle, but smaller than the average distance between particles. After subtraction of the background, random noise is eliminated by convolving the image with a Gaussian surface revolution that is smaller than the noise correlation length. As these values have to be optimized for a specific image, a Graphical User Interface (GUI) was created in this thesis to allow efficient adjustments (see figure 3.2). Next, particles are located by finding local brightness maxima that are subsequently refined by calculating the brightness-weighted centroid of the surrounding region of pixels, called mask. This process is iterated several times to reach maximum accuracy. Finally, the found centroid positions are filtered by their integrated intensity (GUI: mass cut off) and their peak brightness (GUI: peak percentage). To check the results of the script manually, an overlay of the raw data and found centroid positions can be created within the GUI and saved to the hard disc. Data involving 2 µm particles where analyzed by manual particle counting, to exclude multi-counting errors.

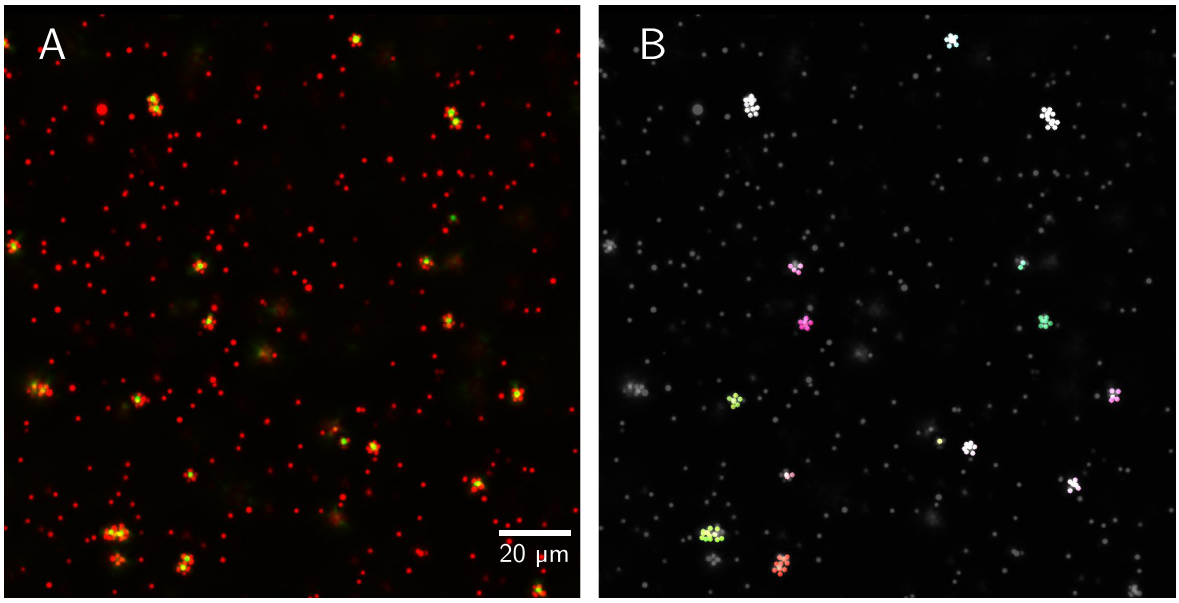

Figure 3.3.: Connectivity-based clustering algorithm. (*A*) Confocal *z*-projection of 10 slices of a $X = 18$ sample. Minority particles (green channel) and majority particles (red channel) form finite coagulates. (*B*) Results of the clustering algorithm. Particles of the identified clusters are coded in different colors, single particles are not detected as clusters.

The resulting centroid positions were loaded to IGOR PRO and analyzed. Cluster analysis in all 1 µm particle aggregation samples was performed with a self-made connectivity-based clustering algorithm (for details see section A.2). The algorithm identified clusters by connecting all particles that had a maximum centroid distance of 2 µm (= 2× particle diameter) (see figure 3.3). The following defining relations for fractal coagulates are applied to the data. Samples that contain diluted fractal coagulates (see figure A,B) are characterized by [13]

$$N = k_0 \left(\frac{R_g}{r_0} \right)^{D_f} \quad , \tag{3.1}$$

where N is the number of particles in an coagulate, k_0 the scaling prefactor, r_0 the particle radius and R_g the radius of gyration of the coagulate, defined as

$$R_g^2 = \frac{1}{N} \sum_{k=1}^{N} (\tilde{r}_k - \tilde{r}_{\text{mean}})^2 \quad . \tag{3.2}$$

If fractal coagulates merge to a fractal gel, Equation 3.1 cannot be applied. In these cases the mass dimension [1]

$$N = k_m \cdot r^{D_f} \tag{3.3}$$

is calculated, where k_m is a scaling prefactor and N is the number of particles that are found inside a radius R within the gel (see figure C,D). As the fractal gel is self-similar,

the mass dimension was calculated for each particle as the center of counting-sphere with radius R and a mean mass dimension was determined subsequently. It has to be noted that both relations can only be applied to data, where the centroid position of every particle can be extracted (see section 3.1.1.5 for particle counting). In contrast to the wide-spread Minkowski-Bouligand or box-counting dimension, where usually intensities are evaluated in image analysis, particle based evaluation methods are independent of thresholding and therefore expected to be statistically more robust.

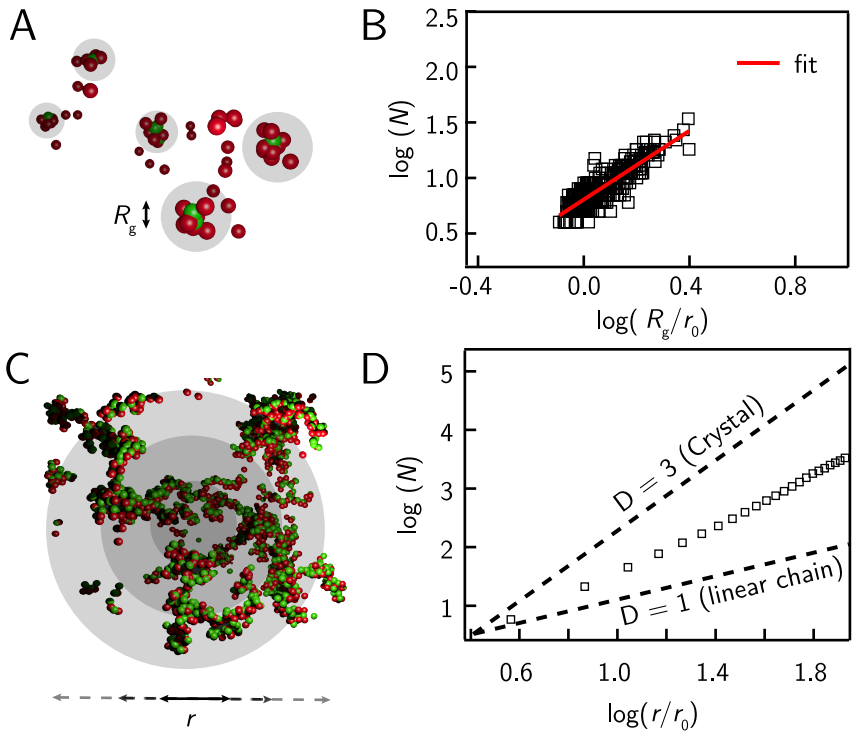

Figure 3.4.: Fractal analysis of gels and clusters. (A) 3D rendering of typical clusters found in binary heterocoagulation. (B) The number of particles N inside a cluster is plotted against the normalized radius of gyration R_g of the cluster and fitted according to equation 3.1. (C) 3D rendering of a fractal gel. (D) The number of particles N inside a sphere of radius r is plotted against the normalized radius of the sphere $\frac{r}{r_0}$. The result lies between the limits $D = 1$ and $D = 3$, reflecting the fractality of the gel.

3.1.2. Nano gold colloids

3.1.2.1. DNA sequences and coating

The gold nanoparticles (AuNPs) had a diameter of 10 nm and were purchased from Cytodoagnostics. To stabilize the bare particles, they were incubated with 0.75 mM Bis(p-sulfonatophenyl)phenylphosphine dihydrate dipotassium (BSPP) for 3 days. After stabilization, the particles were precipitated with NaCl and centrifuged at 1600 relative centrifugal

force for 30 min. The supernatant was subsequently removed and the pellet was resuspended wth 800 µl methanol and 800 µl of 2.5 mM BSPP. After another centrifugation step the pellet was resuspended with 800 µl of 2.5 mM BSPP, yielding a concentrated stock of stabilized AuNP. The AuNP concentration of the concentrated stock was determined by using a Peqlab ND 1000 NanoDrop UV-Vis spectrophotometer to measure the optical extinction at 519 nm (extinction coefficient: $1.01 \cdot 10^8$ $M^1 cm^{-1}$ [119]).
As a first step of AuNP DNA coating, the thiolated DNA docking strands (see table 3.2) were incubated with 10 mM Tris(2-carboxyethyl)phosphin (TCEP) for 30 min. This ensured that the protection groups that were bound to the thiolated ends *via* disulfide bonds were disrupted. Subsequently, the AuNPs were incubated with the de-protected DNA strands at a ratio of 1:100 in 20 mM citrate with pH 7.0. After 3 min of incubation, the pH was increased to pH 9 and buffered by adding 100 mM 4-(2-Hydroxyethyl)piperazine-1- ethanesulfonic acid (HEPES). To test whether the DNA coating was successful, the DNA coated particles were dispersed in 200 mM NaCl. If the dispersion did not change its color, sufficient monodispersity and therefore successful DNA coating was presumed. To remove unbound DNA docking strands, the AuNP dispersion was washed 6 times with 400 µl 0.5×TBE by centrifugation at 10000 relative centrifugal force through a 50 kDa amicon ultra centrifugation filter tube (Milipore, Merck). Before storage at 4°C, the concentration of the remaining dispersion was determined as described above.

Name	Sequence
Docking A_{AU}	5'- /Thiol/ - $(T)_{10}$ GGT GTT GTG TGT GTG GGT GTG TGT GTG - 3'
Docking B_{AU}	5'- /Thiol/ - $(T)_{10}$ CAC ACA CAC ACC CAC ACA CAC AAC ACC - 3'

Table 3.2.: DNA sequences used in section 4.4.3

3.1.2.2. Sample preparation

All AuNP samples were prepared by the following procedure using stock solutions of DNA coated AuNP as prepared in section 3.1.2.1. Depending on the stoichiometry $X_{\alpha-\beta}$, 2 µl of α-particles and a varying amount of β-particles was mixed in a base buffer containing 5 mM Tris. After mixing, 200 mM of NaCl was added to the particle dispersion ($V_{sum} = 20$ µl) to enable particle coagulation *via* DNA hybridization and mixed with a pipette. Subsequently, the particle dispersion was pipetted into an eppendorf tube, a microscopy chamber, a cuvette or a TEM grid as described in the corresponding sections.

3.1.2.3. UV/VIS spectroscopy

UV/Vis spectra of the 10 nm AuNP samples were conducted with a Perkin Elmer lambda 25 spectrometer. The samples were prepared according to section 3.1.2.2 and subsequently pipetted into a 30 µl quartz ultra-micro-cuvette (Hellma analytics). The data was acquired at a scan speed of 480 $\frac{\text{nm}}{\text{min}}$ and a data interval of 1 nm.

3.1.2.4. Electron microscopy

To resolve the nanoparticle coagulates on a single particle level, transmission electronmicroscopy was applied. As the conventional dehydration of the samples often leads to strong artifacts, caused by particle aggregation and salt crystallization, the samples were prepared in a cryo-TEM setup. Accordingly, 3 µl of particle of the sample were pipetted on a TEM copper grid and subsequently treated by a Vitrobot (FEI) and drop-frozen by applying liquid nitrogen. The drop-freezing procedure ensured that the water ice is trapped in an amorphous state, suppressing crystal growth and therefore enabling TEM imaging [120]. After sample preparation the samples were stored in liquid nitrogen until imaging. Finally, the images were recorded with a Tecnai G2.

3.1.2.5. Dark field microscopy

Darf field microscopy (DFM) was used to enable the mesoscopic imaging of AuNP clusters that often have sizes below the resolution limit of conventional light microscopy. In contrast to conventional bright-field microscopy, DFM aims to detect only the scattered light of a sample instead of complete trans-illumination. To achieve this, an oil-immersion condenser with a numerical aperture of 1.4 (Zeiss Ultrakondensor 1.2/1.4) was mounted on a Zeiss Axiovert 200 microscope. The corresponding air-objective (N-Achroplan 63×/0.7) had a significantly smaller numerical aperture of 0.7. This ensured, that the light source itself is not projected into the objective so that only the scattered light of the sample is collected. As a result, nanoparticle clusters down to the size of tens of particles could be detected and imaged. For imaging, a Canon EOS 750D with a 24.2 megapixel APS-C-sensor was deployed.

3.1.3. Macroscopic hybrid polymer-colloid DNA gels

3.1.3.1. Rheology

For rheological measurements, an Anton Paar Physica MCR 301 plate rheometer equipped with a PP08 8 mm upper plate and self-made transparent lower plate to enable controlled light exposure was used. The experiments were conducted in a darkened room to ensure

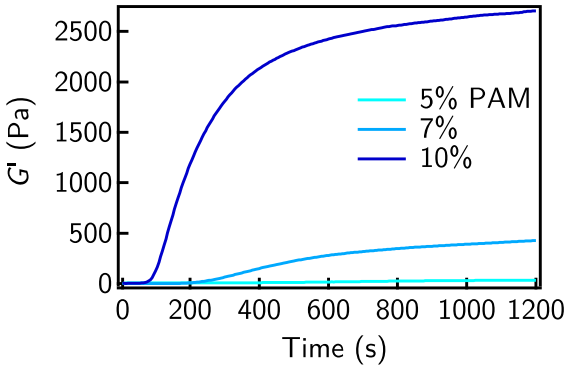

Figure 3.5: Storage modulus measured during PAM polymerization for different concentrations over time. As expected, increasing the concentration of PAM leads to an increase in storage modulus. In experiments, the storage modulus was presumed to be approximately constant after 20 min of polymerization.

that the PAM stays unpolymerized before the microsphere structure formation processes are finished. A detailed description of the rheological parameters studied in this thesis can be found elsewhere [121].

1 µm sized non-fluorescent streptavidin coated polystyrene microspheres were coated with DNA α and β in analogy to section 3.1.1.1, the linker $\overline{\alpha\beta}$ was used to induce coagulation. Samples were prepared in analogy to section 3.1.1.2 at a final volume of $V_{\text{sum}} = 10$ µl and incubated on a rotating device for 1 h to ensure coagulation of large, system-spanning coagulates. Subsequently, the sample was transferred onto the lower rheometer plate by a pipette with a cut-off pipette tip in order to minimize coagulate disruption by shear forces. Then, the upper rheometer plate was lowered to a working distance of 200 µm, followed by a second incubation step of 1 h. After the incubation, the sample was illuminated with a Schott KL 1600 light-emitting diode lamp through the transparent lower plate for 20 min. The polymerization process of the PAM matrix can be monitored by applying an oscillatory shear stress in the linear regime, which allows for measuring the storage modulus (G') and the loss modulus (G'') with time. After 20 min the polymerization process of PAM can be assumed to be finished as G' approximately reaches its asymptotic maximum G'_{max} (see figure 3.5).

3.1.3.2. Printable gels

The printable gel was prepared similar to the rheology samples in section 3.1.3.1. In order to enable quasi-instantaneous PAM polymerization, 6% of PAM,0.625% ammonium persulfate and 140 µM Tris(2,2'-biprydidyl) dichlororuthenium(II) were used at a particle concentration of 5000 ppm. Additionally, 1 M of sucrose was added to generate a suitable surface tension of the solution for printing on the glass coverslide. This ensured, that the lines of fluid generated by the pipette, contained their original geometry and did not spread on the cover slide before PAM gelation.

After mixing in a darkened chamber, the particle dispersion was loaded into a pipette and dragged along a glass microscopy slide, followed by a optical fibre that was illuminated by

a Schott KL 1600 light-emitting diode lamp.
In hybrid-gel mold experiments, two solutions were prepared. First, a PAM base containing 23% Acrylamide 4K solution (29:1) (Applichem), 150 mM NaCl 0.0625% ammonium persulfate and 140 µM Tris(2,2'-biprydidyl) dichlororuthenium(II) was mixed and pipetted into an acryl-glass mold. The mold was created by gluing a acryl-glass grid (see figure 3.6) on a glass cover-slide. The transparent mold enables controlled light-exposure at the end of the experiment. Secondly, a DNAcc dispersion (5000 ppm DNAcc concentration) with high sucrose content (800 mM sucrose, 23% Acrylamide 4K solution (29:1) (Applichem), 150 mM NaCl 0.0625% ammonium persulfate and 140 µM Tris(2,2'-biprydidyl) dichlororuthenium(II), 10 $\frac{mg}{ml}$ BSA) was added on top of the PAM base. Finally, the sample was illuminated with a Schott KL 1600 light-emitting diode lamp for 3 min, resulting a solid-like PAM block with DNAcc as a top layer.

Figure 3.6: Acryl-glass mold for 3D hybrid-gel molding.

3.1.4. Light scattering

Light scattering experiments were conducted with a Jasco FP-8500 spectrofluorometer. As the spectrofluorometer is primarily designed to measure fluorescence signals, it only collects light that is emitted from the sample at 90° angle in respect to the incoming exciting light. As the excitation and the emission wavelength were set to 497 nm with a bandwidth of 5 nm (response time: 4 s), elastically scattered light of the samples was collected. The samples were prepared in analogy to section 3.1.1.2 (without Acrylamide and its polymerization starters) at a final volume of 30 µl. The samples were subsequently pipetted into a 30 µl quartz ultra-micro-cuvette (Hellma analytics) and measured in parallel by a Jasco multisample holder at room temperature. After the measurement was completed, the cuvettes were rinsed with water and sonicated with detergent and ethanol.

3.2. Dynamic structure formation

3.2.1. DNA sequences and coating

The microspheres were coated in analogy to section 3.1.1.1 and stored for no longer than a week at 4°C on a rotating device. The sequences used in chapter 5 are listed in table 3.3.

Name	Sequence
Template	5'- CTA ATA CGA CTC ACT ATA GGG GTT ATA TAG TAA GTT TTG TTG GTT GGT GTG GGT GGG TG - 3'
Template complementary	5'- CAC CCA CCC ACA CCA ACC AAC AAA ACT TAC TAT ATA ACC CCT ATA GTG AGT CGT ATT AG - 3'
Synthesized RNA	5'- GUU AUA UAG UAA GUU UUG UUG GUU GGU GUG GGU GGG UG - 3'

Table 3.3.: DNA sequences used in chapter 5

3.2.2. Sample preparation

In chapter 5, only 1 µm sized non-fluorescent Streptavidin-coated microspheres (Bangs Laboratories) were used. To enable enzymatic activity the low-Tris low-salt buffer was prepared with 30 mM $MgCl_2$ instead of 150 mM NaCl. Consequently, the microspheres were stored in a $MgCl_2$ density-matched buffer (450 mM sucrose, 30 mM $MgCl_2$, 10 mM Tris, pH 8.8). Unless otherwise specified, the microspheres were dispersed in a standard colloidal buffer of 450 mM sucrose, 30 mM NaCl, 10 mM Tris, and 5 mg/mL BSA before experiments. All samples were prepared at a fixed total microsphere volume fraction of 5000 ppm. The coagulation in all samples was induced by adding the appropriate RNA linker strands (see table 3.1) or by RNA polymerization by T7 RNA polymerase. For bright-field microscopy imaging, the samples were pipetted into a glass microscopy chamber and mounted on a microscopy temperature stage. Unless otherwise specified, the temperature stage was calibrated to 37°C by a Voltcraft K204 temperature sensor, to ensure enzymatic activity.

3.2.3. Fluorescence measurements

Bulk fluorescence measurements were performed with a Jasco FP-8500 spectrofluorometer. Samples were prepared according to section 3.1.2.1, pipetted into a 30 µl quartz ultra-micro-cuvette (Hellma analytics) and the measurement was started subsequently. As a fluorescent dye for RNA detection, 0.55 µl 1:10 dilution of SYBR Green II (ThermoFisher) was added to each sample at a total sample volume of 30 µl. The fluorimeter was equipped with a Xe-lamp that allowed for excitation between 200-900 nm with a minimum spectral width of

1 nm. The samples were excited at 497 nm with a spectral width of 1 nm and the emitted light was detected at an angle of 90° at 530 nm with a spectral width of 5 nm. Unless otherwise specified, the samples were placed in a passive temperature controlled multi-sample holder. The temperature inside the cuvettes was calibrated to 37°C by a Voltcraft K204 temperature sensor. After the measurement was completed, the cuvettes were rinsed with water and sonicated with detergent and ethanol. In order to quantify the production

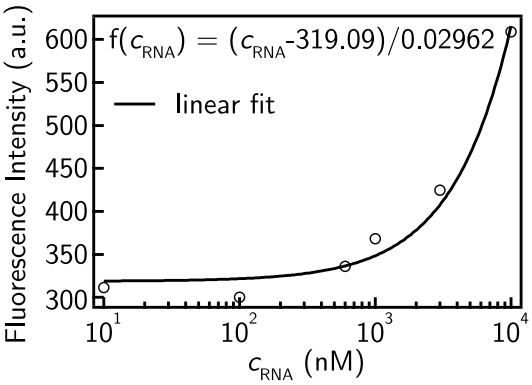

Figure 3.7: Fluorescence signal calibration for RNA detection. At standard conditions (c_{NTP} = 0.46 mM, $c_{template}$ = 0.91 µM) the sensitivity of the assay is limited to ≈ 200 nM.

and degradation rates of RNA, a calibration curve for the fluorescence signal for different RNA concentrations at standard buffer conditions containing a standard concentration of NTPs (0.46 mM) and templates (0.91 µM) was determined (see figure 3.7). The calibration curve shows that detection limit of this method lies at ≈ 200 nM. This detection limit arises from the fact that also dsDNA templates are present in the sample, giving the baseline in figure 3.7. As a consequence, this calibration curve is in an absolute sense only valid for the described calibration buffer and template concentration. However, the rates of RNA production are independent of the baseline and can therefore be calibrated using this curve also for other template concentrations.

3.2.4. Bright field light microscopy

Bright field light microscopy on dynamic structure formation samples was performed with a Leica HCX PL Apo 40×oil objective on a Leica DMr 6000B microscope. Images were recorded with a Hamamatsu ARCA-ER controller that was operated by the Micro-Manager open source microscopy software (v. 1.4).

3.2.5. Gel electrophoresis

Native polyacrylamide gelectrophoresis (native PAGE) was performed in a 18% polyacrylamide TBE gel. The separating gel was prepared with 18% Acrylamide 4K solution (Applichem), 3.7 µM EDTA, 0.3% ammonium persulfate and 8 mM N,N,N',N'- Tetramethylethylenediamine (TEMED) in Tris-Borat-EDTA-buffer (TBE, 89 mM Tris, 89 mM

boratic acid, 2 mM EDTA, pH 8.0). The separating gel was poured in a vertical electrophoresis chamber. After 10 min, the collecting gel (3.6% Acrylamide 4K solution, 1 µM EDTA, 0.3% ammonium persulfate and 10 mM TEMED in TBE-buffer) was poured on top of the separating gel and allowed for 1 h of polymerization. The samples were mixed with 5× loading dye (Qiagen gelpilot) at a final concentration of 5 µM and subsequently loaded into the gel. The gel typically was subjected to 100 V for 1.5 h in 1×TBE buffer and subsequently stained. Staining was performed in 100 ml 1:5000 SYBR Green II in 1×TBE buffer for 20 min. After rinsing with water, the gel was imaged in UV Gel-chamber.
Depending on the length of the target RNA or DNA strand, this PAGE was capable of resolving a length difference of a few nucleotides and strand lengths up to 300 nt (see figure 3.8).

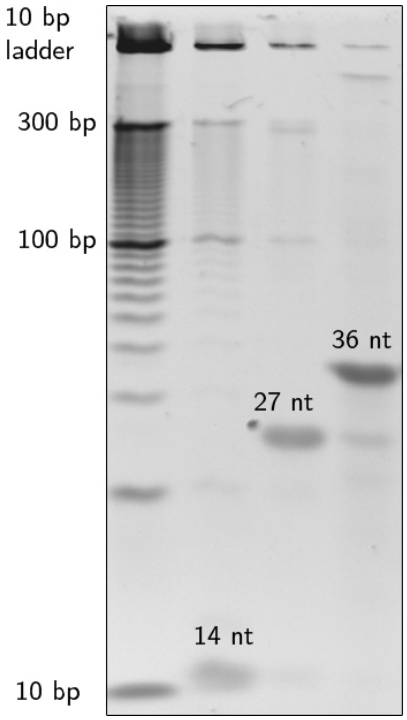

Figure 3.8: Native polyacrylamide gelectrophoresis (PAGE) with a 18% polyacrylamide TBE gel. The gel is capable of resolving DNA and RNA fragments between 10–300 nt/bps. The control experiment with commercially synthesized DNA fragments shows that differences of a few nucleotides can be resolved.

4. Static Structure Formation by DNA coated colloids

In this chapter the structure formation by DNA coated colloids far from equilibrium will be investigated on different length scales. These structure formation processes are triggered by specific DNA interactions of binding energies $E_B \gg k_B T$, thus leading to fast coagulation and quasi-irreversible binding. As a result, the formed structures can be considered static in a sense that they are not capable of rearranging or disintegrating without human intervention.

While it is known that in this regime, homocoagulation leads to the formation of fractal gels of defined fractal dimensions, heterocoagulation of binary, ternary or higher order systems has not been studied in detail. The aim of this chapter is to shed light on these heterocoagulation processes in terms of basic mechanisms that govern structure formation but also in terms of complex self-organiziation. The data show that binary heterocoagulation can be utilized to create finite-sized clusters of different sizes and geometries. Moreover, ternary heterocoagulation enables the formation of polar structures that can be classified as junctions. These junctions in turn lead to the rational design of a complex hierarchical coagulation process that allows for the self-organization of distinct mesoscopic objects of up to 26 µm within a few hours. Most data of these structure formation processes have been published [122].

Finally, different applications are presented to show that the found principles of structure formation far from equilibrium can be utilized to create novel applications ranging from the nano- to the macroscale.

4.1. Binary heterocoagulation

4.1.1. Fractal growth

Although DNA coated colloids have been studied in a myriad of self-organization systems (see section 2.2), systematical studies that investigate heterocoagulation of DNAcc far from equilibrium in terms of fractal growth have not been reported.

In order show that the chosen system of DNA coatings and linker strands results in specific aggregation and fractal growth, a binary system of *A*-microspheres (coated with docking-

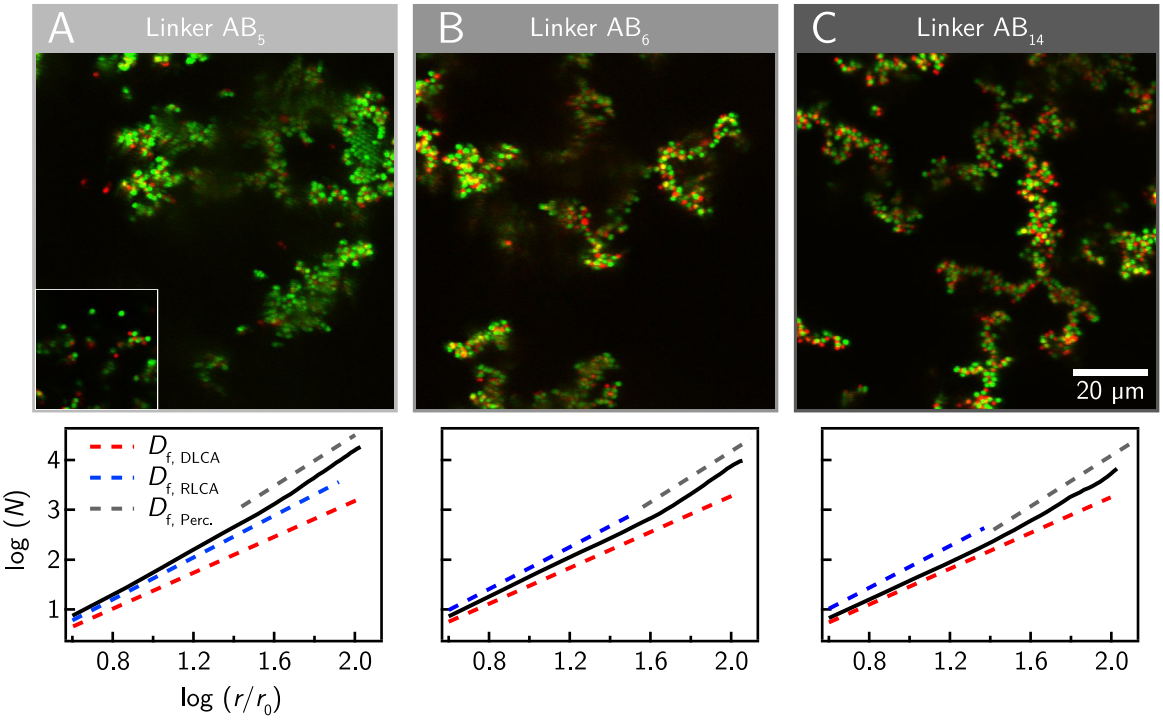

Figure 4.1.: Morphological comparsion of different fractal gels formed by a binary system of DNA coated colloids. The heterocoagulation of the two microsphere species A (red) and B (green) is triggered by the addition of the ssDNA linker strand $\overline{AB}_x$, where x represents the number of nucleotides available for binding B spheres. (A) At $x = 5$ the coagulation process leads to a fractal gel close to the RLCA limit. (B) Increasing to $x = 6$ already results in DLCA like morphologies. (C) At $x = 14$ the DLCA limit is reached.

DNA A) and B-microspheres (coated with docking-DNA B) was investigated. A- and B-DNA was designed in a way that they do not exhibit significant equilibrium binding. However, on addition of a linker strand ($\overline{AB}_x$) that is fully complementary to A (21 nucleotides), but only partially complementary to B (by $x = 5 \ldots 14$ nucleotides), the inter-particle potential is altered. This leads to the formation of an energetic minimum (see section 2.2) that can be varied in depth by varying the length of AB_x. Indeed, choosing $x = 11$ at a fixed linker concentration (for details see section 3.1.1.2) leads to the formation of a fractal gel that has a typical DLCA-like morphology after 2h (see figure 4.1C). While reducing to $x = 6$ still leads to the same morphology (see figure 4.1B), $x = 5$ shows no complete gelation after 2h (see figure 4.1A, inset). However, additional incubation of 2h leads to near gelation with significantly denser structures (see figure 4.1A).

Calculating the mass fractal according to equation 3.3 reveals that this difference in morphology can also be captured quantitatively. The longest linker, $x = 14$, exhibits a mass fractal that is very close to the DLCA limit. This shows that at $x = 14$ a purely diffusion limited coagulation process can be expected. However, at $x = 5$, the denser structures, that form over a significantly longer time span, are reflected in a mass fractal that is comparable

to the RLCA limit. Consistently, the linker $\overline{AB}_6$ represents an intermediate between these two extreme cases.
Moreover, all investigated $\overline{AB}_x$ triggered structures showed a deviation in the mass fractal at $\log\left(\frac{r}{r_0}\right) > 1.6$. This deviation is consistent with what is expected from literature [29][30]. It can be interpreted as a transition from the flocculation to the percolation regime, where large clusters start to interpenetrate and arrest in their current position (see section 2.1.1.2).

4.1.2. Controlling cluster size and geometry

As it has been shown in section 4.1.1, a binary system of DNAcc can be used to create fractal gels that behave like DLCA or RLCA. These gels represent scale-free objects that span from the micro- to the macroscale. However, their growth is only limited by the finite pool of material available for structure formation. In this section it will be investigated how cluster size and geometry can be controlled in such a binary system of DNAcc in order to enable a more complex self-organization of multicomponent DNAcc far from equilibrium.
In the binary colloidal system presented here, the DNA sequences α and β are equivalent to $\overline{AB}_{14}$ (see section 3.1.1.1). This ensures that upon addition of the linker strand $\overline{\alpha\beta}$, α– and β–spheres can interact with each other in a DLCA like process leading exclusively to fast heterocoagulation. However, if the stoichiometry of α– to β–spheres $X_{\alpha-\beta} = \frac{c_\alpha}{c_\beta} \neq 1$, the symmetric and therefore unlimited coagulation of the microspheres will be distorted. With increasing $X_{\alpha-\beta}$ the probability increases that microspheres of the minority type (here: β–spheres) will be saturated with majority type microspheres (here: α–spheres) before gelation, resulting in an effective screening of both particles types for further interactions and thus isolated clusters (see section 4.1.4 for detailed discussion an modeling). As a result, an increment of $X_{\alpha-\beta}$ should directly yield a control over cluster size.
Confocal measurements could verify this model (see figure 4.2). Quantitative image analysis (as described in section 3.1.1.5) shows that the number average cluster size and its standard deviation are highly dependent on $X_{\alpha-\beta}$ (see figure 4.2A). However, the mass average cluster size of the assembled clusters shows an even larger dependency and significantly lower standard deviations (see figure 4.2B). The discrepancy between these two statistical averages is caused by the asymmetric shape of the cluster size distributions (see figure 4.2C,i–vi). At $X_{\alpha-\beta} = 4$, the heterocoagulates are able to grow into large, branched structures with a fractal dimension D_f that is comparable to the DLCA limit (see figure 4.3A). The assembled structures can therefore be understood as growth restricted fractals that grow with minority spheres acting as aggregation seeds. Only a small minority of microspheres is found in unbranched clusters or compact clusters ($= 1$ central minority sphere) (see figure 4.3B). This leads to a broad distribution of differently sized clusters and a large standard deviation

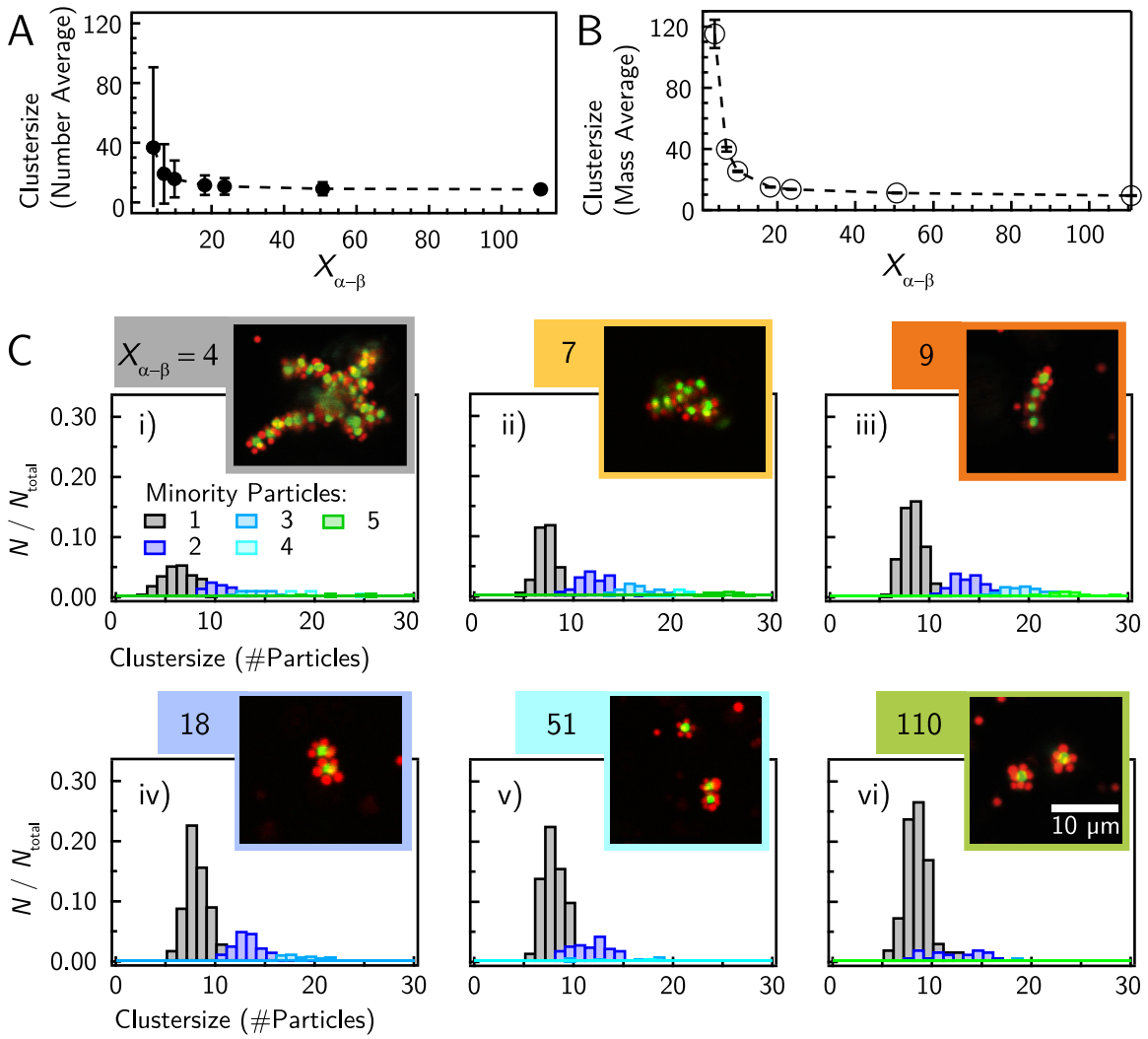

Figure 4.2.: Controlling the cluster size in a binary heterocoagulation experiment. (*A*) Increasing the stoichiometry $X_{\alpha-\beta}$ between α- and β- spheres leads to a monotonous decrease in the average cluster size. (*B*) As the cluster sizes exhibit an asymmetric distribution, the mass average of the cluster sizes has an enhanced capability of capturing this effect. (*C*) Example confocal slices and quantitative cluster size distribution histograms for different stoichiometry $X_{\alpha-\beta}$ colored by the number of minority spheres encapsulated in the clusters. While at (i) $X_{\alpha-\beta} = 4$ large clusters are able to grow and a broad cluster size distribution is found, increasing up (vi) $X_{\alpha-\beta} = 110$ leads to a sharp distribution containing only one minority sphere.

of the number average clustersize (see figure 4.2A, C(i)). Consequently, increasing $X_{\alpha-\beta}$ results in a shift in the cluster size distributions and their geometrical composition. As the cluster growth is further restricted to less aggregation seeds, the formation of branched and fractal structures is increasingly suppressed at $X_{\alpha-\beta} = 9$, yielding structures where most spheres are found in unbranched, i.e. linear clusters (see figure 4.3B). This bias towards linear structures is also reflected in the continuous decrease of D_f with higher $X_{\alpha-\beta}$ (see

figure 4.3A)). At $X_{\alpha-\beta} = 110$ most spheres are found within clusters of only one central minority sphere. The minority particles, which act as aggregation seeds, stay isolated, yielding compact, highly monodisperse clusters of the same minimal size (see figure 4.3B). The standard deviation in the number average of this cluster size distribution is consequently very low (see figure 4.2A).

An analytic model based on Smoluchowski's concept of fast coagulation theory [38] was developed and will be discussed in section 4.1.4. This purely diffusion based model is able to predict a critical concentration $X_{\text{growth}} \approx 22.3$ where cluster growth is predominantly restricted to compact clusters. Also experimentally it was found that at $X_{\text{growth,exp.}} \approx 21.8 \pm 0.8$ compact clusters stop to dominate the mass average of the clusters (see section 4.1.4 and figure 4.6C). From this experimental data, three functional or geometrical regimes of cluster growth can be defined. At $X_{\alpha-\beta} < 8$ fractal DLCA like structures of a limited size emerge, thus being called the fractal regime. At intermediate $8 < X_{\alpha-\beta} < X_{\text{growth}}$, branching of the clusters is effectively suppressed, yielding mostly unbranched clusters that form the linear regime. Finally, at $X_{\alpha-\beta} > X_{\text{growth}}$ the compact regime is reached, where compact clusters dominate the mass average of the clusters.

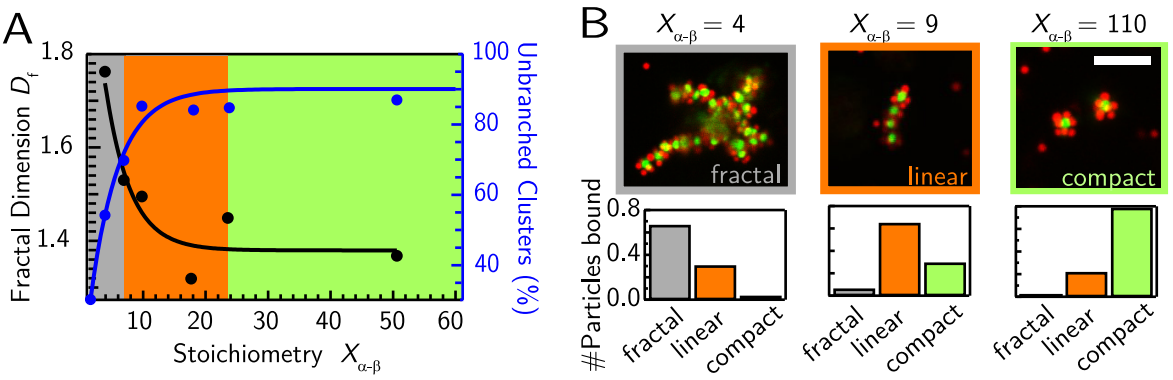

Figure 4.3.: Geometrical classification of binary heterocoagulates into three regimes. (*A*) At $X_{\alpha-\beta} < 8$ the clusters grow into branched, fractal structures that exhibit a fractal dimension that is comparable to the DLCA limit. At intermediate $8 < X_{\alpha-\beta} < X_{\text{growth}}$ the branching of the clusters is suppressed, resulting in smaller, mostly linear structures. Finally, at $X_{\alpha-\beta} > X_{\text{growth}}$ is highly restricted to compact clusters that contain only one minority sphere. (*B*) Example confocal slices and geometrical cluster distributions for each regime. The number of bound particles in each geometrical regime clearly seperates the three proposed regimes. Scale bar 10 µm.

4.1.3. Time-evolution in binary systems

In order to get further insight into the previously defined functional regimes of cluster formation in a binary system of fast heterocoagulation, time course measurements have been performed with confocal microscopy.

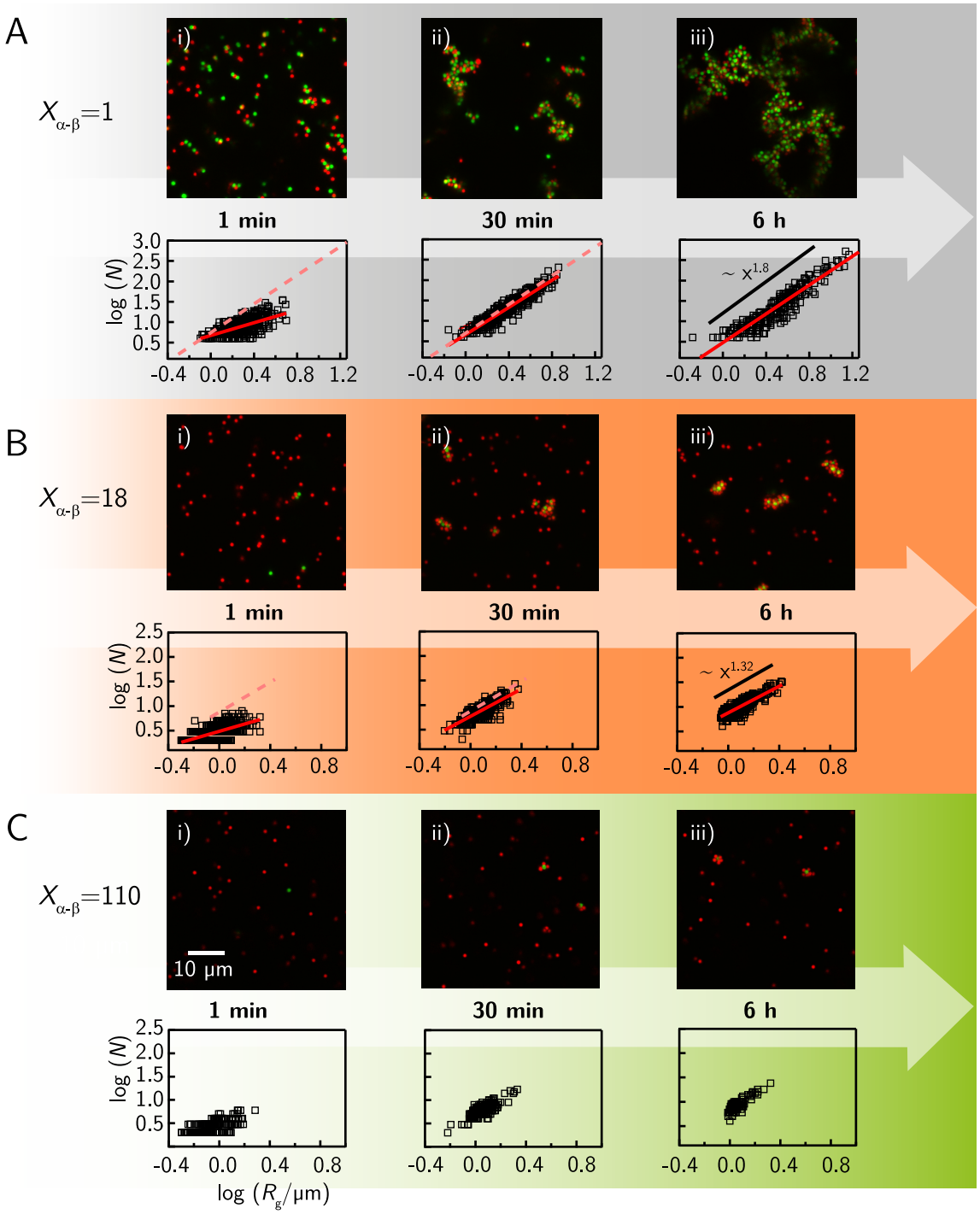

Figure 4.4.: Time evolution in binary heterocoagulation for different $X_{\alpha-\beta}$. (*A*) At $X_{\alpha-\beta} = 1$, fractal growth takes place as expected from section 4.1.1, resulting in fractal coagulates close to the DLCA limit after 30 min. (*B*) In the linear regime at $X_{\alpha-\beta} = 18$, fractal growth is limit to smaller clusters, but also to a significantly lower fractal dimension. Moreover, the fractal limit is reached within comparable timescales. (*C*) In the compact regime at $X_{\alpha-\beta} = 110$, mostly clusters containing only one minority sphere can be found. Due to the lack of larger coagulates, robust fractal analysis cannot be conducted in this regime.

At $X_{\alpha-\beta} = 1$ fractal growth in the DLCA limit is observed (see figure 4.4A). Already at $t = 1$ min clusters containing up to ≈ 30 particles can be observed, indicating the rapid structure formation that is expected from a DLCA process. The fractal dimension of these clusters lies well below the DLCA limit (see figure 4.4A(i)). However, within 30 min the classical DLCA limit is reached, with maximum cluster sizes of up to ≈ 300 particles (see figure 4.4A(ii)).
In the linear regime at $X_{\alpha-\beta} = 18$, the cluster size distribution starts similar to $X_{\alpha-\beta} = 1$. Only small clusters with a low D_f can be found (see figure 4.4B(i)). In contrast to $X_{\alpha-\beta} = 1$, the clusters stay well below the DLCA limit also after $t = 30$ min, reflecting the significant amount of linear clusters within the sample. After 6 h the cluster formation is in its final form at $D_f = 1.32$, quantitatively solidifying the visual evidence for linear growth. This is in good agreement with the mechanism proposed in section 4.1.2. As fractal growth has the tendency to take place at the exposed ends of a growing structure [123], limiting fractal growth to small clusters will directly result in unbranched structures.
Consequently, choosing $X_{\alpha-\beta} = 110$ will limit fractal growth to the smallest entities of binary heterocoagulation, which are mostly isolated minority spheres that are saturated by majority spheres 4.4C).
Analysis of the time course of other key figures supplements this model. While the average cluster size continuously increases over 6 h for $X_{\alpha-\beta} = 1$ (see figure 4.5A(i)) it has reached more than 90% of its final value for $X_{\alpha-\beta} = 18$ and $X_{\alpha-\beta} = 110$ after $t_{\text{bin}} = 30$ min (see figure 4.5B,C(i)). t_{bin} can therefore be defined as characteristic time for binary heterocoagulation at the chosen particle concentration. How the formation of large clusters is suppressed at high $X_{\alpha-\beta}$ can quantitatively be seen by monitoring how many spheres are bound in which cluster type over time. For $X_{\alpha-\beta} = 1$ already after 10 min, nearly all micro-spheres are bound in coagulates (see figure 4.5A(iii)). The majority of spheres is bound in cluster with more than 5 minority particles, which represent fast fractal growth (see figure 4.5A(ii)). However, in the beginning at $X_{\alpha-\beta} = 18$ most spheres are bound in seeds, i.e. they are bound to 1 minority sphere. These seeds further coagulate to larger coagulates over the next 30 min, resulting in a scenario, where most micro-spheres are bound in coagulates with 2 or more minority spheres (see figure 4.5B(ii)). As expected, $X_{\alpha-\beta} = 110$ results in an extreme case of binary heterocoagulation, where $\approx 90\%$ of all bound spheres are bound in aggregation seeds. Only very few small coagulates containing 2 or 3 minority spheres can be found (see figure 4.5C(ii)). At both $X_{\alpha-\beta} = 18$ and $X_{\alpha-\beta} = 110$ the minority spheres are bound rapidly (≈ 1 min) leaving behind many unbound majority spheres (see figure 4.5B,C(ii)).

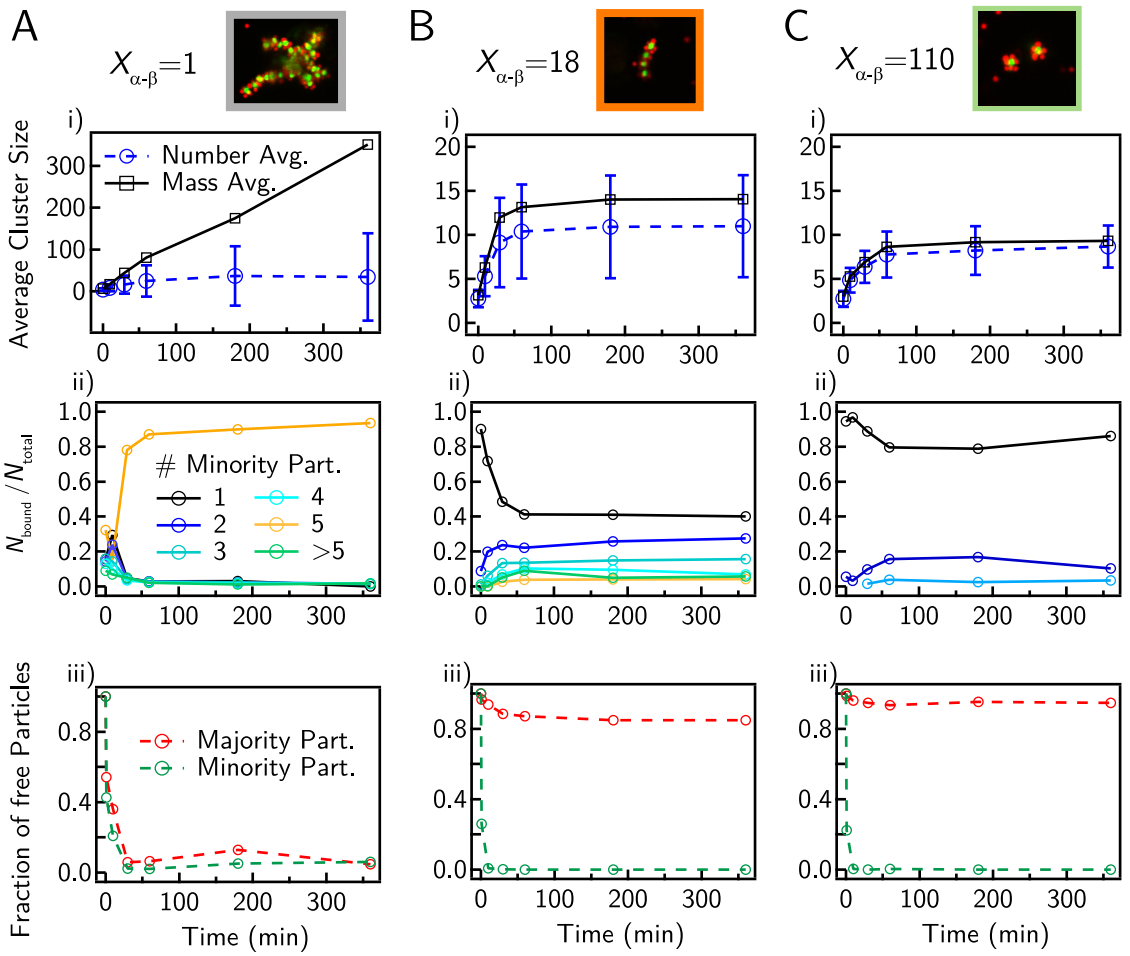

Figure 4.5.: Time evolution of different key parameters of binary heterocoagulation. (*A*) (i) At $X_{\alpha-\beta} = 1$, the average cluster size rapidly increases, showing a monotonous increase also after 6h. (ii) The detailed time evolution of the differently sized clusters shows that most particles are bound in large coagulates with more that 5 minority spheres after 10min. (iii) In this timescale nearly all free spheres are bound in clusters, yielding no significant difference between the two sphere species. (*B* and *C*) At $X_{\alpha-\beta} = 18$ and $X_{\alpha-\beta} = 110$, the average cluster size reaches its asymptotic maximum after $\approx$ 1h. While at $X_{\alpha-\beta} = 18$ most spheres are bound in clusters containing more than one minority sphere (*B*(ii)), nearly 90% of all spheres are bound in single minority sphere clusters at $X_{\alpha-\beta} = 110$ (*C*(ii)). At both stoichiometries, the minority spheres are adsorbed within 10min, showing the highly asymmetric behavior of majority and minority spheres.

4.1.4. Analytical model

An analytical model was developed to solidify the presented experimental findings. This model is based on Smoluchowski's concept of fast coagulation [38], but can also be derived from Langmuir adsorption theory [124][125]. Smoluchowski first introduced the fast coagulation rate $W_K = 8\pi DRc$ as the rate at which two spherical particles of diffusion coefficient

D, radius R and concentration c meet. Using the Stokes-Einstein equation $D = \frac{k_B T}{6\pi\eta R}$, W_k can be written as $W_K = \frac{4ck_B T}{3\eta}$, losing its dependency on R. However, it is important to note that this is only valid in the limit of spherical particles. If anisotropic particles such as prolate ellipsoids are to be used in experiments, the rather complex dependency of D on the semi-principal axes of the ellipsoids [126] has to be taken into account, preventing further condensation of W_K. Furthermore it has been shown in literature that also the hydrodynamic coupling of the spheres plays a significant role in aggregation rates. It can be estimated that this reduces the fast coagulation rate by a factor of $\mu = 0.54$ [127]. For pseudo-irreversible processes such as they are investigated here, this is also the rate at which two spheres bind. In a simplified system, where one sphere A (minority sphere) with radius R is surrounded by an infinite number of majority spheres B with Radius R, that cannot bind themselves, but only the minority sphere A, the binding probability of A to B can be written as

$$W_{AB} = \frac{4\ c_B k_B T \mu}{3\eta} Y(t) = W_K Y(t) \quad , \tag{4.1}$$

where $N(t)$ is the number of B bound to A and N_{max} is the maximum number of bound spheres bound to A. The accumulated number of B spheres on A with time is therefore

$$dN = W_{\text{AB}} dt \tag{4.2}$$

resulting in

$$N(t) = N_{\text{max}} \left(1 - \exp\left(-\frac{W_K t}{N_{\text{max}}}\right)\right) \tag{4.3}$$

for the boundary conditions $N(0) = 0$. Reducing the number of B spheres from infinity to a finite reservoir of $X_{\text{B-A}}$ the concentration c_B is effectively reduced in time by the factor $\theta = \frac{X_{\text{B-A}} - n(t)}{X_{\text{B-A}}}$. Inserting this into equation 4.2 and subsequent solving for $N(0) = 0$ yields

$$N(t) = N_{\text{max}} \left(\frac{1 - \exp\left(\frac{W_K (X_{\text{B-A}} - N_{\text{max}})}{N_{\text{max}} X_{\text{B-A}}}\right)}{1 - \frac{N_{\text{max}}}{X_{\text{B-A}}} \exp\left(\frac{W_K (X_{\text{B-A}} - N_{\text{max}})}{N_{\text{max}} X_{\text{B-A}}}\right)}\right) \quad . \tag{4.4}$$

In a regime where no multimerization occurs and the described accumulation process is the dominating process, equation 4.4 is a valid approximation for an ensemble of spheres. In this case, $N(t)$ is the average number of accumulated B spheres on A spheres and N_{max} is the maximum of accumulated spheres on A spheres averaged over all A spheres. Consequently, $X_{\text{B-A}}$ is the stoichiometry between B and A particles $X_{\text{B-A}} = \frac{c_B}{c_A}$. According to experiments, N_{max} is best approximated by $N_{\text{max}} = 6.8$ (see figure 4.6A). As the temperature and the viscosity of the sample can be measured experimentally, there are no remaining free variables in equation 4.4. Time course measurements at $X_{\text{B-A}} > 90$ for different concentrations show

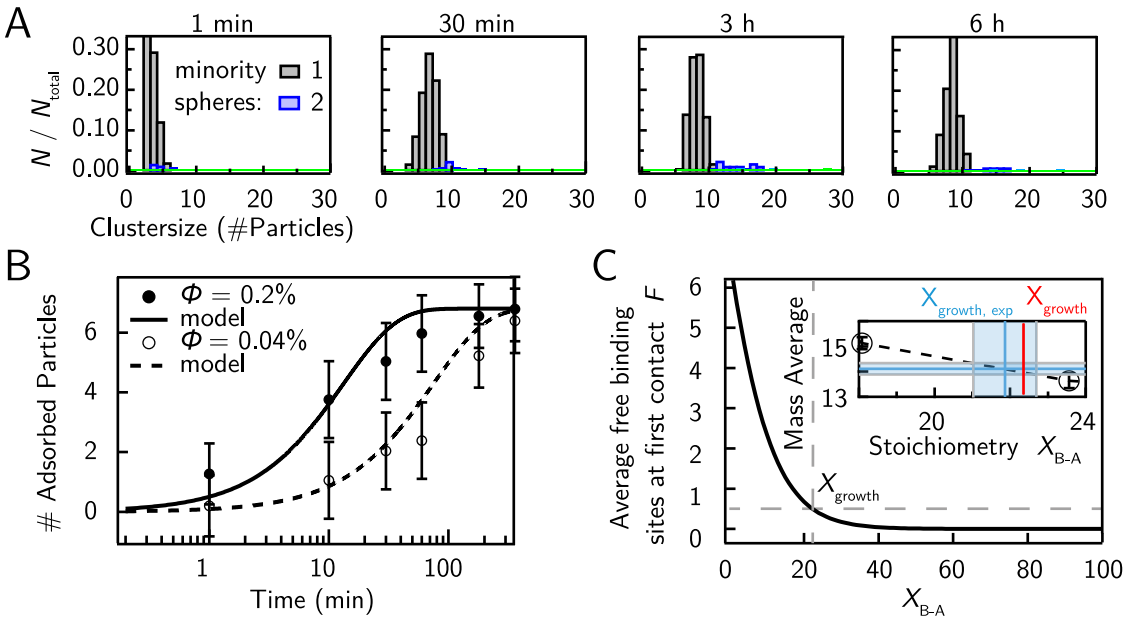

Figure 4.6.: Analytic model for binary heterocoagulation at high stoichiometries. (*A*) Experimental data shows that at a stoichiometry of $X_{A-B} = 110$ binary heterocoagulation is reduced to aggregation of majority spheres on minority spheres. (*B*) Model predictions of equation 4.4 and experimental data for different microsphere volume fractions Φ. (*C*) Prediction of the model concerning the formation of isolated aggregation seeds (see equation 4.8). The red line marks 50% free-binding sites on a minority particle on first contact with another minority particle. Consequently the stoichiometry $X_{\text{growth}} = 22.3$ can be considered a critical stoichiometry for cluster growth. (Inset) Closeup of figure 4.2 with the estimated $X_{\text{growth,exp}}$ in comparison to the predicted X_{growth}. Error bars denote the SD of the underlying cluster distribution.

that the model predictions of equation 4.4 are in good agreement with experimental data (see figure 4.6B) ,where only compact clusters with one minority sphere per cluster have been evaluated. Interestingly, also Langmuir adsorption theory leads to the same result. It has been shown elsewhere [125], that an irreversible adsorption of spheres from a finite reservoir to a surface can be described by

$$n(t) = n_{\max}\left(\frac{1-\exp(-k_{\text{on}}(c_0-c_{\max})t)}{1-\frac{c_{\max}}{c_0}\exp(-k_{\text{on}}(c_0-c_{\max})t)}\right) \quad . \tag{4.5}$$

The Langmuir description lacks the explicit form of k_{on}, but comparison to equation 4.4 yields

$$k_{\text{on}} = \frac{W_K}{N_{\max}c_B} = \frac{4k_BT\mu}{3\eta N_{\max}} \quad . \tag{4.6}$$

Hence it follows, that the binary heterocoagulation process can also be modeled by an irreversible Langmuir adsorption process with a purely kinetic on-rate, where the sum of

surfaces of the minority spheres represents the total adsorbing surface.
As equation 4.4 describes the the accumulation of majority on minority spheres, the stoichiometry at which minority spheres are predominantly occupied by majority spheres when they meet other minority spheres on average for the first time can be estimated. This can be done by evaluating equation 4.4 at the fast aggregation time τ_{AA} of minority spheres

$$\tau_{AA} = \frac{1}{W_{AA}} = \frac{3\eta}{4c_A k_B T \mu} \quad , \tag{4.7}$$

resulting in

$$N(\tau_{AA}) = N_{\max} \left(\frac{1 - \exp\left(-(\frac{X_{\text{B-A}}}{N_{\max}}) - 1\right)}{1 - \frac{N_{\max}}{X_{\text{B-A}}} \exp\left(-(\frac{X_{\text{B-A}}}{N_{\max}}) - 1\right)} \right) \quad . \tag{4.8}$$

The function

$$F(X_{\text{B-A}}) = N_{\max} - N(\tau_{AA}) \tag{4.9}$$

represents an approximation for the average free binding sites F on a minority sphere on first contact with another minority sphere (see figure 4.6C). The stoichiometry X_{growth} at which only 0.5 binding sites are available on first contact, can be calculated numerically, resulting in $X_{\text{growth}} = 22.3$. This value represents the critical stoichiometry at which more than half of the minority spheres are saturated on first contact, inhibiting further growth of the aggregates. To compare X_{growth} to experimental data, the following estimation can be used. As X_{growth} marks the point at which approximately 50% of aggregation seeds are able to merge to bigger clusters, it should in turn experimentally reflect the stoichiometry at which the mass average of the clusters is increased by 50% in relation to the compact regime of aggregation seeds. The data point $X = 110$ (see figure 4.2) and its error was chosen as a reference for the compact regime. Accordingly, a 50% increase of the mass average is found at $X_{\text{growth,exp}} = 21.8 \pm 0.6$, which is in good agreement with X_{growth} (see figure 4.6C, inset). As equation 4.8 is not dependent neither on the size of the spheres, nor of their concentration, X_{growth} can be considered a universal, scale-free constant, applicable to all binary spherical particle systems that are purely diffusion limited.

4.2. Ternary heterocoagulation

4.2.1. Equally sized colloids

In order to show that also a three-micro-sphere, i.e. ternary system can be introduced using DNAcc far from equilibrium, a system of three different colloids of the same size ($= 1$ µm), but of different DNA coating α, β and γ was investigated.

It is expected, that on addition of the linker strands $\overline{\alpha\beta}$ and $\overline{\gamma\beta}$, α- and γ-spheres both start to bind to β-spheres leading to a competitive binding process. Consequently, in the compact regime ($X_{\gamma-\beta} + X_{\alpha-\beta} \geq 30$), predominantly compact isolated aggregation seeds should be found that have a composition that reflects the stoichiometries $\overline{\alpha\beta}$ and $\overline{\gamma\beta}$ (see figure 4.7A).

The data indeed shows that a balanced stoichiometry of γ- and α-spheres ($X_{\gamma-\beta} = 1$) leads to an equally bound number of these two colloidal species to β-spheres (see figure 4.7B). Decreasing the stoichiometry $X_{\gamma-\beta}$ results in a depletion of γ-spheres, until there is on average only one γ-sphere bound to a β-sphere. As the maximum number of bound majority spheres to minority spheres is $n_{\mathbf{max}} = 6.8$ (see figure 4.6B), the stoichiometry at which β-spheres are on average covered by only one γ and several α -spheres equals $X_{\gamma-\alpha} = \frac{1}{6.8} = 0.147$. Experimentally $X_{\gamma-\alpha} = 0.12$ is found, which is in good agreement with the expected value. Consequently, this value reflects the stoichiometry at which the coagulates consist of one γ-sphere and several α-spheres, hence exhibiting polar order (see figure 4.7B, lowest red dashed line). Increasing the stoichiometry $X_{\gamma-\alpha}$ above 1 symmetrically leads to the same result. It is obvious that at a ratio of $X_{\gamma-\alpha} = 6.8$ the average cluster contains only one α-sphere (see figure 4.7B, highest red dashed line)

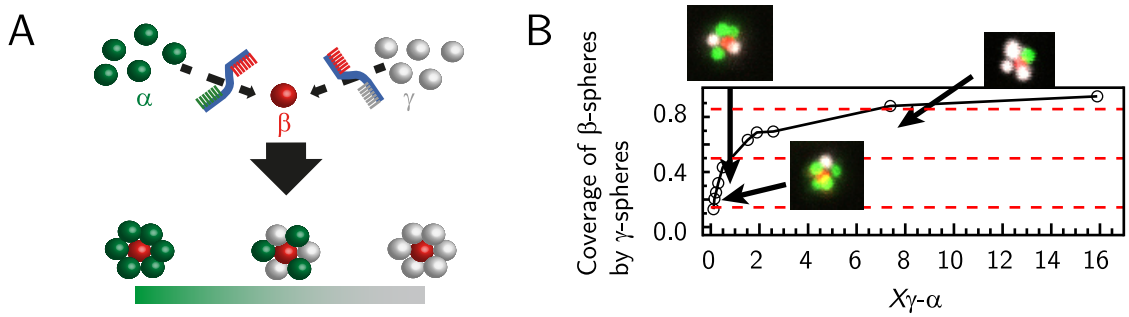

Figure 4.7.: Ternary aggregation of equally sized microspheres in the compact regime. (*A*) Introducing two microsphere species α and γ that can exclusively bind to β-spheres results in competetive binding that allows for controlling the internal structure of the clusters. (*B*) A balanced stoichiometry of white γ- and green α-spheres ($X_{\gamma-\beta} = 1$) leads to an equally bound number of these two colloidal species to a red β-sphere (centered red dashed line). Decreasing the stoichiometry $X_{\gamma-\beta}$ results in a depletion of γ-spheres, until there is on average only one γ-sphere bound to a β-sphere (lower red dashed line), reflection a stoichiometry at which the coagulates exhibit polar order. Increasing the stoichiometry $X_{\gamma-\beta}$ above 1 symmetrically leads to the same result.

4.2.2. Differently sized colloids for asymmetry

As it has been shown in section 4.2.1 ternary heterocoagulation of equally sized micro spheres can be used to control the composition of spheres within clusters in the compact

regime. Also polar objects could be obtained, offering an opportunity for directional binding to these clusters. However, these polar clusters only emerge at a narrow range of stoichiometries $X_{\gamma-\alpha}$, thus yielding very limited options for further mutli-component self-organization processes. In order to further enhance the polar regime of compact ternary heterocoagulation, it is possible to extend ternary heterocoagulation to differently sized spheres. Instead using α- β- and γ-spheres of the same size, Γ-spheres of the double the size (2 µm) were used. By this, a geometrical constraint is introduced, which results in an even more effective

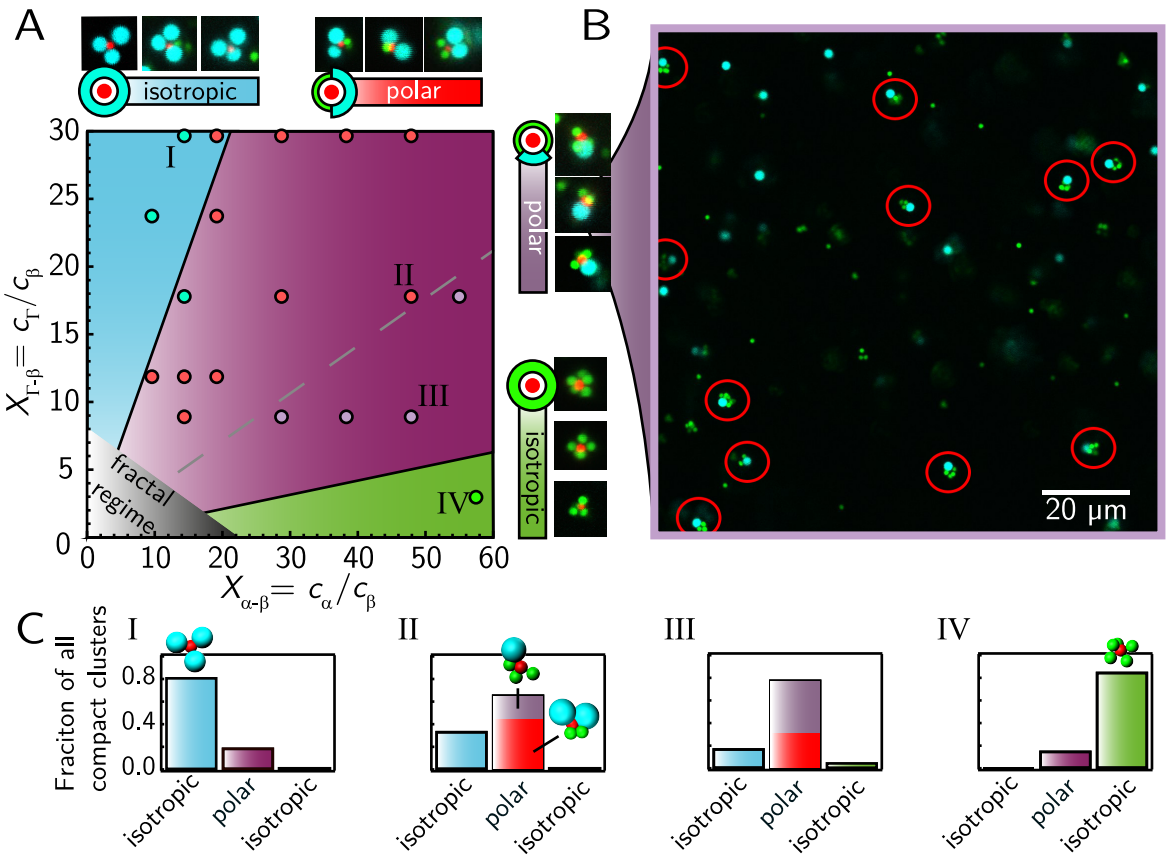

Figure 4.8.: Ternary aggregation of differently sized microspheres. (*A*) Adding a a third, larger spherical particle enables the formation of polar objects at varying stoichiometries. Besides the two isotropic regimes (blue area and blue markers, green area and green markers), that correspond to binary heterocoagulation described in section 4.1, a regime of polar structures (purple area, red and purple markers) is found, where the majority type of formed clusters is of polar order. (*B*) Representative confocal image purified solution of polar clusters. Purification was performed using a magnetic separation technique (see section 3.1.1.3). (*C*) Change in cluster distribution illustrated by four example stoichiometries. Whereas in the blue and green regimes more than 80% of the clusters are isotropic (I, IV), the majority of clusters remains polar in the purple regime (II, III). The exact position in the phase diagram is relevant for the polar substructure (II, III). The shown pictograms of single clusters are 3D renderings of confocal data.

blocking of potential binding sites on the same β-hemisphere for the α-spheres, resulting in

a large polar regime. At $X_{\Gamma-\alpha} \ll 1$, only isotropic clusters are observed, as the ternary aggregation process is basically reduced to a binary problem (see figure 4.8A, green markers). However, increasing $X_{\Gamma-\alpha}$ leads to the cross-over to a regime where both α- and Γ-spheres can bind to a β-sphere, yielding true ternary clusters. The majority of the resulting clusters are polar and harbor only one large Γ-sphere and multiple α-spheres (see figure 4.8A, purple markers). Consistently, a further increment of $X_{\Gamma-\alpha}$ leads to the binding of not only one but two Γ-spheres to one β-sphere. In contrast to equally sized γ-spheres, the use of larger Γ-spheres preserves polarity also in this regime (see figure 4.8A, red markers). Only if the concentration of Γ-spheres is drastically increased to $X_{\Gamma-\alpha} \gg 1$, so that three or four Γ-spheres are bound to one β-sphere, polarity is lost again due to an effective screening of the α-spheres (see figure 4.8, blue markers).
The data show that a wide range of concentration of α- and Γ-spheres can be used to design polar structures with distinct composition (see figure 4.8C). This variety of compact junction-type structures opens up the possibility to aim for higher-order structures based on a hierarchical DLCA process. However, this idea of self-organization far from equilibrium in the compact regime also leaves behind the majority of majority types spheres, as they are not part of the assembly and therefore remain unbound (see also section 4.1.3). To remove these free majority type spheres, magnetic particle separation techniques can be applied (see also section 3.1.1.3), resulting in a higher purity of the assembled structures (see figure 4.8B). As an alternative, instead of treating them as waste, the unbound majority type spheres can be included in the subsequent more complex assembly process (see section 4.3).

4.3. Hierarchical self-organization of complex structures

To demonstrate how multi-heterocoagulation can be used in a more complex self-organization process, a five-particle system is deployed. Here, the microspheres are coated with specific DNA strands α, β, Γ, Δ, and ϵ. α-, β-, and ϵ-coated spheres are 1 µm microspheres, Γ-coated spheres have a diameter of 2 µm, and Δ-coated spheres have a diameter of 6 µm. As this approach represents a one-pot approach, all particles are present in the solution throughout the complete process; only the linker strands are added subsequently (see figure 4.9A). In analogy to section 4.2.2, a ternary aggregation process is triggered by adding linker $\overline{\alpha\beta}$ and $\overline{\Gamma\beta}$. Consequently, this results in polar junction-type clusters (settings: $X_{\alpha-\beta} = 25$, $X_{\Gamma-\beta} = 6$). These clusters show high directionality and therefore represent the basis for further assembly steps. In a second step, the α-side of the junctions is connected to a large Δ-sphere by adding linker $\overline{\alpha\Delta}$ ($X_{\Delta-\beta} = 0.22$). A third step is conducted simultaneously by adding linker $\overline{\Gamma\epsilon}$, re-using the Γ-spheres that have acted as majority spheres

in the ternary heterocoagulation process. This leads to binary heterocoagulation of Γ- and ϵ-spheres into binary coagulates that can bind to the Γ-side of the ternary clusters. As this third step of binary attachment is performed in the linear or compact regime, respectively ($X_{\epsilon-\beta} = 10 \ldots 100$), it also enables the control of the size of the finally produced mesoscopic structure (see figure 4.9B, C).

In total, this three-step process leads to the rapid formation of a tadpole-shaped structure on the mesoscale, comprising three different parts. One part is the 6 µm Δ-sphere that represents the head of the tadpole. The second part is a compact polar junction that is build *via* ternary aggregation. Part three is a binary cluster that is independently formed in the linear or compact regime by Γ- and ϵ-spheres, constituting the tadpole's tail. To put it in a nutshell, the five-sphere approach shown here results in an anisotropic and mesoscopic structure of rational design that has been purely formed far from equilibrium while using isotropic building blocks. The effective yield ($= \frac{c_{\text{tadpoles}}}{c_{\Delta\text{-spheres}}}$) of the generated tadpole-shaped structures that reach up to 26 µm in size lies between $\approx$ 50% and 70% (see figure 4.9C, inset).

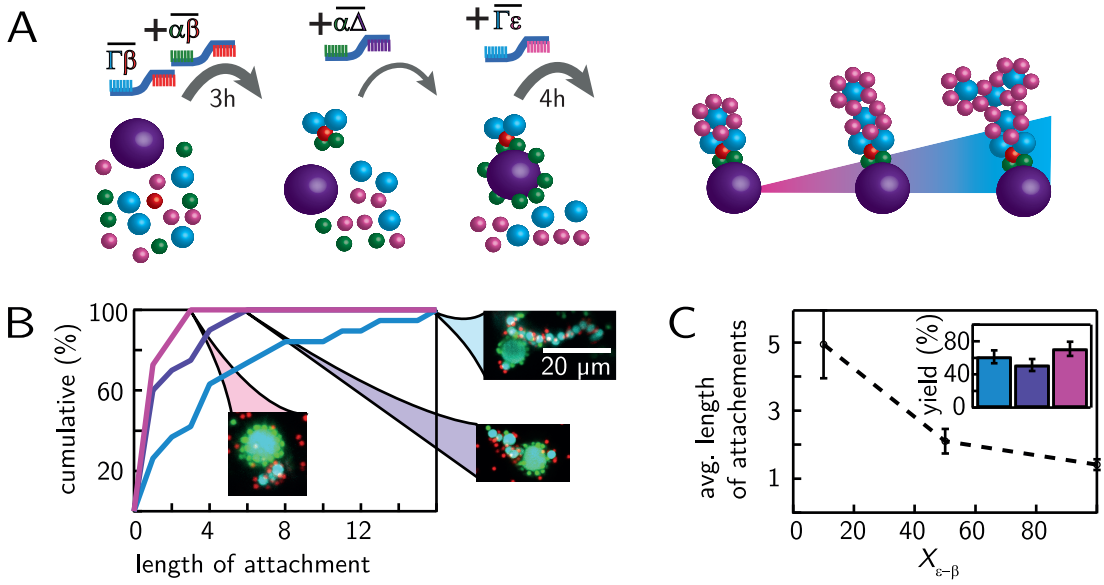

Figure 4.9.: Hierarchical 5-component heterocoagulation process. (*A*) Schematic assembly line, controlled by the addition of DNA-linker strands at different time points. First, ternary aggregation is induced to create polar clusters by adding two distinct linker strands. These junction-type coagulates are connected to a 6 µm base particle on one side and to a binary cluster on the other side. The binary cluster can be controlled in size according to section 4.1. (*B*) Cumulative length distribution of the binary clusters attached to the base particles *via* junctions for different stoichiometries $X_{\epsilon-\beta}$. (Inset) Confocal images show the largest class of binary clusters found in the different samples. (*C*) Average length of the binary clusters attachments as a function of the stoichiometry $X_{\epsilon-\beta}$. (Inset) The effective yield (number of base particles with attachments/number of all base particles) lies between $\approx$ 50% and 70%. Error bars denote SEM of the data.

4.4. Applications

Structure formation of DNA coated colloids far from equilibrium can be utilized to create complex mesoscopic objects. However, for many applications the explicit geometry of the objects plays a minor role. Consequently, in this section, different applications are presented that make use of the scale-free nature of the investigated binary heterocoagulation processes. In order to demonstrate the universality of the approach applications of relevance on different scales, ranging from the nano- to the macroscale are presented.

4.4.1. Light scattering by mesoscopic colloidal structures

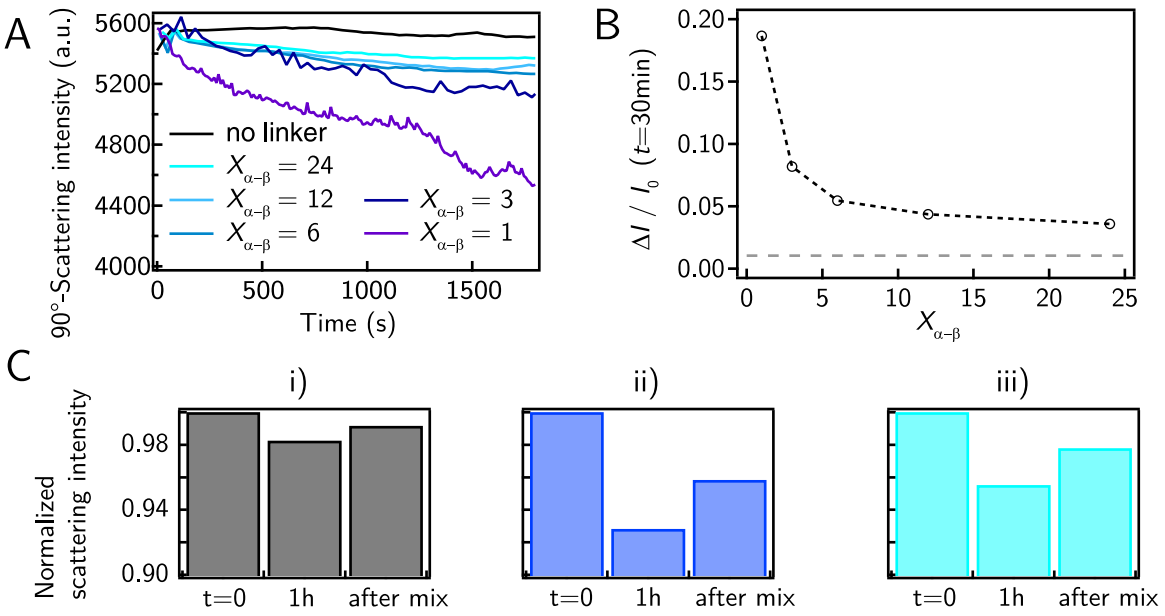

Figure 4.10.: 90°-light scattering on binary microsphere coagulates. (*A*) While The light scattering intensity stays constant for monodisperse microspheres, it significantly drops within 30 min for coagulated spheres. (*B*) The drop of light scattering intensity increases for smaller stiochiometries $X_{\alpha-\beta}$, where larger coagulates are formed (see section 4.1). (*C*) Scattering intensity after the coagulation process and subsequent pipette mixing normalized by the initial intensity. i) monodisperse microspheres, ii) $X_{\alpha-\beta} = 6$, iii) $X_{\alpha-\beta} = 24$.

According to Mie-theory [128] the scattering of light caused by spherical particles is highly dependent on the particle size. Moreover, the particle size does not only strongly influence the scattering intensity, but also the the angular distribution of scattered light in a non-trivial way.

To show, that light scattering is suitable to monitor the colloidal coagulation processes described in this thesis, time course measurements for 90°-light scattering for different binary heterocoagulation processes were conducted. As shown in section 4.1 that large parts of the

coagulation process at the chosen particle concentration are finished within 30 min, light scattering measurements were also performed for this time span (for experimental details see section 3.1.4).
As $X_{\alpha-\beta} = 1$ leads to fast fractal growth and therefore a fast increment of structure size, the light scattering intensity is expected to change rapidly over time. Light scattering measurements could confirm this hypothesis (see figure 4.10A). The scattering intensity drops significantly over time, indicating that the formed clusters exhibit a different scattering behavior. As already known from section 4.1, performing binary heterocoagulation at different stoichiometries $X_{\alpha-\beta}$ leads to the formation of differently sized clusters. Consequently, increasing $X_{\alpha-\beta}$ leads to smaller clusters and thus to a smaller change in scattering intensity over time (see figure 4.10A, B). Obviously, inhibiting coagulation by leaving out the linker strand $\overline{\alpha\beta}$ results in no significant change in scattering intensity over 30 min.
There are different mechanisms that could be the cause for this $X_{\alpha-\beta}$ dependent 90°-light scattering. Firstly, for monodisperse, spherical particles of 1 µm it can be expected, that the incident light ($\lambda_{\text{scatter}} = 497$ nm) is scattered in an approximately isotropic way, leading to a large scattering intensity at 90°. In contrast to that, larger clusters that contain tens to hundreds of particles will not act as point scatterers, but as objects that can be treated in terms of geometrical optics. As a result, these large clusters do rather absorb and reflect light, with small contributions to 90°-light scattering. Secondly, also sedimentation could be the cause for the drop in scattering intensity, as it cannot be totally excluded in this assay despite buoyancy matching using sucrose. Larger clusters sediment faster, thus resulting a more rapid decrease in intensity. In order to investigate the effect of sedimentation, the experiments shown in figure 4.10A have been repeated. After 1 h of coagulation the samples were thoroughly mixed with a pipette and measured subsequently. The data show that mixing does not restore the starting intensity completely. However, $\approx 50\%$ of the scattering intensity can be regained by mixing at $X_{\alpha-\beta} = 6$ and $X_{\alpha-\beta} = 24$ (see figure 4.10C(ii) and C(iii)), indicating that Mie-scattering effects and sedimentation nearly equally contribute to the observed drop in intensity.
Nevertheless, 90°-light scattering could be a valuable tool to characterize and control heterocoagulation processes of µm-sized colloids.

4.4.2. Macroscopic hybrid polymer-DNA coated colloid gels

As described in section 1, colloids of all sizes are widely used to create materials with unique mechanical properties,e.g. they can be used to vary the elastic response of rubbers [129] but are also capable of tailoring the viscosity and the non-linear response of liquids [130].
Here, hybrid polymer-DNA-colloid gels were investigated together with Henry Dehne. These consist of a hydrogel matrix that is formed by PAM (polyacrylamide) of different concen-

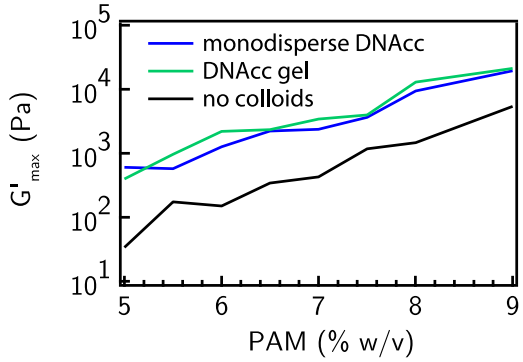

Figure 4.11: Elasticity of hybrid polymer-DNA coated colloid gels. The storage modulus G'_{max}, measured after 20 min of PAM polymerization, increases monotonously with an increase in PAM concentration. While the colloids themselves lead to an increase of nearly one order of magnitude, the explicit structure of the colloids (monodispers/gelated) does not exhibit significant differences.

trations and of the binary DNA coated colloid system ($X_{AB} = 1$) as it has been introduced in section 4.1.1. This hybdrid system offers the opportunity to control colloidal structure formation and hydrogel formation independently and thus to investigate the influence of internal colloidal structure formation on the mechanical properties of gels. To ensure that the hydrogel formation and the colloidal gelation are seperated in time, a light sensitive catalyst for PAM polymerization is used (see section 3.1.3.1 for details). In short, the fractal growth of the DNAcc system at a concentration of $\Phi_{\text{DNAcc}} = 4\%$ is triggered by addition of a linker strand at first. After gelation, the sample is exposed to white light, resulting in PAM polymerization. As a control, the DNAcc system is incubated without the linker strand before illumination, yielding monodisperse colloids dispersed in the PAM matrix.
Measuring the G'_{max} of the samples for different PAM concentrations shows that the addition of the colloids leads to a significant enhancement of the hydrogel elasticity (see figure 4.11). However, the structure of the hydrogel encapsulated colloidal gel does not seem to make a significant difference, as monodisperse and geled DNAcc result in the same G'_{max}. In stark contrast to the elasticity, the toughness of the hydrogel is significantly influenced by the colloidal structure formation within the hydrogel. Recording a strain ramp protocol at $\Phi_{\text{PAM}} = 10\%$ on the monodisperse and the geled system shows that the PAM matrix containing the DNAcc gel is capable of bearing an order of magnitude more stress before rupturing (see figure 4.12A,B). Calculating the amount of energy needed to rupture the hydrogels shows that the hydrogel containing the colloidal gel can absorb $\approx 35\times$ more energy than the monodisperse system. As the composition for both samples is identical, it can be assumed that this vast difference in toughness is solely caused by the changes in colloidal structure. This is especially interesting as only $\Phi_{\text{DNAcc}} = 4\%$ are required to create this tunable hybrid gel.
As the transition from the fluid-like to the gel-like state of presented hybrid gels can be triggered by light exposure, they can also be used in other applications that profit from the explicit macroscopic geometry of the gel in combination with its DNA functionality. In 2D, the hybrid gel can be used as a printable fluid, that is fixated by concentrated ligth exposure

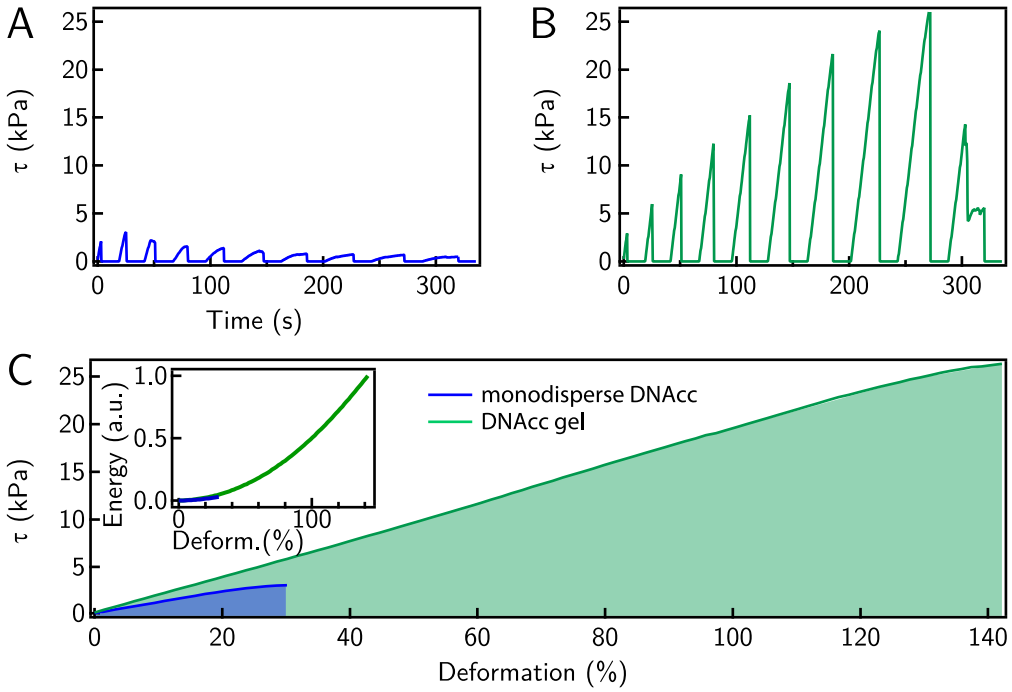

Figure 4.12.: Toughness of hybdrid polymer-DNAcc gels. (*A*) Linear increasing strain ramps show that the hybrid gel containing monodisperse colloids are irreversibly damaged below a stress of 5 kPa.(*B*) In contrast to monodisperse colloids, the gelated DNAcc can bear stresses up to 25 kPa. (*C*) Detailed plot of the last stable stress-strain curve conducted in (*A*) and (*B*). While the inital elasticity is comparable, the hybrid gel containing gelated DNAcc can bear 5× more stress and can absorb up to 35× more energy that the ungelated sample (inset).

at the current position of the printing probe (see figure 4.13A). Moving the printing probe along a substrate creates thin lines of the hybrid gel, containing a significant amount of DNA that is exposed at the surface (see figure 4.13B). This approach therefore results in biochemical functional hydrogel that can be printed in arbitrary 2D shapes. Moreover, using a mold also 3D functional hybrid gels can be produced. Using a cubic mold, PAM blocks can be created. In order to guarantee surface functionalization, a layer of highly concentrated DNAcc is added on top of the yet unpolymerized PAM base (see figure 4.13C). To further increase density and viscosity of the DNAcc solution, 800 mM of sucrose is added. This prevents mixing with the PAM base. The subsequent light exposure leads to full polymerization of the macroscopic gel block that is equipped with a thin functional top layer (see figure 4.13D).

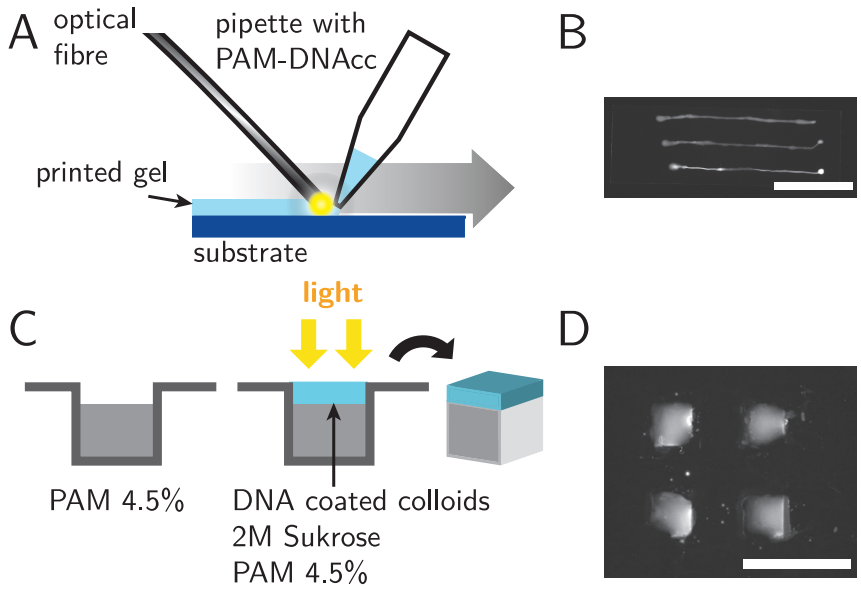

Figure 4.13.: Printing and 3D molding of hybrid polymer-DNA coated colloid gels. (*A*) As the polymerization PAM part of the hybrid gel can be triggered by light illumination, it can be used in ink-jet printing approach. Moving an optical fibre along the ink-jet tip leads to a quasi-instantaneous polymerization of hybrid gel. (*B*) Printed lines of the hybrid-gel, illuminated with UV light. (*C*) Molding of a cubic PAM gel equipped with a top layer of the hybrid gel. After filling the mold with conventional PAM gel, it is covered by an un-polymerized DNA coated colloid hybrid gel with high sucrose content. Due to the high density of the topping solution, the DNAcc stay in the top layer and are fixated by subsequent light exposure. Scale bar 2 cm.

4.4.3. Scaling down to gold nanoparticles for optical applications

It has been shown in section 4.1.4 that the underlying mechanism for the binary structure formation processes as presented here is scale-free and therefore independent of particle size. According to equation 4.8, the only deterministic parameter is the stoichiometry $X_{\alpha\beta}$, which governs the growth limitation of the fractals. However, the timescale of coagulation process can be altered by the concentration of the particles (see equation 4.4).

Exploiting this model, the binary heterocoagulation of 10 nm sized spherical gold nanoparticles (AuNP) has been investigated together with Benedikt Buchmann [131]. In contrast to the microspheres, the nanoparticles have been coated with complementary ssDNA, so that the addition of a linker strand is not required. This is a precaution to ensure that also at this small scale the coagulation process is limited by particle diffusion alone and not by particle-DNA reaction rates. Following the model, different stoichiometries $X_{\alpha-\beta}$ should lead to differently sized clusters.

Indeed, mixing the nanoparticles at different stoichiometries $X_{\alpha-\beta}$ results in solutions that

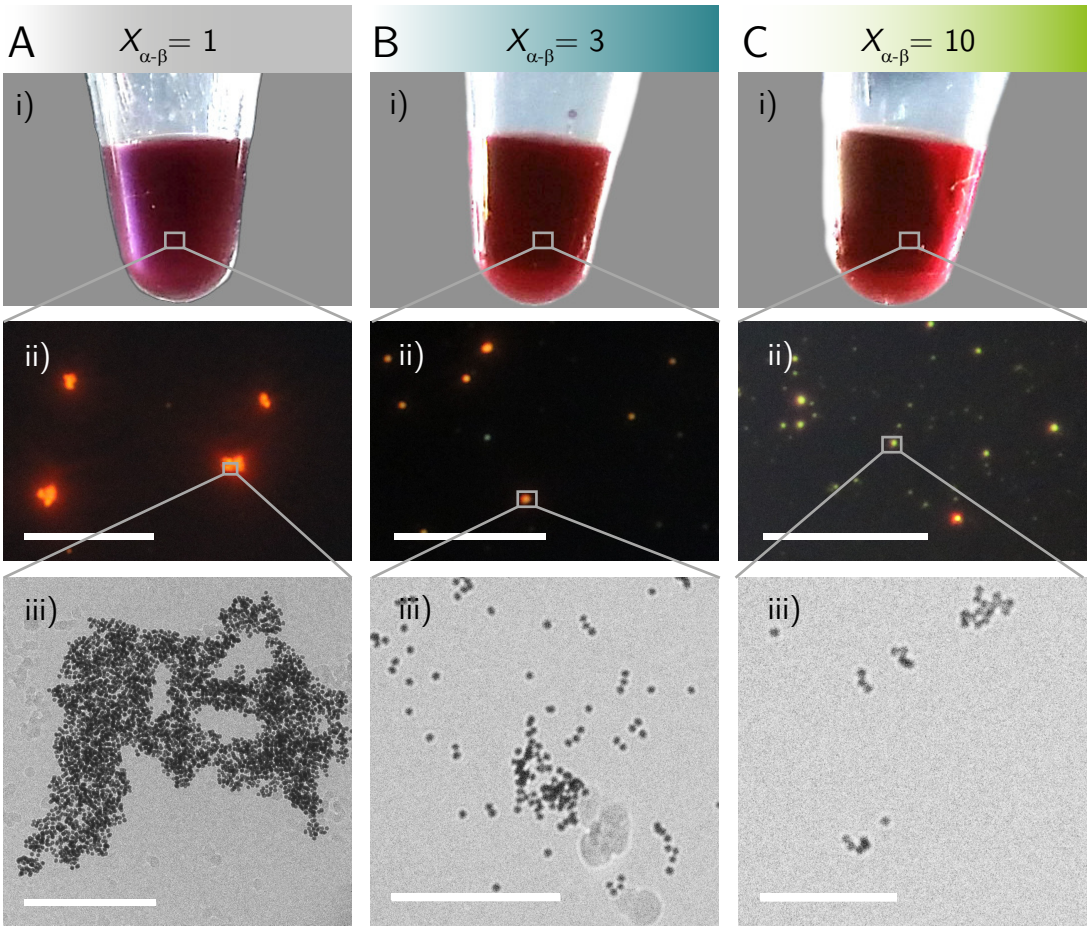

Figure 4.14.: Binary heterocoagulation of 10 nm sized gold nanoparticles on different scales for different stoichiometries $X_{\alpha-\beta}$. (*A*) At $X_{\alpha-\beta} = 1$, large nanoparticle cluster form. This can be seen from the macroscale (photo, i), down to the mesoscale (dark field imaging, ii, scale bar 20 µm) and the nanoscale (TEM, iii, scale bar 200 nm). (*B*) $X_{\alpha-\beta} = 3$ leads to smaller clusters that change the behavior on all scales. (*C*) At $X_{\alpha-\beta} = 10$ the clusters contain only a few particles, leading to a visible green shift in dark field imaging (ii).

can be distinguished on the macroscopic scale by naked eye due to their difference in light extinction (see figure 4.14A(i), B(i), C(i)). In order to verify that this originates from differently sized clusters, dark field imaging was applied (see section 3.1.2.5 for details). This already shows on the microscale that higher $X_{\alpha-\beta}$ lead to objects decreasing in size with a spectral change from red to green (see figure 4.14A(ii), B(ii), C(ii)). Resolving these objects with transition electron microscopy (TEM) reveals that these objects indeed represent nanoparticle clusters of different sizes (see figure 4.14A(iii), B(iii), C(iii)). It is obvious from figure 4.14 that AuNP clusters of different sizes result in significantly different optical properties of the particle solution. This behavior can be understood with reference to Mie-theory [128]. Accordingly, AuNPs interact with the incoming light resulting in absorption and scattering. Surface plasmonic resonance (SPR) is responsible for light absorption of

particles of radius R with $R \ll \lambda$. Monodisperse AuNP therefore absorb light at 520 nm. Increasing the clustersize shifts the resonance frequency to higher wavelengths. Additionally, larger clusters also exhibit enhanced light scattering, which results in increased light extinction, enabling dark field microscopy to image clusters that are below the diffraction limit. Indeed, UV/VIS measurements show that the extinction spectrum can be controlled by adjusting $X_{\alpha-\beta}$ (see figure 4.15A). This leads to a controlled shift of the extinction maximum depending on $X_{\alpha-\beta}$ (see figure 4.15B).

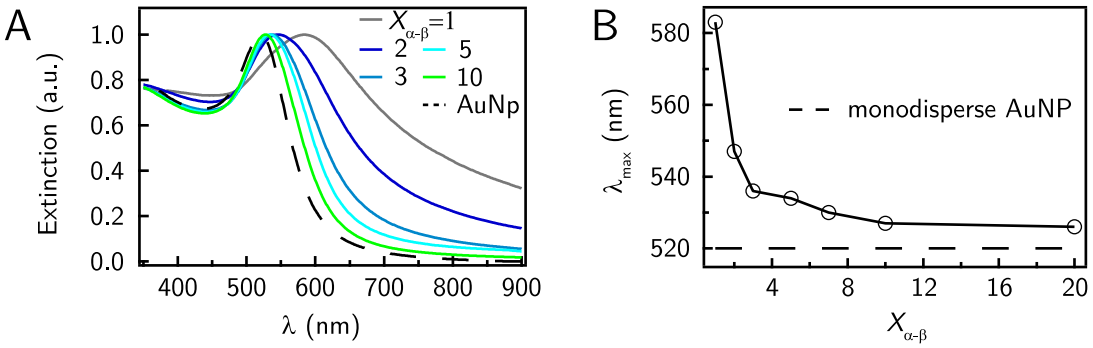

Figure 4.15.: Extinction spectra of nanoparticle clusters for different stoichiometries $X_{\alpha-\beta}$. (A) The normalized extinction spectra show a monotonous of the peak position and the spectal width. (B) The peak position from (A) depending on $X_{\alpha-\beta}$. As higher $X_{\alpha-\beta}$ lead to smaller clusters, the curve asymptotically approaches the monodisperse particle limit for high $X_{\alpha-\beta}$.

4.5. Discussion and Outlook

Multicomponent self-organization is becoming of increasing interest for the field of complex self-organization [132]. However, the formation of multicomponent structures is mainly investigated on the nanoscale. This is done by using short pieces of ssDNA as building blocks in equilibrium approaches [133][134]. In this chapter it was shown that also multicomponent systems that interact far from equilibrium can be utilized to create complex structures by rational design. DNA coated colloids with a diameter between 1–6 µm served hereby as a simplified model system. Although the colloids represent microspheres that exhibit no intrinsic directionality in geometry or functionality, they can be utilized to create finite sized, asymmetric structures.

Firstly, it has been shown that in binary systems kinetic arrest can be used to create finite-sized structures that can be considered mesoscopic. The size and geometry of these structures can be adjusted by controlling the binary stoichiometry of the two microsphere species. It was found that structure size and geometry are correlated so that the differently sized structures can be categorized into three geometrical classes: The smallest clusters

contain only one minority sphere and several majority spheres. They represent nearly round, densely packed objects and are therefore termed compact clusters. If the clusters are allowed to grow larger than compact, they expand *via* fractal growth. However, if this fractal growth is limited to only small clusters of up to ≈ 10 minority particles, clusters predominantly do not exhibit branches. They are therefore termed linear clusters. Only if the clusters are allowed to grow larger than ≈ 10 minority particles, the structures exhibit the typical branched fractal architecture, reaching the classical DLCA limit in fractal dimension analysis. The binary coagulation process was successfully rationalized by an analytic model based on Smochulowski's concept of fast coagulation, allowing deeper insight into the timescales and the mechanisms of the structure formation process. Expanding this idea to a system of ternary heterocoagulation in the compact regime lead to the formation of asymmetric structures that exhibited polar functionality. These polar objects could subsequently be utilized in a true colloidal multicomponent system of 5 different microsphere species to assembly complex mesoscopic objects in a hierarchic fashion. Note, that in comparison to equilibrium-based self-organization techniques, which rely on the predefinition of the desired structures by precise control of the equilibrium positions, the presented approach is based on the kinetic control of the diffusion dynamics of a colloidal system by means such as particle sizes and stoichiometries. The approach presented herein can therefore directly be extended to any multicomponent system that allows for multiple orthogonal interactions.
However, the complexity of the assembled structures is limited by the prediction capabilities of kinetic model. While for binary heterocoagulation an analytical model is sufficient, multicomponent structures can only be predicted by numerical methods. To extend the capabilities of the presented approach, numerical simulations have to be performed that accurately reproduce the experimental findings. In collaboration with Timo Krüger [135] it could already be shown that binary systems can be reproduced with sufficient precision (see figure 4.16). Expanding this approach to multicomponent systems could yield a toolbox for multicomponent self-organization systems.
Moreover, as the presented approach is scale-free, it has a high potential of facilitating novel materials with applications that require tailored plasmonic excitation bands, scattering, biochemical, or mechanical behavior. Consequently, different applications were investigated on a proof-of-principle basis. Using 10 nm gold particles, it could be shown that binary heterocoagulation far from equilibrium can also be applied on the nanoscale to control the size of colloidal structures. As gold nanoparticles exhibit strong surface plasmonic resonance, assembling differently sized colloidal structure resulted in a direct control over the optical extinction spectra of the samples. To show that the colloidal structures can also be used to create novel materials in terms of mechanical properties, a PAM-DNAcc hybrid gel was rheologically investigated. The measurements showed that a gel of DNAcc was able to

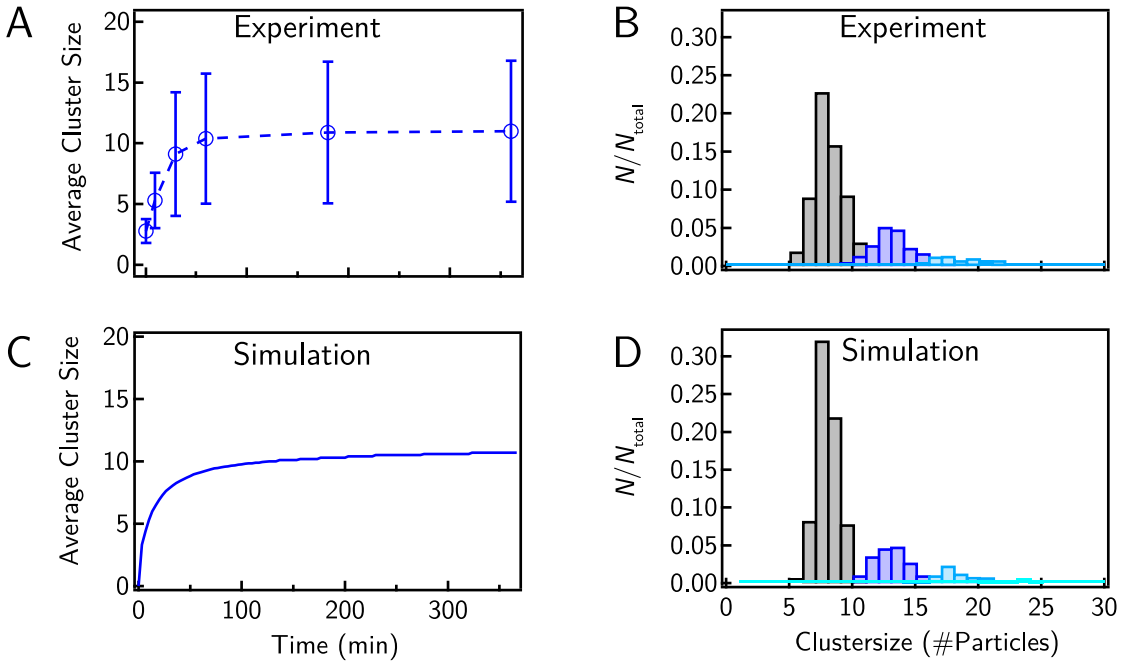

Figure 4.16.: Comparison of experimental and simulation data for binary heterocoagulation at $X_{\alpha-\beta} = 18$. (A) Experimental data from 4.5 showing the time evolution of the average cluster size. (B) Experimental data from figure 4.2 showing the cluster size distribution after 6h. (C) and (D) simulation for $X_{\alpha-\beta} = 12$ (A). Simulation data from [135].

absorb $\approx 35\times$ more energy before rupturing in comparison to monodisperse colloids. This is especially interesting, as the difference in the mechanical properties arises solely from the difference in local arrangement of the colloids while the composition of the samples was identical. As the fluid-gel transition of this PAM-DNAcc hybrid gel is designed to be triggered by light, also 2D gel-printing and 3D gel blocks are possible application that have been described in this chapter.

The whole of these applications further strengthens the idea that the presented self-organization techniques could give rise to a field of future applications spanning from smart materials to optoelectronics to quantumcomputation [50][136][137].

5. Dynamic Structure Formation by DNA Coated Colloids

In the first part of this thesis it was shown that fast coagulation processes of colloids can be stirred and controlled to create complex mesoscopic structures by rational design. Moreover it has been shown, that these structures exist far from equilibrium, which enables the fastest possible self-organization process that is only limited by diffusion and not reaction times. In this chapter, a dynamic component is added to the previously static system to enable timely control over structure formation of DNA coated colloids. As it is known from synthetic biochemical reaction networks, enzymatic reactions are coupled to the colloidal system to achieve dynamic control. T7 RNA Polymerase will be used to produce RNA linker strands that are designed to link two species of DNA coated colloids and therefore lead to fractal growth. As structure formation is directly coupled to enzymatic activity, regulating the enzymatic rates also changes the rate of structure formation. To disintegrate the colloidal structures the enzyme RNAseH is deployed. As RNaseH only degrades ssRNA strands that are bound to ssDNA in a RNA-DNA duplex, RNAseH is capable of removing the RNA linker strands from the DNA coated colloids, therefore effectively disintegrating the colloidal structures. To show the potential of this approach, a RNA pulse caused by the two enzymes is coupled to the colloidal system, which results in tunable transient structure formation of the DNA coated colloids.

5.1. RNA polymerization and degradation for colloidal aggregation

5.1.1. Controlling RNA polymerization by T7 polymerase

5.1.1.1. Controlling the rate of RNA polymerization

Experimental means of controlling the rate of product formation by T7 polymerase are of vital importance for the presented system. Consequently, fluorescence time course measurements as described in section 3.2.3 have been conducted for different conditions at a fixed concentration of polymerase $c_{T7,ref}$.

As described in section 2.3.3, T7 polymerase requires double stranded DNA as templates for

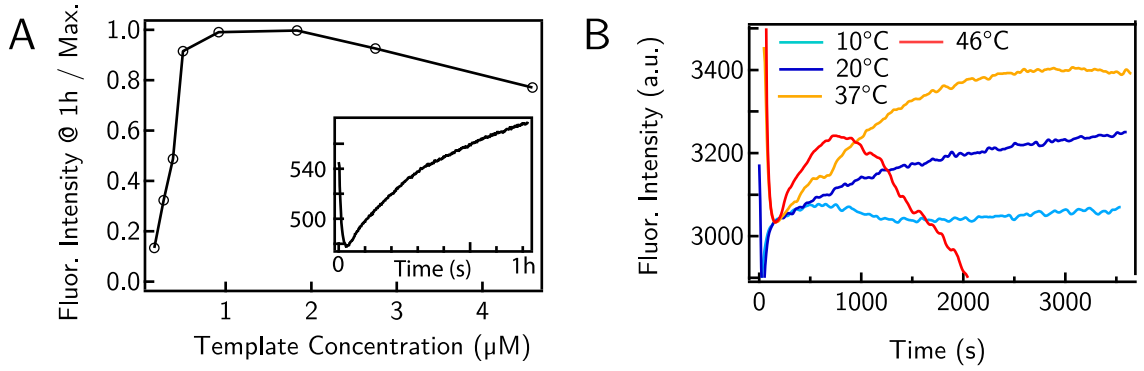

Figure 5.1.: Fluorescence bulk measurements of RNA polymerization by T7 RNA polymerase. (*A*) Increasing the template concentration increases the amount of produced RNA within 1h, yielding an effective control over RNA polymerization. At a template concentration of $c_{\text{ideal}} = 0.91$ μM, a maximum in RNA production is reached, indicating that T7 polymerase is saturated with templates. (Inset) typical polymerization curve at c_{ideal}. (*B*) Temperature dependence of T7 RNA polymerase. The production rate of RNA is increased monotonously between 10°C and 37°C. At higher temperatures the produced RNA is degraded in an auto-catalytic process.

transcription. If the concentration of active enzymes and templates ($= c_{\text{ideal}}$) are comparable, the enzymes are able to work at their full catalytic rates, yielding the fastest production of RNA strands at a fixed NTP concentration. However, if the concentration of templates is reduced significantly below c_{ideal}, unbound enzymes will remain in the sample, thus being inactive. This is expected to reduce the overall rate of RNA production, yielding a valuable tool for the control of RNA production rates. On the other hand, increasing the template concentration above c_{ideal} should have little effect on the rate of production, as the enzymes are saturated with templates.

Indeed, the data shows that the RNA production can be well controlled by varying the template concentration between 0.17–0.91 μM, resulting in a relative change from 10 to 100% of the RNA fluorescence signal after 1 h (see figure 5.1A). Above 0.91 μM the production of RNA stagnates, followed by a slightly template concentration depended decrease of RNA polymerization. This shows that c_{ideal} lies at 0.91 μM, indicating that this is the effective concentration of enzymes at the chosen amount of T7 polymerase stock solution in the sample (see figure 5.1A, inset). This effective concentration of enzymes will be used in section 5.1.1.2 to deduce quantitative production rates. This slightly template concentration dependent decrease of RNA polymerization is probably an artifact caused by the fluorescent dye that also binds to the dsDNA templates under lower quantum yield of fluorescent light emission.

As the enzymatic reactions have to be conducted under buffer conditions that are also appropriate for the colloidal system, it is necessary to find the optimal buffer conditions in

regard to both systems. As described in section 3.1.1.2, the colloidal system is prepared with 450 mM of sucrose to prevent fast sedimentation and 10 mg/ml BSA for means of passivation. Fluorescence measurements for different sucrose and BSA concentrations show, that there is a dependence of T7 polymerase activity on both reactants. Enzyme activity reaches its maximum at 5 mg/ml BSA (see figure A.1B). Adding 450 mM sucrose does not have a significant effect on enzyme activity.
Another important tool to control the rate of RNA polymerization externally is the temperature dependency of the enzymes. It is know that enzyme activity and temperature are highly correlated, allowing for precise control of production rates [138]. However, the temperature dependence of T7 RNA polymerase is also dependent on the transcription sequence and the buffer conditions [139]. Consequently, the temperature dependence of RNA production was investigated for the standard colloidal buffer conditions (450 mM sucrose, 5 mg/ml BSA) (see figure 5.1B). While increasing the temperature from 37°C to 46°C did not affect the speed of polymerization, it lead to a fast decrease of fluorescence signal after roughly 10 min of polymerization, probably caused by an increased auto-hydrolysis of RNA at higher temperatures. In contrast to that, a decrease to 20°C lead to a significant reduction in RNA polymerization by $\approx$ 50%. Finally, at 10°C, no enzymatic activity and therefore no RNA polymerization could be measured.
Overall, the rate of RNA polymerization can be effectively controlled either intrinsically by adjusting the template concentration or externally by changing the temperature. The buffer conditions required for colloidal aggregation do not have a negative effect on RNA polymerization by T7 polymerase.

5.1.1.2. Quantity and specificity of RNA polymerization

To address the question of quantity and specificity of RNA polymerization, quantitative measurements of enzymatic reaction rates have to be conducted. Knowing these reaction rates, predictions can be made that allow to couple the enzymatic system efficiently to the colloidal system.
As discussed in section 2.3.3, assuming that the enzymes are saturated with templates, the initial rate of production $\frac{dc_{\mathrm{RNA}}}{dt}(t=0)$ follows the Michaelis-Menten model (see equation 2.8)

$$\frac{dc_{\mathrm{RNA}}}{dt}(t=0) = k_{\mathrm{cat}} c_{\mathrm{T7}} \frac{c_{\mathrm{NTP},0}}{K_M + c_{\mathrm{NTP},0}} \quad , \tag{5.1}$$

where $c_{\mathrm{NTP},0}$ is the concentration of NTPs at $t = 0$. According to section 5.1.1.1 this requirement is fulfilled for the template concentration c_{ideal} at the reference concentration of T7 polymerase $c_{\mathrm{T7,ref}}$ defined in section 3.2.2. Subsequent measurements have therefore been conducted at $c_{\mathrm{T7}} = c_{\mathrm{T7,ref}} = c_{\mathrm{ideal}}$. Indeed, fluorescence measurements at varying NTP

concentrations show the expected dependency (see figure 5.2B). $\frac{dc_{RNA}}{dt}(t=0)$ was extracted by a linear fit to the first 500 s to each polymerization curve and has been converted to RNA concentrations according to section 3.2.3. Fitting equation 2.8 to the data, while making use of c_{ideal} as the concentration of enzymes, yields enzymatic reaction rates for T7 polymerase at the buffer conditions established in section 5.1.1.1. These enzymatic rates ($k_{cat} = 0.00635$ 1/s, $K_M = 0.91$ mM) are comparable to what is expected from literature (see section 2.3.3). However, for $K_M \gg c_{NTP,colloid}$ equation 5.1 can be simplified to

$$\frac{dc_{RNA}}{dt} = k_{cat} c_{T7} \frac{c_{NTP}}{K_M + c_{NTP}} = \frac{k_{cat} c_{T7,ref} X_{T7}}{K_M} c_{NTP} = k_{eff,T7} X_{T7} c_{NTP} \quad , \tag{5.2}$$

where $X_{T7} = \frac{c_{T7}}{c_{T7,ref}}$ is the dimensionless normalized concentration of T7 polymerase and $k_{eff,T7} = 6.35 \cdot 10^{-6}\ \frac{1}{s}$. As only comparably low NTP concentration have to be used for

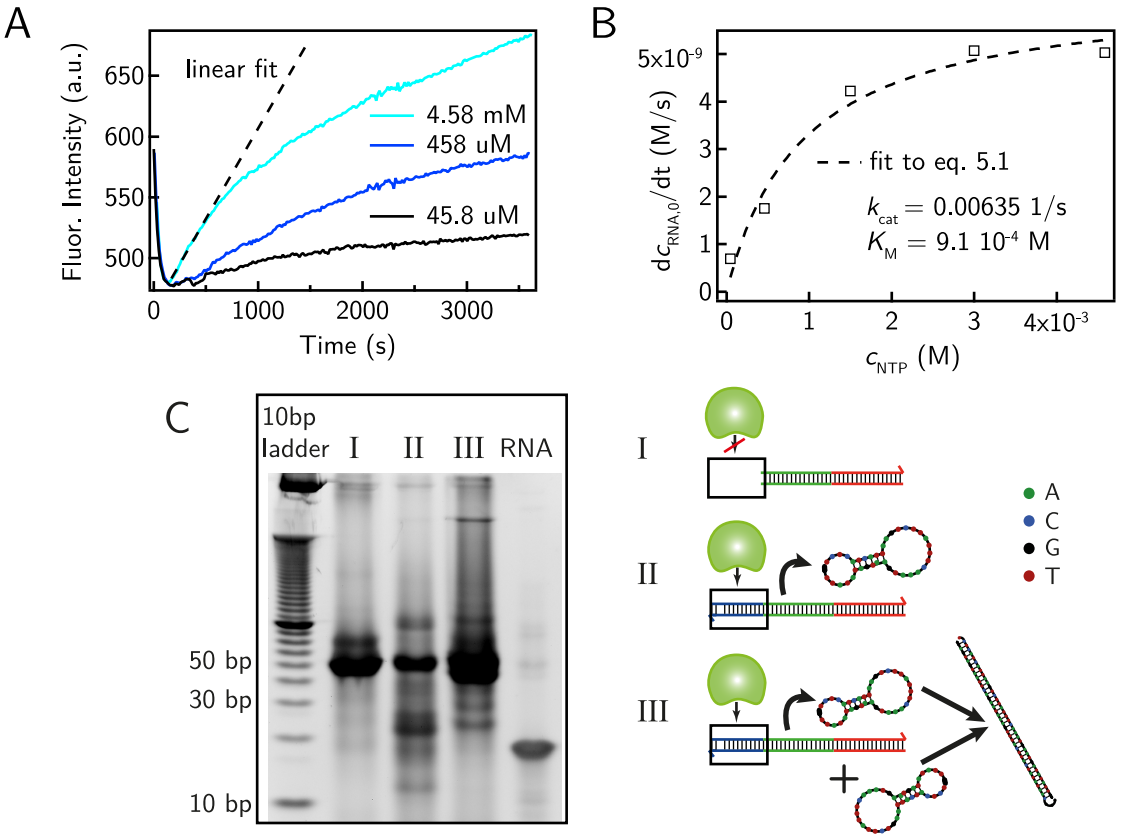

Figure 5.2.: Quantity and specificity of RNA production by T7 RNA polymerase. (*A*) Polymerization curves for different NTP concentrations. The linear fit for $t = [0 \ldots 500]$s was used to measure the inital rate of RNA production. (*B*) Initial rate of RNA production calibrated according to section 3.2.3. Fitting equation 5.1 yields quantitative rates for RNA production. (*C*) Specificity of the produced RNA. (I) A template without the recognition sequence does not lead to production of RNA. (II) RNA production of the complete template strand containing the recognition sequence. (III) Polymerization and subsequent hybridization of RNA to its DNA complement.

colloidal aggregation (< 10 µM), validity of equation 5.2 can be assumed for quantitative predictions.

For the chosen target RNA sequence to be polymerized, the base Adenin is limiting the maximum amount of target RNA to be produced, as it has the highest frequency in the sequence ($N_{Ad} = 17$). It therefore limits the maximum concentration of target RNA in the sample after complete polymerization to $c_{RNA,max} = \frac{c_{ATP}}{17}$. However, the data shows that $c_{NTP} = c_{GTP} = c_{UTP} = c_{CTP} = c_{ATP} = 45.8$ µM is sufficient to polymerize $c_{RNA} = 6.8$ µM (see figure 5.2A,B), which lies well above the aggregation threshold $c_{RNA,colloids} = 46$ nM, but also above $c_{RNA,max}$. This indicates that T7 polymerase keeps polymerizing also after Adenin is depleted in the sample, producing shorter RNA fragments. This hypothesis could be validated by native polyacrylamide gelelectrophoresis (PAGE) (see figure 5.2C). While templates without a promoter sequence do not lead to RNA polymerization within 1 h (see figure 5.2C(I)), samples containing templates with a complete promoter sequence show a significant production of RNA strands by T7 polymerase (see figure 5.2C(II)) that are also able to hybridize to complementary DNA strands (see figure 5.2C(III)). Additionally, it is evident that not only target RNA strands but also shorter fragments are produced that can also hybridize to target complementary DNA strands (see figure 5.2C(III)). Also, the total length of the produced RNA is a few nucleotides longer than the control RNA. This results from the details of RNA polymerization by T7 polymerase that also includes some promoter sequence nucleotides during the transcription process (see section 2.3.3).

As a conclusion, the data shows that the chosen settings are capable of producing a sufficient amount of target RNA well within appropriate timescales for colloidal aggregation. The specificity of the RNA products for the chosen template sequence is very high initially, but drops significantly after the consumption of the limiting base Adenin. leading to the production of shorter RNA fragments.

5.1.2. RNA degradation by RNASeH

Another critical step for a dynamic colloidal structure formation process it the controlled degradation of the RNA linkers that link the colloids to form the desired structures. RNaseH only degrades RNA linkers that are bound to DNA strands in a RNA-DNA duplex. This ensures that degradation only takes place at the binding sites and that the DNA docking strands on the colloidal surfaces stay intact. Indeed it can be shown with fluorescence measurements, that RNAseH does not affect single stranded RNA or DNA but does completely remove 1 µM of RNA within a RNA-DNA duplex at the buffer conditions established in section 5.1.1.1 (see figure 5.3A). Also native PAGE experiments could confirm that the degradation of 1 µM of RNA by RNAseH is very effective, so that the RNA is nearly completely degraded after 10 min and no significant amount of smaller RNA fragments are

found (see figure 5.3B).
According to equation 2.8 the enzymatic rate of production of NMPs by degradation of RNA can be described as

$$\frac{dc_{\mathrm{NMP}}}{dt} = k_{\mathrm{cat}} c_{\mathrm{RNAseH}} \frac{c_{\mathrm{RNA}}}{K_M + c_{\mathrm{RNA}}} \quad . \tag{5.3}$$

Due to mass conservation it is also known that

$$c_{\mathrm{NMP}}(t) = L \cdot (c_{\mathrm{RNA},0} - c_{\mathrm{RNA}}(t)) \quad , \tag{5.4}$$

where L is the number of nucleotides in one RNA strand and $c_{\mathrm{RNA},0}$ is the initial concentration of RNA at $t = 0$. As the typical K_M of ribonucleases ($\approx 10^{-2}$ M [140]) is much greater than the RNA concentrations that will be degraded here (≈ 1 µM), the initial rate of RNA degradation can be written as

$$\frac{dc_{\mathrm{RNA}}}{dt}(t=0) = -\frac{k_{\mathrm{cat}} c_{\mathrm{RNAseH}}}{L \cdot K_M} c_{\mathrm{RNA},0} = -\frac{k_{\mathrm{cat}} c_{\mathrm{RNAseH,ref}} X_{\mathrm{RNAseH}}}{L \cdot K_M} c_{\mathrm{RNA},0} \tag{5.5}$$

where $X_{\mathrm{RNAseH}} = \frac{c_{\mathrm{RNAseH}}}{c_{\mathrm{RNAseH,ref}}}$ is the normalized dimensionless concentration of RNAseH on the reference concentration of RNAseH as defined in section 3.2.3. As neither the concentration of enzyme nor the enzymatic rates in equation 5.7 are known, it is impossible to determine k_{cat} and K_M independently. It is therefore reasonable to define effective rates that can be used to quantitatively predict degradation in relative parameters. By varying the normalized concentration of RNAseH X_{RNAseH} at a fixed concentration of $c_{\text{RNA-DNA}} = 5$ µM in fluorescence measurements, the expected linear relationship of initial production rates could be obtained (see figure 5.3C). Thus, the shown linear relationship can be fitted by the equation

$$\frac{dc_{\mathrm{RNA}}}{dt}(t=0) = -k_{\mathrm{eff,RNAseH}} \cdot c_{\mathrm{RNA},0} \cdot X_{\mathrm{RNAseH}} \quad , \tag{5.6}$$

with $k_{\mathrm{eff,RNAseH}} = 7.41 \cdot 10^{-4}\ \frac{1}{\mathrm{s}}$ as a result. A typical timescale for RNA degradation can therefore be written as

$$t_{\mathrm{degrad.}} = \frac{1}{k_{\mathrm{eff,RNAseH}} \cdot X_{\mathrm{RNAseH}}} \quad . \tag{5.7}$$

Temperature dependent measurements of RNA degradation show, that in contrast to T7 RNA polymerase, RNAseH exhibits a complete reduction of activity already at 20°C (see figure 5.3D), while being promoted at temperatures above 37°C. This promotion of activity at higher temperatures is probably due to RNA auto-hydrolysis that has been already observed in section 5.1.1.1.
As a conclusion, degradation of RNA by RNAseH can be controlled at appropriate timescales compared RNA polymerization and colloidal aggregation and is therefore potentially suitable

for colloidal disintegration. Interestingly, the temperature dependence of RNAseH and T7 polymerase differ significantly, which opens new opportunities for temperature controlled applications.

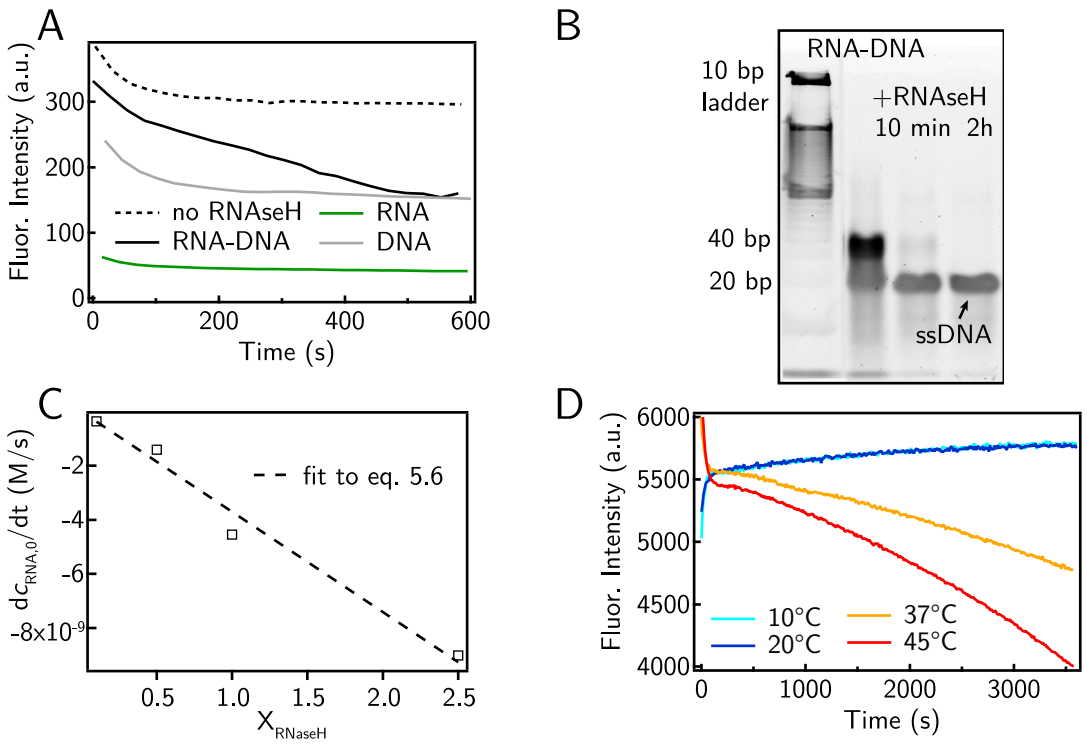

Figure 5.3.: RNA degradation by RNAseH. (*A*) Degradation of RNA only occurs in RNA-DNA duplexes. While pure DNA or RNA is not affected by RNAseH, the RNA bound in an RNA-DNA duplex is degraded. (*B*) Native PAGE showing the effectivity of RNA degradation described in (*A*). (*C*) Initial rate of RNA degradation for different normalized RNAseH concentrations. The fit to equation 5.7 yields quantitative rates for RNA degradation under the presented conditions. (*D*) Temperature dependence of RNA degradation by RNAseH. In contrast to T7 RNA polymerase there is no significant activity up to 20°C.

5.1.3. Competition of polymerization and degradation yields a tunable RNA Pulse

In order to achieve a transient structure formation of colloidal structures the previously shown polymerization and degradation of RNA linker strands have to be coupled. Applying a theoretical minimal model to these coupled enzymatic processes is needed to predict and control the subsequent experiments concerning colloidal structure formation.

The coupling can be modeled combining the already established equations 5.6, 5.2 and 5.13 to

$$\frac{dc_{\mathrm{RNA}}}{dt} = k_{\mathrm{eff,T7}} X_{\mathrm{T7}} \cdot c_{\mathrm{NTP}} - k_{\mathrm{eff,RNAseH}} \cdot X_{\mathrm{RNAseH}} \cdot c_{\mathrm{RNA}} \tag{5.8}$$

$$\frac{dc_{\mathrm{NTP}}}{dt} = -k_{\mathrm{eff,T7}} X_{\mathrm{T7}} N_{\mathrm{Ad}} \cdot c_{\mathrm{NTP}} \quad . \tag{5.9}$$

Solving these differential equations for a limited NTP pool of $c_{\mathrm{NTP,0}}$ yields

$$c_{\mathrm{RNA}}(t) = \Gamma \cdot \left(e^{-k_{\mathrm{eff,T7}} X_{\mathrm{T7}} N_{\mathrm{ad}} t} - e^{-k_{\mathrm{eff,RNAseH}} X_{\mathrm{RNAseH}} t} \right) \quad , \tag{5.10}$$

where $\Gamma = \frac{c_{\mathrm{NTP,0}} k_{\mathrm{eff,T7}} X_{\mathrm{T7}}}{k_{\mathrm{eff,RNAseH}} X_{\mathrm{RNAseH}} - k_{\mathrm{eff,T7}} X_{\mathrm{T7}} N_{\mathrm{ad}}}$. Equation 5.10 represents a relaxational pulse, while the NTPs are depleted exponentially (see figure 5.4A). In order to compare this result to experimental data in a reasonable way, first equation 5.10 has to be interpreted in respect to dynamic colloidal self-organization. As the goal of this chapter is to create a transient structure formation of colloids, two independent features of the RNA pulse are of high interest: The height of the pulse and the peak position of the pulse. These two features also determine when the threshold for aggregation and disintegration of the colloidal structures are reached, thus yielding timescales for the colloidal transient self-organization process. The height of the pulse can directly be seen from equation 5.10 and is given by Γ. It is obvious that the pulse height is linearly proportional to the initial concentration of NTPs, $c_{\mathrm{NTP,0}}$. In comparison to equation 5.14 not only the concentration of NTPs but also the rates of the enzymes as well as their concentrations strongly influence the pulse height. Consequently it is apparent from Γ, that in order to vary the peak position independently of the pulse height the only remaining free parameters X_{RNAseH} and X_{T7} have to be varied. However, while varying either X_{T7} or X_{RNAseH} results in a change in position and height (see figure 5.4B), keeping $\frac{X_{\mathrm{T7}}}{X_{\mathrm{RNAseH}}} = const.$ leads to the desired effect. To capture the peak position quantitatively, 5.8 can be evaluated for $\frac{dc_{\mathrm{RNA}}}{dt} = 0$, yielding the peak position at

$$t_{\mathrm{peak}} = \frac{\ln\left(\frac{k_{\mathrm{eff,T7}} X_{\mathrm{T7}} N_{\mathrm{ad}}}{k_{\mathrm{eff,RNAseH}} X_{\mathrm{RNAseH}}}\right)}{k_{\mathrm{eff,T7}} X_{\mathrm{T7}} N_{\mathrm{ad}} - k_{\mathrm{eff,RNAseH}} X_{\mathrm{RNAseH}}} = \frac{1}{\kappa} \cdot \frac{\ln\left(\frac{k_{\mathrm{eff,T7}} N_{\mathrm{ad}}}{k_{\mathrm{eff,RNAseH}}}\right)}{k_{\mathrm{eff,T7}} N_{\mathrm{ad}} - k_{\mathrm{eff,RNAseH}}} \quad , \tag{5.11}$$

where $\kappa = X_{\mathrm{T7}} = X_{\mathrm{RNAseH}}$. As the catalytic rates of the enzymes are given intrinsically by the enzymes and the buffer conditions, respectively, only by varying the concentration of RNAseH and T7 polymerase by the same factor κ leads to an experimentally well-controlled shift of the peak position. Moreover, as the peak position is inversely proportional to κ, is is expected that higher enzyme concentrations lead to a faster pulse of the same height. Indeed, fluorescence experiments for different κ reproduce this behavior (see figure 5.4C). Using the the catalytic rates of the enzymes that have been determined in sections 5.1.1.2

and 5.1.2 also allow for theoretically modeling the experimental data, yielding a quantitative picture in terms of RNA concentration (see figure 5.4D). It can be clearly seen, that the simplified assumptions that lead to this model are justified and can be used to make quantitative predictions for the presented experimental setup. According to the shown model curves, the experimental settings shown here lead to pulses with peak RNA concentration of $c_{\mathrm{RNA,\,peak}} \approx 10$ µM at peak-times between $t_{\mathrm{peak}} \approx 30$ min and $t_{\mathrm{peak}} \approx 3.5$ h. These timescales and RNA concentrations are well suited for the following approach to create a transient structure formation of colloids.

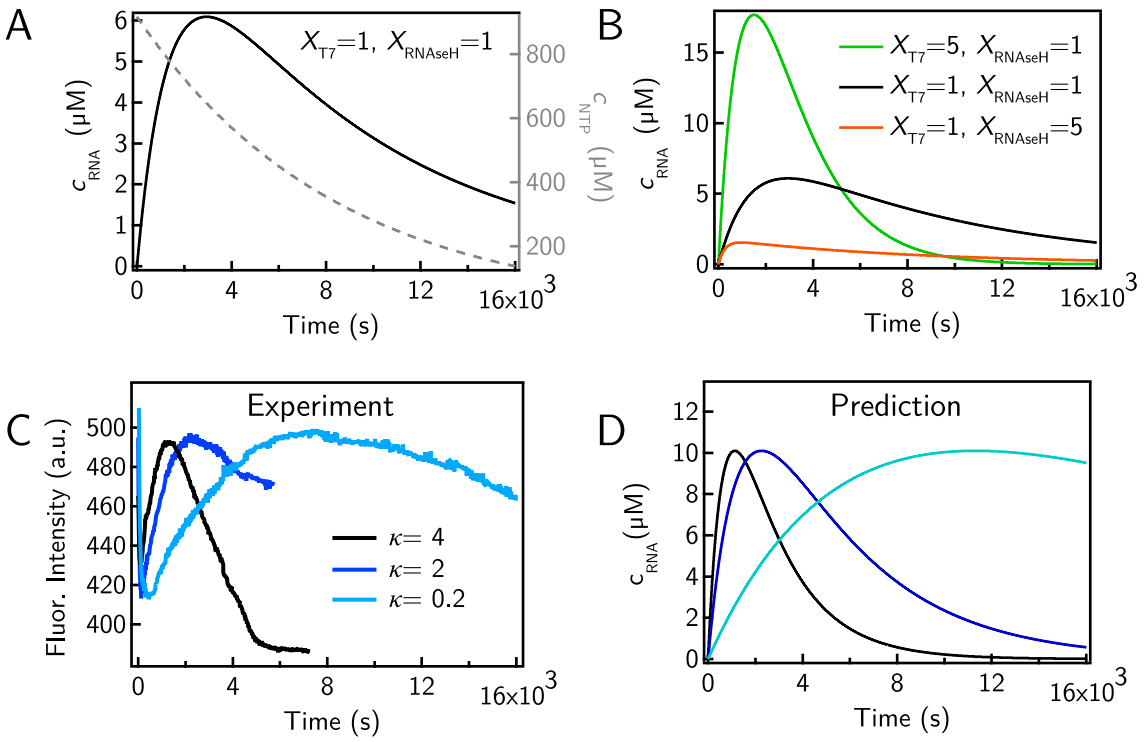

Figure 5.4.: RNA pulse generation by T7 RNA polymerase and RNAseH. (*A*) Model predictions deduced from sections 5.1.1.2 and 5.1.2 for $X_{\mathrm{T7}} = X_{\mathrm{RNAseH}} = 1$ showing an RNA pulse and the corresponding depletion of NTPs. (*B*) RNA pulses for different T7 and RNAseH concentrations. (*C*) Fluorescence experiments for different $\kappa = X_{\mathrm{T7}} = X_{\mathrm{RNAseH}}$, showing that κ yields full control over the peak position of the RNA pulse. (*D*) Model predictions for the experimental data in (*C*).

5.2. Coupling the RNA signal to structure formation

5.2.1. Colloidal structure formation by RNA polymerization

In order to couple the presented enzymatic processes to the colloidal system in a controlled way colloidal coagulation has to be characterized in regard to the buffer conditions and the

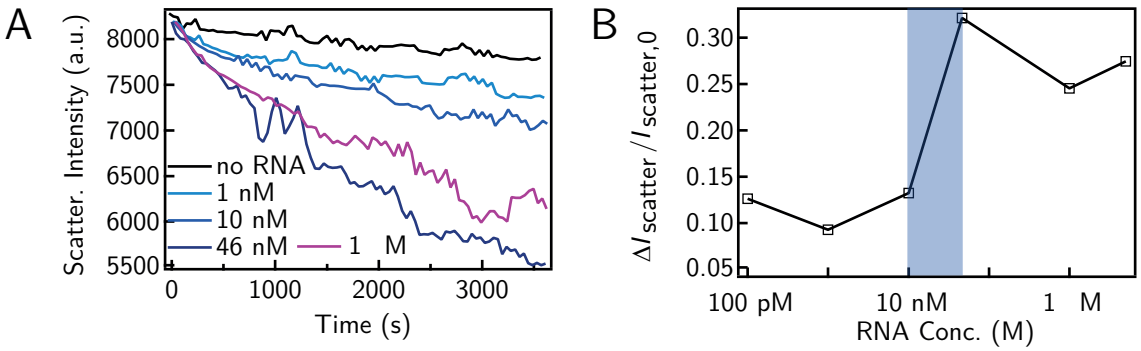

Figure 5.5.: Coagulation of DNA coated colloids induced by RNA. (*A*) 90°-light scattering measurements of the coagulation process for different RNA concentrations. (*B*) Analysis of the coagulation speeds in (*A*) shows that the DNAcc exhibit fast coagulation at an RNA concentration of $c_{RNA,colloids} > 46$ nM.

produced RNA. Light scattering measurements show, that binary heteroaggregation can be induced by adding commercially synthesized ssRNA linker in analogy to chapter 4 (see figure 5.5A). Upon addition of the RNA linker, the scattering signal drops significantly, showing fast heterocoagulation within minutes. This confirms that also RNA can be used in the enzymatic buffer conditions to ensure efficient colloidal aggregation. Plotting the percentile drop of scattering intensity after 1h shows that increasing the RNA concentration does not result in a continuous increase in aggregation speed, but rather corresponds to a switch-like behavior (see figure 5.5B). Below the concentration of 10 nM RNA, the colloids show only weak aggregation of small clusters. In contrast to that the colloids aggregate rapidly above $c_{RNA,colloids} = 46$ nM. $c_{RNA,colloids}$ can therefore be considered as the fast coagulation threshold for the buffer conditions of chapter. Consequently, it is reasonable to limit the NTP pool for colloidal experiments to a comparable concentration. Choosing $c_{RNA,max} = 500$ nM as a limit for RNA production will ensure not only that enough RNA is produced to induce structure formation, but also that the structural disintegration by RNA degradation can be achieved at reasonable timescales. This requires an NTP pool of

$$c_{NTP,colloids} = 500 \text{ nM} \cdot 17 = 8.5 \ \mu M \quad . \tag{5.12}$$

To estimate the timescale at which the threshold for colloidal aggregation is reached, model predictions from equation 5.2 can be conducted. Equation 5.2 is coupled to the consumption of NTPs by

$$\frac{dc_{NTP}}{dt} = -k_{eff,T7} X_{T7} N_{Ad} \cdot c_{NTP} \quad . \tag{5.13}$$

The solution of both differential equations under the boundary condition for a finite NTP pool $c_{NTP,0}$ reads

$$c_{RNA}(t) = \frac{c_{NTP,0}}{N_{Ad}} \left(1 - e^{-k_{eff,T7} X_{T7} \cdot N_{Ad} \cdot t}\right) \quad . \tag{5.14}$$

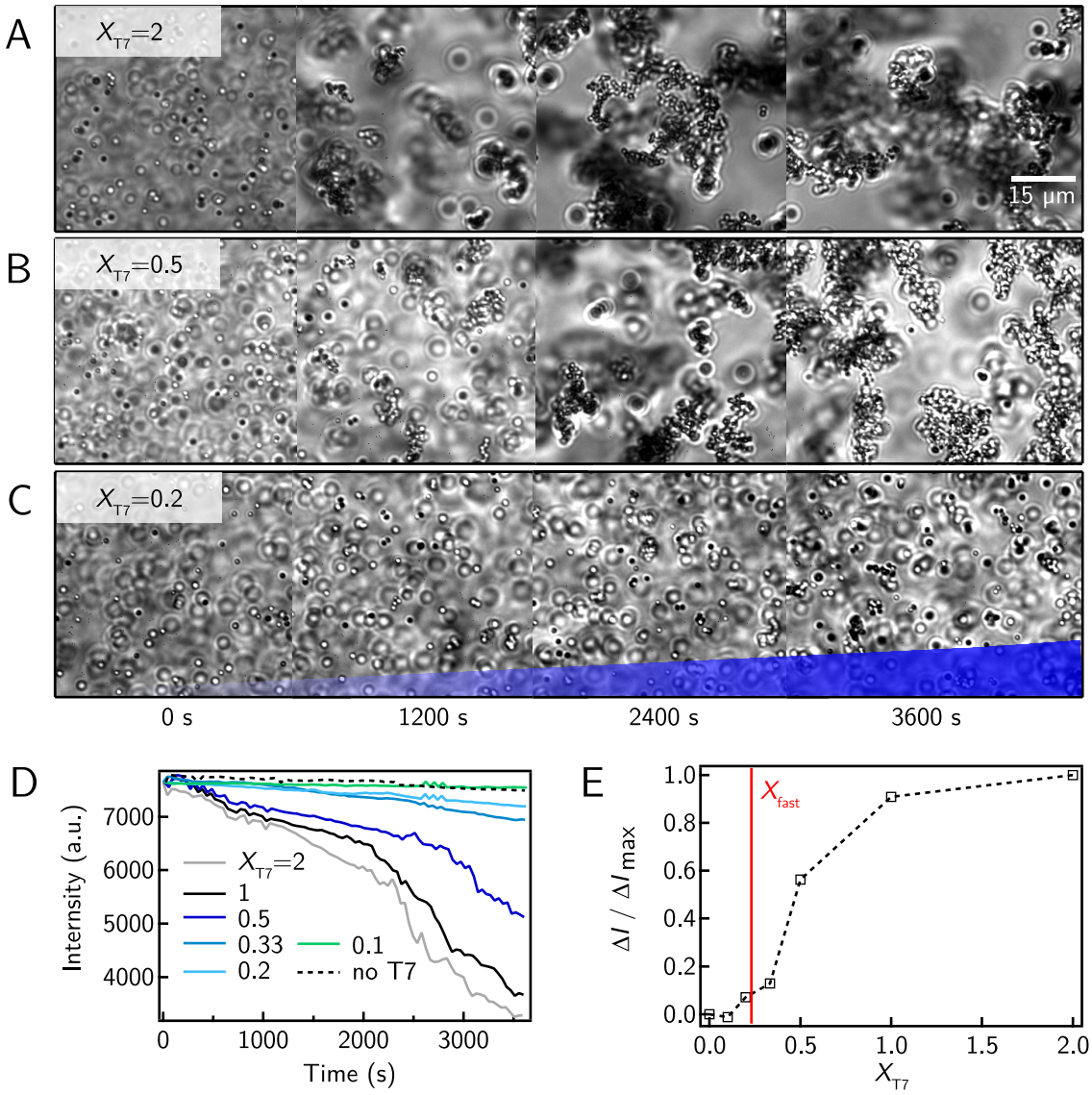

Figure 5.6.: Time course measurements of DNA coated colloid coagulation caused by RNA production of T7 RNA polymerase. (*A*) to (*C*) Microscopy images showing that a decreasing concentration of T7 polymerase results in slower colloidal coagulation. (*D*) 90°-light scattering measurements quantitatively show the influence of T7 polymerase concentration on the coagulation speed of the DNAcc. (*E*) Normalized drop in scattering intensity ΔI for different T7 polymerase concentrations X_{T7}. The predicted X_{fast} for the onset of fast coagulation is in good agreement with the experimental data.

A characteristic time $t_{aggr.}$ for the polymerization of $c_{RNA,target}$ that is able to cause fast aggregation can be written as

$$t_{aggr.} = t(c_{RNA,target}) = -\left(\frac{1}{k_{eff,T7} X_{T7}}\right) \cdot \ln\left(1 - \frac{c_{RNA,target} N_{Ad}}{c_{NTP,0}}\right) \quad . \tag{5.15}$$

As a result, $t_{aggr.} = 813$ s for $c_{NTP,colloids}$, $c_{RNA,target} = c_{RNA,colloids}$ and $X_{T7} = 1$ can be obtained. This timescale is comparable to typical aggregation times at this colloid concentration and could therefore influence the time dependent behavior of colloidal aggregation. Thus it can be expected that by reducing the concentration of the T7 polymerase-template complex also the speed of colloidal aggregation can be slowed down and hence effectively controlled.

Indeed, time-lapse microscopy images at $c_{NTP,colloids}$ show that aggregation can be successfully triggered and varied by RNA polymerization (see figure 5.6). While there is no obvious difference between $X_{T7} = 2$ and $X_{T7} = 0.5$, $X_{T7} = 0.2$ shows a drastic decrease in colloidal aggregation over 1h. This is in line with what can be expected from equation 5.15. For the above described concentrations, $t_{aggr.} > 1$h is reached for $X_{T7} < 0.23 (= X_{fast})$, i.e. the onset of fast aggregation will not be observed within 1 h, leading to drastically suppressed cluster growth and no gelation. However, it seems that the produced RNA is sufficient to build smaller clusters.

To confirm quantitatively that this effect is caused by a decrease in $t_{aggr.}$, light scattering measurements for different X_{T7} were conducted (see figure 5.6D, E). It is evident that the prediction of $X_{fast} = 0.23$ is in good agreement with the experiments.

This shows that colloidal aggregation of DNAcc can be caused by specific RNA polymerization of T7 RNA polymerase. Furthermore, the time-dependent aggregation behavior of DNAcc can be quantitatively understood by taking into account models of enzymatic activity and known coagulation rates.

5.2.2. Colloidal structure disintegration by RNA degradation

In analogy to the previous section, the effect of enzymatic activity of RNAseH on the colloidal system was investigated. To see whether RNAseH is capable of disintegrating colloidal structures that are linked by a RNA-DNA complex, the DNAcc were pre-incubated with linker RNA to build large colloidal structures and subsequently subjected to different normalized concentrations X_{RNaseH} of RNAseH. At this stage, synthesized and purified linker RNA close to the colloidal fast aggregation threshold ($c_{RNA,colloids} = 46$ nM) was used instead of enzymatically polymerized RNA to guarantee optimal conditions for structural disintegration. To exclude pipetting artifacts upon RNAseH addition, RNAseH was added at the beginning of the experiment. As RNAseH activity is highly suppressed below 10°C (see section 5.1.2), incubation of the samples for 30 min on ice allowed the colloidal coagulates to form, while the enzyme remained mostly inactive. Subsequently, the samples were put on the microscopy temperature stage at 37°C, recreating working conditions for the enzyme and thus activating it. Time course microscopy images show that RNAseH is indeed capable of disintegrating preformed colloidal structures by degrading RNA bound in RNA-DNA linker

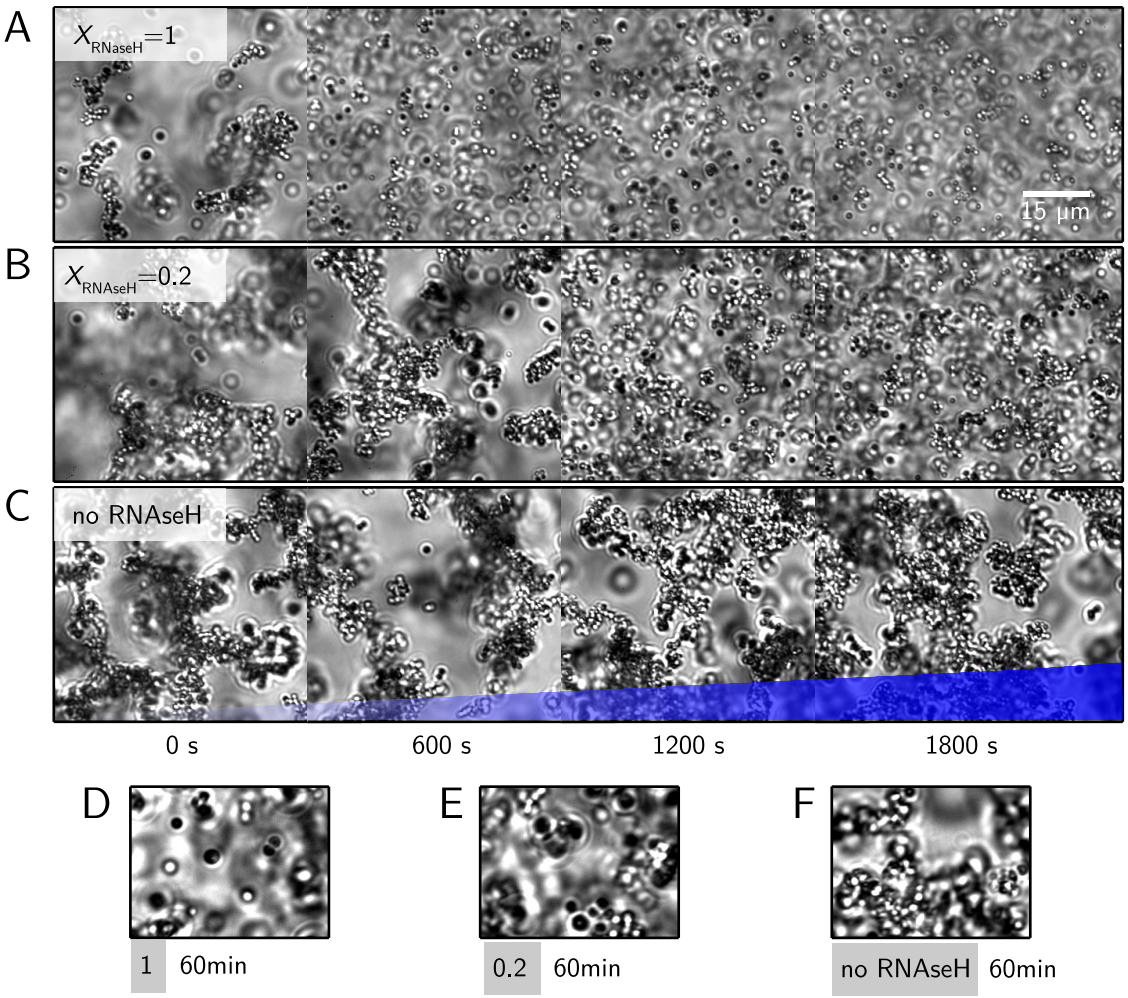

Figure 5.7.: Disintegration of pre-formed DNAcc clusters linked by RNA-DNA duplexes. (A) –(C) Decreasing the concentration of RNAseH increases the time scale of cluster disintegration. The time scale for the disintegration process lies between 1–20min. (D) – (F) Close-up images for the samples in (A) –(C) after 60min.

complexes (see figure 5.7,A-C). While $X_{\text{RNaseH}} = 1$ leads to a fast disintegration of the DNAcc structure after a few minutes, $X_{\text{RNaseH}} = 0.2$ already prolongs the disintegration process to $\approx$ 20 min. As expected, a sample without RNAseH stays stable during the same time span. These timescales are significantly longer than expected from non-colloidal experiments of section 5.1.2, where $t_{\text{degrad.}}(X_{\text{RNaseH}} = 1) = 22.5$ min. RNAseH seems to be significantly more effective in the colloidal system leading to RNA degradtion that is $\approx 10\times$ faster. It has to be noted that the disintegration process does in general not generate a monodisperse system of single particles. Close-up images of different X_{RNaseH} after 1h show, that the disintegration process is very effective at $X_{\text{RNaseH}} = 1$, leaving only a few small clusters and many single particles behind (see figure 5.7,D). Already at $X_{\text{RNaseH}} = 0.2$, even though the very large clusters are disrupted, the remaining clusters still harbor tens to

hundreds of particles (see figure 5.7,E).
Nevertheless, these experiments show that RNAseH is able to effectively degrade RNA linkers bound in between DNAcc, leading to a disintegration of colloidal structures. This second step of dynamic colloidal structure formation completes the basic set of tools needed for a transient self-organization of DNAcc.

5.3. Transient colloidal structure formation

As it has been shown in sections 5.2.1 and 5.2.2 the enzymes T7 RNA polymerase and RNAseH are capable of producing and degrading RNA strands at the requirement amount at reasonable timescales to steer colloidal structure formation of DNAcc. In analogy to section 5.1.3 the combination of polymerization and degradation should lead to a transient self-organization of DNAcc, so that mesoscopic colloidal structures autonomously form and disintegrate without human intervention.
Indeed, microscopy measurements show that such a mesoscopic transient structure formation can be achieved and controlled with the presented system. At $c_{\mathrm{NTP},0} = c_{\mathrm{NTP,colloids}}$, $X_{\mathrm{T7}} = 2$ and $X_{\mathrm{RNaseH}} = 0.2$ colloidal structures are monotonously built in the first $t_{\mathrm{turn}} = 20$ min and quickly disintegrated subsequently (see figure 5.8C). The time scale of this transient structure formation can be well controlled by adjusting X_{RNaseH}. As expected, while increasing X_{RNaseH} leads to a shorter t_{turn} or no structure formation at all (see figure 5.8A,B), lowering X_{RNaseH} leads to an increment of t_{turn} (see figure 5.8D). Image analysis further solidifies this conclusion (see figure 5.8E,F) showing that t_{turn} can effectively be shifted, reaching larger clusters at later points in time. Moreover it shows that the fluorescence measurements of section 5.1.3 can not be directly transferred to the colloidal system. This can readily seen by calculating the fluorescence peak time t_{peak} from equation 5.11 for $X_{\mathrm{T7}} = 2$ and $X_{\mathrm{RNaseH}} = 0.2$

$$t_{\mathrm{peak}}(X_{\mathrm{T7}} = 2, X_{\mathrm{RNaseH}} = 0.2) = 5284s \quad . \tag{5.16}$$

This lies well beyond the observed $t_{\mathrm{turn}} = 1200$ s. However, as it has been shown in section 5.2.2, the degradation of RNA is effectively enhanced in colloidal disintegration experiments. Taking this enhancement into account t_{peak} can be estimated as $t_{\mathrm{peak}}(X_{\mathrm{T7}} = 2, X_{\mathrm{RNaseH}} = 2) = 1471$ s. This value is comparable to t_{turn}, thus yielding a possible explanation for the deviation of fluorescence and colloidal experiments. Nevertheless, the enzymes T7 polymerase and RNAseH are indeed capable of producing and degrading RNA linker strands in the desired fashion, yielding a toolbox for dynamically assembly and disassembly of DNA coated colloidal structures at reasonable time scales.

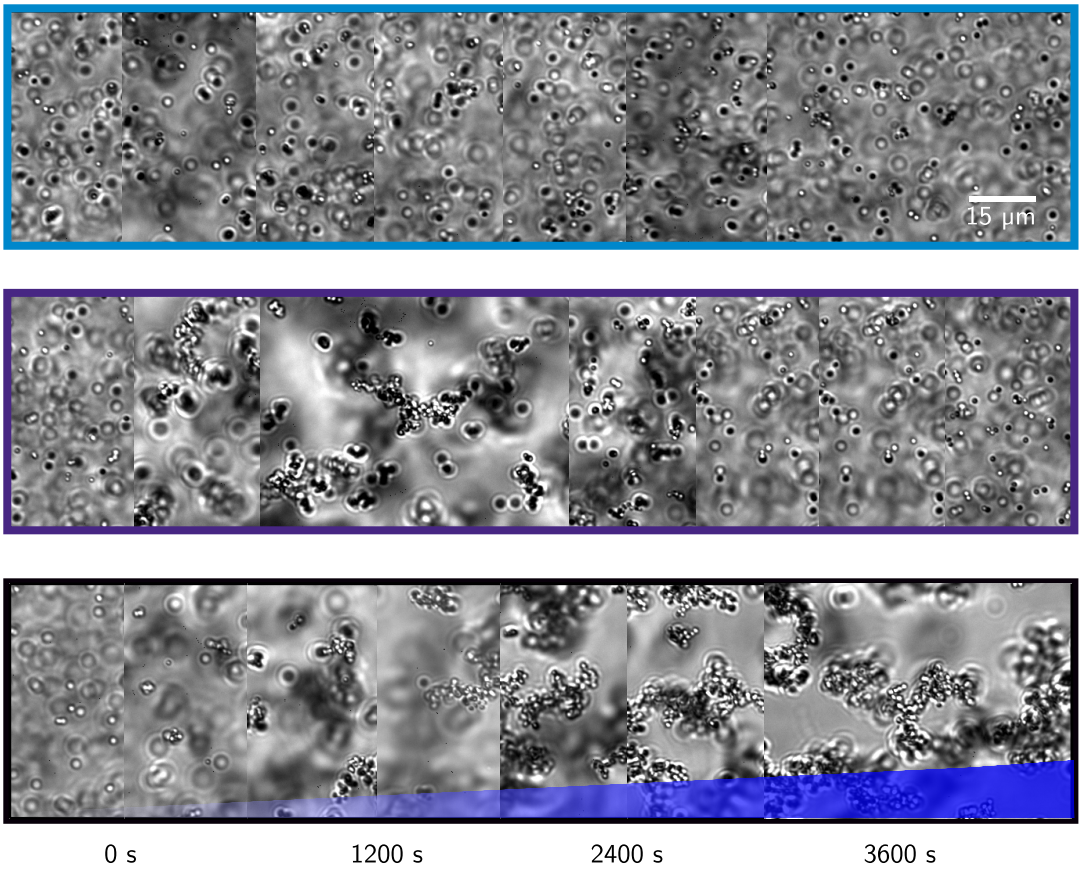

Figure 5.8.: Transient structure formation of DNA coated colloids by T7 RNA polymerase and RNAseH. Varying the concentration of RNAseH X_{RNaseH} shifts the transient time scale. (A) $X_{\mathrm{RNaseH}} = 0.5$ does not show significant cluster formation. (B) $X_{\mathrm{RNaseH}} = 0.33$ enables the formation of small clusters that are disintegrated within minutes after they are formed. (C) Consequently, $X_{\mathrm{RNaseH}} = 0.2$ leads to the formation of large clusters that are slowly disintegrated over $\approx$ 30min. (D) $X_{\mathrm{RNaseH}} = 0.16$ results in the formation of a gel-like structure that is not fully disintegrated over a time scale of 1h. (E) Image analysis of the the microscopy images shown in (A)–(D). Decreasing the concentration of RNAseH leads to the formation of larger structures that are disintegrated in a relaxation-like process. The control experiment without RNAseH can be clearly separated from the transient self-assembly processes. (F) Close-up of (E), focused on the transient self-organization phase.

5.4. Discussion and Outlook

In this chapter it was shown that the static structure formation processes of chapter 4 can be rendered dynamic by deploying the enzymes T7 RNA polymerase and RNAseH. T7 polymerase is capable of producing the required quantities of RNA at a sufficient specificity in applicable time scales. Although the enzyme activity is highly dependent on buffer conditions, temperature and template concentration, there exists a range of stable experimental conditions that are suitable for both enzymatic and colloidal reactions. Accordingly, using 450mM sucrose for colloidal buoyancy matching and 5 mg/ml BSA for colloidal passivation did not have a negative effect on enzymatic activity. Consequently, quantitative parameters for the enzymatic production of RNA by T7 polymerase and the RNA degradation rates of RNAseH could be obtained. Interestingly, the temperature dependence of these rates where significantly different. Combining these parameters with the quantitative rates of RNAseH lead to a simplified model of an transient RNA pulse. This model was capable of predicting experimental data with sufficient accuracy, yielding valuable analytic parameters to predict time scales of the assembly-disassembly cycle.
Using this knowledge, the enzymatic production and degradation of RNA was applied to the DNA coated colloid system of polystyrene micro spheres as it was introduced in chapter 4. It could be shown that the polymerization of RNA lead to binary heterocoagulation of the DNAccs. By adjusting the rate of polymerization, additional control over the speed of colloidal coagulation was demonstrated, showing that the DNAcc did not interfere with the RNA production. Also the disintegration of the colloidal structures by RNAseH could be demonstrated. This proves that the colloids were indeed specifically linked by RNA-DNA duplexes. However, it was also evident, that the colloidal disintegration process was nearly an order of magnitude faster than expected from bulk experiments. This hints to the fact that the localization of the RNAseH substrates on the colloids significantly influences the activity of the enzyme. Nevertheless, combining coagulation and disintegration yielded a transient self-organization of colloidal clusters. This dynamic self-organization process represents a type of self-organization that is currently only known on the molecular scale [92]. Potentially, it therefore opens a new route towards colloidal self-organization processes based on enzymatic reactions that have been applied to create logical or oscillating operations [78][68][79]. Additionally, the observed dependency of enzymatic activity concerning substrate localization on the colloids may be used to introduce a self-reinforcement in RNA production/degradation into the system. As this is the basic mechanism for pattern formation in reaction-diffusion systems, the presented system could ultimately be used to study 3D pattern formation processes by DNAcc. Moreover, the deviation in temperature dependence of RNAseH and T7 polymerase activity could be utilized for create switchable materials. While at low temperatures ($10 - 20°C$), only the polymerase is active, RNAseH

activity is boosted at 37°C. As a consequence, a sample containing both enzymes can be used to triggered colloidal coagulation at 10°C and switched to a system of monodisperse colloids at an arbitrary point in time, by activating the RNAseH at 37°C (see figure 5.9). Assuming a sufficiently large pool of NTPs this could lead to a system, where the fractal growth of DNAcc is rendered switchable, broading the spectrum of applications presented and discussed in section 4.4.

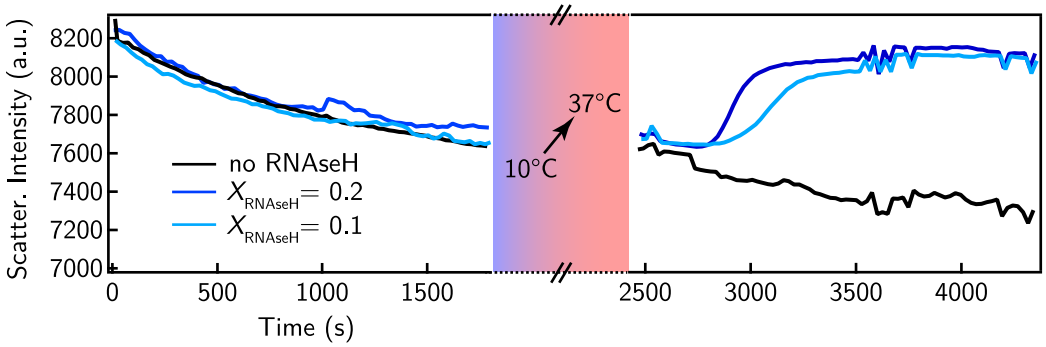

Figure 5.9.: Temperature switchable structure formation by DNA coated colloids for different RNAseH concentrations monitored by 90°-light scattering. After inducing the coagulation process by RNA, samples are incubated at 10°C, leading to fast coagulation. After 30min, the temperature is increased to 37°C, leading to RNAseH activity and a subsequent structure disintegration.

A. Appendix

A.1. Polymerization of RNA by T7 RNA polymerase

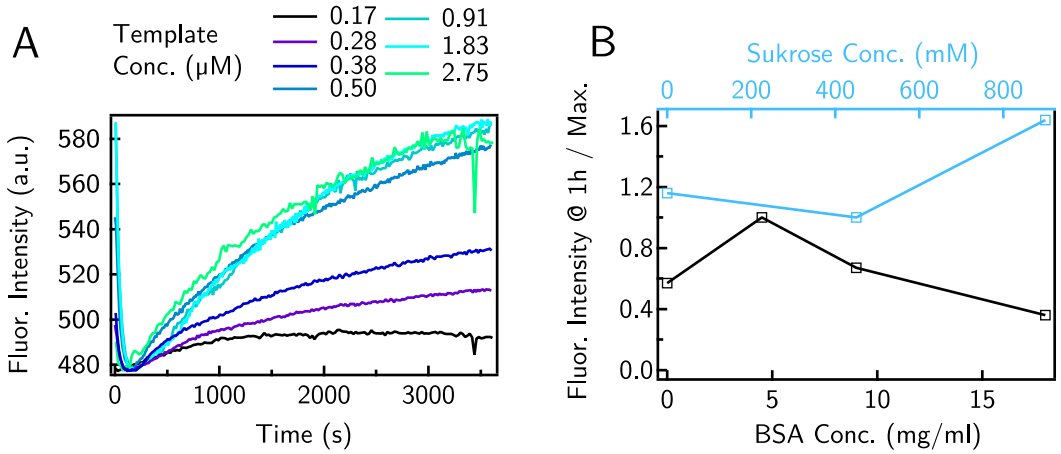

Figure A.1.: Polymerization of RNA by T7 RNA polymerase. (*A*) Detailed time course measurements for different template concentrations. (*B*) Increase of fluorescence intensity after 1h for different sucrose and BSA concentrations at the template concentration c_{ideal}.

A.2. Clustering algorithm

Listing A.1: IGOR PRO clustering algorithm, main

```
1  // greenParticles has to be a wave with dimension "j x 4", where j is the number
       of particles and the 4 columns are for: x-,y-z-coordinates of the particles
       and for the clusterID
2  //FH: Waves must be imported as: xdataG_org etc and xdataR_org, bdgreen und
       bdgreenred in um!
3  //TooManyParticles = 1 => Only Particles in 100um*100um are considered; helps
       when IGOR crashes
4  //DONT forget to type in StackDimensions in wave stackdimensions!

6  ////////////////////////////////////
7  //BEGIN MAIN///////////////
8  ////////////////////////////////////
9  function Measure(bdgreen, bdgreenred, xScale, yScale, zScale,TooManyParticles)
```

```
11  variable xScale,yScale,zScale,TooManyParticles
12  variable bdgreen, bdgreenred
13  wave xDataG_org, yDataG_org, zDataG_org,xDatar_org, yDatar_org, zDatar_org


16  wave stackdimensions

18  //Create working waves
19  duplicate/O xdataG_org xdataG
20  duplicate/O ydataG_org ydataG
21  duplicate/O zdataG_org zdataG
22  duplicate/O xdataR_org xdataR
23  duplicate/O ydataR_org ydataR
24  duplicate/O zdataR_org zdataR

26  //Working waves scaled in um
27  xdataG *= xScale
28  ydataG *= yScale
29  xdataR *= xScale
30  ydataR *= yScale
31  zdataG *= zScale
32  zdataR *= zScale

34  if (TooManyParticles == 0)
35  //FH 19.09.14
36  //Delete Border Line Particles in xy (every particle closer than 5 um to the
        boundary will be deleted!)
37  xDataG = xDataG < 5 ?  Nan : xDataG
38  xDataG = xDataG > (Stackdimensions[0]-5) ?  Nan : xDataG

40  yDataG = numtype(xDataG) == 2 ? NaN : yDataG
41  zDataG = numtype(xDataG) == 2 ? NaN : zDataG
42  wavetransform zapnans xDataG
43  wavetransform zapnans yDataG
44  wavetransform zapnans zDataG

46  xDataR = xDataR < 5 ?  Nan : xDataR
47  xDataR = xDataR > (Stackdimensions[0]-5) ?  Nan : xDataR

49  yDataR = numtype(xDataR) == 2 ? NaN : yDataR
50  zDataR = numtype(xDataR) == 2 ? NaN : zDataR
51  wavetransform zapnans xDataR
52  wavetransform zapnans yDataR
53  wavetransform zapnans zDataR




58  yDataG = yDataG < 5?  Nan : yDataG
59  yDataG = yDataG > (Stackdimensions[1]-5) ?  Nan : yDataG

61  xDataG = numtype(yDataG) == 2 ? NaN : xDataG
62  zDataG = numtype(yDataG) == 2 ? NaN : zDataG
63  wavetransform zapnans xDataG
64  wavetransform zapnans yDataG
65  wavetransform zapnans zDataG
```

```
67  yDataR = yDataR < 5?  Nan : yDataR
68  yDataR = yDataR > (Stackdimensions[1]-5) ?  Nan : yDataR

70  xDataR = numtype(yDataR) == 2 ? NaN : xDataR
71  zDataR = numtype(yDataR) == 2 ? NaN : zDataR
72  wavetransform zapnans xDataR
73  wavetransform zapnans yDataR
74  wavetransform zapnans zDataR



78  zDataG = zDataG < 5 ?  Nan : zDataG
79  zDataG = zDataG > (Stackdimensions[2]-5) ?  Nan : zDataG

81  xDataG = numtype(zDataG) == 2 ? NaN : xDataG
82  yDataG = numtype(zDataG) == 2 ? NaN : yDataG
83  wavetransform zapnans xDataG
84  wavetransform zapnans yDataG
85  wavetransform zapnans zDataG

87  zDataR = zDataR < 5 ?  Nan : zDataR
88  zDataR = zDataR > (Stackdimensions[2]-5) ?  Nan : zDataR

90  xDataR = numtype(zDataR) == 2 ? NaN : xDataR
91  yDataR = numtype(zDataR) == 2 ? NaN : yDataR
92  wavetransform zapnans xDataR
93  wavetransform zapnans yDataR
94  wavetransform zapnans zDataR
95  //End Delte Border Line Particles


98  endif



102 if (TooManyParticles == 1)
103 //BEGIN PADDING FOR 1to1 SAMPLES
104 xDataG = xDataG > 100 ?  Nan : xDataG

106 yDataG = numtype(xDataG) == 2 ? NaN : yDataG
107 zDataG = numtype(xDataG) == 2 ? NaN : zDataG
108 wavetransform zapnans xDataG
109 wavetransform zapnans yDataG
110 wavetransform zapnans zDataG

112 xDatar = xDatar > 100 ?  Nan : xDatar

114 yDatar = numtype(xDatar) == 2 ? NaN : yDatar
115 zDatar = numtype(xDatar) == 2 ? NaN : zDatar
116 wavetransform zapnans xDatar
117 wavetransform zapnans yDatar
118 wavetransform zapnans zDatar


121 yDataG = yDataG > 100 ?  Nan : yDataG

123 xDataG = numtype(yDataG) == 2 ? NaN : xDataG
```

```
124   zDataG = numtype(yDataG) == 2 ? NaN : zDataG
125   wavetransform zapnans xDataG
126   wavetransform zapnans yDataG
127   wavetransform zapnans zDataG

129   yDatar = yDatar > 100 ?  Nan : yDatar

131   xDatar = numtype(yDatar) == 2 ? NaN : xDatar
132   zDatar = numtype(yDatar) == 2 ? NaN : zDatar
133   wavetransform zapnans xDatar
134   wavetransform zapnans yDatar
135   wavetransform zapnans zDatar
136   //END PADDING For 1to1 SAMPLES
137   endif

139   make/O/N=6 SizeAnalysedStack
140   SizeAnalysedStack[0] = StackDimensions[0]-5
141   SizeAnalysedStack[1] = StackDimensions[1]-5
142   SizeAnalysedStack[2] = StackDimensions[2]-5
143   //Calculate Analysed Volume
144   SizeAnalysedStack[3] = SizeAnalysedStack[0]*SizeAnalysedStack[1]*
          SizeAnalysedStack[2]
145   //Calculate Analysed Particle Density Majority Particles
146   SizeAnalysedStack[4] = dimsize(xdataR,0)/SizeAnalysedStack[3]
147   SizeAnalysedStack[5] = dimsize(xdataR,0)/dimsize(xdataG,0)



151   //Create Particle Waves with IDs
152   MakeWaves(xScale, yScale, zScale, "greenParticles_org", "redParticles_org")

154   // max. distance within which particles still belong to same cluster
155   wave greenParticles_org, redParticles_org                                  //wave
          with particle positions
156   variable a, b, c, i, j, k, n, p, q,  y
157   variable counterSpace, boolean,  sizecounter, waveSize, roundedWaveSize
158   variable clusterID = 1                                  //clusterID for wave
          greenParticles
159   variable sortedClusterID, maximumgreen                              // ClusterID for
          wave greenParticlesSorted
160   variable counter, counterRed, amountClusters
161   variable counter2 = 0
162   variable counterPosition

164   duplicate/O greenParticles_org greenParticles
165   duplicate/O redParticles_org redParticles

167   wave adjacencyMatrixGreen, adjacencyMatrixGreenRed

169   //Calculate the Adjacency Matrices
170   setupAdjacencyMatrices()

172   //Sort and identify Clusters
173   sortClusterIDs(bdgreen, bdgreenred)

175   //Delete all Clusters that are closer than 2um to the boundary
176   DeleteBoundaryClusters()
```

```
179   //Calculate the Clustersizes and other Statistics
180   Statistics()


183   end
184   ////////////////////////////////////
185   //END MAIN////////////////
186   ////////////////////////////////////
```

Listing A.2: IGOR PRO clustering algorithm, setupAdjacencyMatrices

```
1   ////////////////////////////////////////////////////
2   Function SetupAdjacencyMatrices()
3   ////////////////////////////////////////////////////
4   wave greenParticles, redParticles
5   variable a,b,c,i,j

7   //adjacencyMatrix GREEN PARTICLES
8   //setup adjacencyMatrix
9   Make /O/N=(dimsize(greenParticles, 0), dimsize(greenParticles, 0))
        adjacencyMatrixGreen

11  for (i = 0; i < dimsize(greenParticles, 0); i += 1)

13  for( j = 0; j < dimsize(greenParticles, 0); j += 1)

15  if(j <= i )                                    //use symmetry of the adjacencyMatrix

17  variable d                                  //distance between two particles
18  a = greenParticles[i][0] - greenParticles[j][0]
19  b = greenParticles[i][1] - greenParticles[j][1]
20  c = greenParticles[i][2] - greenParticles[j][2]
21  d = sqrt(a*a + b*b + c*c)                          //measures distance between two
        particles (in um!)

23  adjacencyMatrixGreen[i][j] = d

25  if(i != j)

27  adjacencyMatrixGreen[j][i] = adjacencyMatrixGreen[i][j]            //copy distance
         into the other diagonal

29  endif

31  endif


34  endfor

36  endfor

38  //adjacencyMatrix RED & GREEN Particles
39  //setup adjacencyMatrix
```

```
41  Make/O /N=(dimsize(redParticles, 0), dimsize(greenParticles, 0))
        adjacencyMatrixRedGreen

43  for (i = 0; i < dimsize(redParticles, 0); i += 1)

45  for( j = 0; j < dimsize(greenParticles, 0); j += 1)


48  variable dist                                   //distance between two particles
49  a = redParticles[i][0] - greenParticles[j][0]
50  b = redParticles[i][1] - greenParticles[j][1]
51  c = redParticles[i][2] - greenParticles[j][2]
52  dist = sqrt(a*a + b*b + c*c)                          //measures distance between two
        particles

54  adjacencyMatrixRedGreen[i][j] = dist

56  endfor

58  endfor


61  end
62  /////////END//////////////////////////////////////////////////////////////////
```

Listing A.3: IGOR PRO clustering algorithm, sortClusterIDs

```
1  ////////////////////////////////////////////////////////////////////////////
2  //sort clusters for distgg (maximum allowed distance between two green particles)
       and distgr (maximum allowed distance between red and green particle)
3  Function sortClusterIDs(distgg, distgr)
4  ////////////////////////////////////////////////////////////
5  variable distgg, distgr
6  wave greenParticles, redParticles, adjacencyMatrixGreen, adjacencyMatrixRedGreen
7  variable clusterID = 1
8  variable /G maximumgreen
9  variable i,j,k, sortedClusterID, counter


12 //start to give particles in same cluster the same clusterID  --- FOR GREEN
       PARTICLES
13 for ( i = 0; i < dimsize(greenParticles, 0); i += 1)

15 for( j = 0; j < dimsize(greenParticles, 0); j += 1)

17 if(greenParticles[i][3] == 0)                         // if particle isnt labeled yet
       , label it with new clusterID

19 greenParticles[i][3] = clusterID
20 clusterID += 1                                 //set ID to next number in order to can
       distinguish between different clusters

22 endif

24 if( adjacencyMatrixGreen [i][j] < distgg  && i != j)                  //look
       whether particle j is within distance bd to particle i
```

```
26 if(greenParticles [j][3] != 0)                    //if particle has already an ID
       , give all particles same ID as particle i

28 for(k = 0; k < dimsize(greenParticles, 0); k += 1)

30 if(greenParticles[k][3] == greenParticles[j][3] && j != K)

32 greenParticles[k][3] = greenParticles[i][3]

34 endif

36 endfor

38 endif

40 greenParticles[j][3] = greenParticles[i][3]          //give particle j same ID
       as particle i

42 endif

44 endfor

46 endfor


49 //labels red Particles with same cluster ID as greenParticle in direct vicinity
50 for (i=0; i<dimsize(redParticles,0); i+=1)
51 redParticles[i][3] = NaN
52 endfor

54 make/O/N=(dimsize(GreenParticles,0),4) SoleGreenParticles  //Wave for single Green
       PArticles
55 make/O/N=(dimsize(RedParticles,0),3)  SoleRedParticles  //Wave for single red
       particles
56 SoleRedParticles = NaN
57 SoleGreenParticles = NaN
58 variable tempID, dist

60 for(j = 0; j < dimsize(redParticles, 0); j += 1)

62 for(i = 0; i < dimsize(greenParticles,0); i += 1)

64 dist = adjacencyMatrixRedGreen[j][i]
65 if (dist <= distgr )

67 tempID = greenParticles[i][3]
68 redParticles[j][3] = tempID
69 break


72 else

74 endif

76 endfor
```

```
endfor


//Delete all red Particles with no Green in vicinity

//Save Rows with no Label to other wave and set to NaN
for (i=0; i<dimsize(redParticles,0); i+=1)
if (numtype(redParticles[i][3])==2)
SoleRedParticles[i][0] = redParticles[i][0]
SoleRedParticles[i][1] = redParticles[i][1]
SoleRedParticles[i][2] = redParticles[i][2]
redParticles[i][2] = NaN
redParticles[i][1] = NaN
redParticles[i][0] = NaN
endif
endfor

//Zapnans from MultiScale wave
ZapNaNsMultiScale("redParticles")
ZapNaNsMultiScale("SoleRedParticles")

//End Delete Red sole Particles

//Check on green Particles without green/red neighbour, set sole particles to nan
for (i=0; i<dimsize(greenParticles,0); i+=1)
counter = 0
for (j=0;j<dimsize(redParticles,0); j+=1)
if (greenParticles[i][3] == redParticles[j][3]) // && numtype(redParticles[j][3])
    == 0; I dont think I still need this part!
counter += 1
//Count number of red neighbours for label
endif
endfor

if ( (counter==0))// && (i != (dimsize(greenParticlessorted,0)-1)) && ((
    greenParticlesSorted[i][3] != greenParticlesSorted[i-1][3]) && (
    greenParticlesSorted[i][3] != greenParticlesSorted[i+1][3]))) //if no green and
     no red in vicinity, delete

SoleGreenParticles[i][0] = greenParticles[i][0]
SoleGreenParticles[i][1] = greenParticles[i][1]
SoleGreenParticles[i][2] = greenParticles[i][2]
SoleGreenParticles[i][3] = greenParticles[i][3]
GreenParticles[i][0] = NaN
GreenParticles[i][1] = NaN
GreenParticles[i][2] = NaN
GreenParticles[i][3] = NaN

endif
endfor

for (i=0; i<dimsize(greenParticles,0); i+=1)
if (numtype(greenParticles[i][3])==2)
greenParticles[i][2] = NaN
greenParticles[i][1] = NaN
greenParticles[i][0] = NaN
```

```
endif
endfor



//Zapnans from MultiScale wave
ZapNaNsMultiScale("SolegreenParticles")
ZapNaNsMultiScale("greenParticles")




//greenParticlesSorted
//sort greenParticles in right order by clusterIDs
Make/O /N=(dimsize(greenParticles, 0), 4) greenParticlesSorted            //here
    starts the sorting of greenParticles--> copy into new wave greenParticlesSorted

Make/O /N = (dimsize(greenParticles,0),1) xDataGtemp
Make/O /N = (dimsize(greenParticles,0),1) yDataGtemp
Make/O /N = (dimsize(greenParticles,0),1) zDataGtemp
Make/O /N = (dimsize(greenParticles,0),1) ID_Gtemp
for(i = 0; i < dimsize(greenParticles, 0); i += 1)
xDataGtemp[i] = greenParticles[i][0]
yDataGtemp [i]= greenParticles[i][1]
zDataGtemp [i] = greenParticles[i][2]
ID_Gtemp [i] = greenParticles[i][3]
endfor

Sort ID_Gtemp, ID_Gtemp, xDataGtemp, yDataGtemp, zDataGtemp

for(i = 0; i < dimsize(greenParticles, 0); i += 1)
greenParticlesSorted[i][0] = xDataGtemp [i]
greenParticlesSorted[i][1] = yDataGtemp [i]
greenParticlesSorted[i][2] = zDataGtemp [i]
greenParticlesSorted[i][3] = ID_Gtemp [i]
endfor

killwaves xDataGtemp, yDataGtemp, zDataGtemp, ID_Gtemp

Variable prevID
sortedClusterID = 1
for(i = 0; i < dimsize(greenParticlesSorted,0); i += 1)

if(i == dimsize(greenParticlesSorted,0)-2)
prevID = greenParticlesSorted[i][3]     //save pre-last clusterID
endif

if(i < (dimsize(greenParticlesSorted,0)-1) && greenParticlesSorted[i][3] ==
    greenParticlesSorted[i+1][3] )

greenParticlesSorted [i][3] = sortedClusterID

elseif(i < (dimsize(greenParticlesSorted,0)-1) && greenParticlesSorted[i][3] !=
    greenParticlesSorted[i+1][3] )
greenParticlesSorted [i][3] = sortedClusterID
sortedClusterID += 1
```

```
187 elseif(i == (dimsize(greenParticlesSorted,0)-1))
188 if(prevID== greenParticlesSorted[i][3])
189 greenParticlesSorted[i][3] = greenParticlesSorted[i-1][3]
190 else
191 greenParticlesSorted[i][3] = sortedClusterID
192 endif

194 endif

196 endfor



200 //redParticlesSorted
201 //sort redParticles in right order by clusterIDs
202 Make/O /N=(dimsize(redParticles, 0), 4) redParticlesSorted            //here starts
     the sorting of greenParticles--> copy into new wave greenParticlesSorted
203 redParticlesSorted = NaN
204 Make/O /N = (dimsize(redParticles,0)) xDataRtemp
205 Make/O /N = (dimsize(redParticles,0)) yDataRtemp
206 Make/O /N = (dimsize(redParticles,0)) zDataRtemp
207 Make/O /N = (dimsize(redParticles,0)) ID_Rtemp
208 xDataRtemp = NaN
209 yDataRtemp = NaN
210 zDataRtemp = NaN
211 ID_Rtemp = NaN

213 for(i = 0; i < dimsize(redParticles, 0); i += 1)
214 xDataRtemp[i] = redParticles[i][0]
215 yDataRtemp [i]= redParticles[i][1]
216 zDataRtemp [i] = redParticles[i][2]
217 ID_Rtemp[i] = redParticles[i][3]
218 endfor

220 Sort ID_Rtemp, ID_Rtemp, xDataRtemp, yDataRtemp, zDataRtemp

222 for(i = 0; i < dimsize(redParticles, 0); i += 1)
223 redParticlesSorted[i][0] = xDataRtemp [i]
224 redParticlesSorted[i][1] = yDataRtemp [i]
225 redParticlesSorted[i][2] = zDataRtemp [i]
226 redParticlesSorted[i][3] = ID_Rtemp [i]
227 endfor

229 killwaves xDataRtemp, yDataRtemp, zDataRtemp, ID_Rtemp



232 sortedClusterID = 1
233 for(i = 0; i < dimsize(redParticlesSorted,0); i += 1)

235 if(i == dimsize(redParticlesSorted,0)-2)
236 prevID = redParticlesSorted[i][3]     //save pre-last clusterID
237 endif

239 if(i < (dimsize(redParticlesSorted,0)-1) && redParticlesSorted[i][3] ==
    redParticlesSorted[i+1][3] )
```

```
redParticlesSorted [i][3] = sortedClusterID

elseif(i < (dimsize(redParticlesSorted,0)-1) && redParticlesSorted[i][3] !=
    redParticlesSorted[i+1][3] )
redParticlesSorted [i][3] = sortedClusterID
sortedClusterID += 1

elseif(i == (dimsize(redParticlesSorted,0)-1))
if(prevID== redParticlesSorted[i][3])
redParticlesSorted[i][3] = redParticlesSorted[i-1][3]
else
redParticlesSorted[i][3] = sortedClusterID
endif

endif

endfor

//Count Clusters
variable countergr,counterr
countergr=1
for (i=0; i<dimsize(greenParticlesSorted,0); i+=1)
if ( i != dimsize(greenParticlesSorted,0)-1 )
if (greenParticlesSorted[i][3] != greenParticlesSorted[i+1][3] )
countergr +=1
endif
endif
endfor


counterr=1
for (i=0; i<dimsize(redParticlesSorted,0); i+=1)
if ( i != dimsize(redParticlesSorted,0)-1)
if (redParticlesSorted[i][3] != redParticlesSorted[i+1][3] )
counterr +=1
endif
endif
endfor


if (countergr == counterr)
maximumgreen = countergr  //total amount of clusters
else
print "Frequency of Red and Green Cluster differ!"
abort
endif


end
////////END
    ////////////////////////////////////////////////////////////////////////////
```

Listing A.4: IGOR PRO clustering algorithm, statistics

```
////////////////////////////////////////////////////////////////////
Function Statistics()
////////////////////////////////////////////////////////////////////
```

```
4  variable /G maximumred, maximumgreen
5  variable counter, counterPosition, y,i
6  wave greenParticlesSorted, redParticlesSorted, soleRedParticles



10 maximumred = maximumgreen      //total amount of clusters

12 //clusterSizes - contents all clusters with size   --- GREEN PARTICLES
13 //count particles of each cluster and write it down
14 //makeWaveClustersCounted(greenParticles, greenParticlesSorted, maximum)   //this
       was old method name
15 Make/O /N=(maximumGreen) clusterSizesGreen
16 ClusterSizesGreen = NaN
17 duplicate/O clusterSizesGreen ClusterIDs
18 counter = 1
19 counterPosition = 0

21 for(y = 0; y < dimsize(greenParticlesSorted, 0); y += 1)


24 if(y != (dimsize(greenParticlesSorted,0)-1) && greenParticlesSorted[y][3] ==
       greenParticlesSorted[y+1][3] )      //if next clusterID is same as this, raise
        counter by one

26 counter += 1

28 elseif(y != (dimsize(greenParticlesSorted,0)-1) && greenParticlesSorted[y][3] !=
       greenParticlesSorted[y+1][3] )    //if next clusterID is not the same, write
       the size of the cluster into the wave

30 clusterSizesGreen[counterPosition] = counter
31 ClusterIDs[counterPosition] = greenParticlesSorted[y][3]
32 counter = 1                                  //reset counter
33 counterPosition += 1                          //go to next clusterID position

35 elseif((y == dimsize(greenParticlesSorted,0)-1) )
36 clusterSizesGreen[counterPosition] = counter
37 ClusterIDs[counterPosition] = greenParticlesSorted[y][3]
38 print counterposition
39 endif

41 endfor


44 //clusterSizes - contents all clusters with size   --- Red Particles
45 //count particles of each cluster and write it down

47 Make/O /N=(maximumRed) clusterSizesRed
48 ClusterSizesRed = NaN

50 counter = 1
51 counterPosition = 0

53 for(y = 0; y < dimsize(redParticlesSorted, 0); y += 1)
```

```
56  if(y != (dimsize(redParticlesSorted,0)-1) && redParticlesSorted[y][3] ==
        redParticlesSorted[y+1][3] )      //if next clusterID is same as this, raise
        counter by one

58  counter += 1

60  elseif(y != (dimsize(redParticlesSorted,0)-1) && redParticlesSorted[y][3] !=
        redParticlesSorted[y+1][3] )    //if next clusterID is not the same, write the
         size of the cluster into the wave

62  clusterSizesred[counterPosition] = counter

64  counter = 1                                 //reset counter
65  counterPosition += 1                          //go to next clusterID position

67  elseif(y == dimsize(redParticlesSorted,0)-1 )
68  clusterSizesred[counterPosition] = counter

70  endif

72  endfor









79  //Add up Clustersizes
80  Make/O /N=(dimsize(clusterSizesGreen,0)) clusterSizesSum

82  for(i = 0; i < dimsize(clusterSizesSum,0); i += 1)

84  clusterSizesSum [i] = clusterSizesRed[i] + clusterSizesGreen[i]

86  endfor


89  //Create wave with all Particle coordinates, sorted by IDs
90  AddUpClusters()

92  //Calculate MassCenters and Radii of Gyration
93  Gyration_FH()

95  //Make Clusterdistributions for different number of minority particles
96  Analyse_Clusterdistr()

98  //Find MaxDiameters
99  FindMaxDiameter()




104 //Make Clustersize Histogram
105 Make/N=50/O clusterSizesSum_Hist;
106 Histogram/C/B={0,2,50} clusterSizesSum,clusterSizesSum_Hist
107 clustersizessum_hist /= numpnts(clustersizessum)
```

```
111 make/O/N=(5,2) info
112 setdimlabel 0,0,NumberAverage,info
113 setdimlabel 0,1,MaxMin,info
114 setdimlabel 0,2,freeRed,info
115 setdimlabel 0,3,freeGreen,info
116 setdimlabel 0,4,MassAverage,info
117 info = NAN
118 wave solegreenparticles
119 //Determine average and max cluster size
120 wavestats/Q clustersizessum
121 info[0][0] = V_avg
122 info[0][1] = V_sdev
123 info[1][0] = V_max
124 info[1][1] = V_min

126 //Calculate "Massenmittel"
127 variable Zaehler,Nenner, Massenmittel

129 Zaehler = 0
130 Nenner = 0
131 for (i=0;i<dimsize(clustersizessum,0);i+=1)
132 Zaehler += clustersizessum[i]^2
133 Nenner += clustersizessum[i]
134 endfor
135 Massenmittel = Zaehler/Nenner


138 wavestats/Q soleredparticles
139 info[2][0] = V_npnts/3
140 wavestats/Q redparticlessorted
141 info[2][1] = info[2][0]/((V_npnts/4)+info[2][0])
142 if (dimsize(solegreenParticles,0)>0) //Only calculate oif there are sole green
    particles
143 wavestats/Q solegreenparticles
144 info[3][0] = V_npnts/4
145 wavestats/Q greenparticlessorted
146 info[3][1] = info[3][0]/((V_npnts/4)+info[3][0])
147 endif
148 info[4][0] = Massenmittel
149 end

151 ///////////////END
    ////////////////////////////////////////////////////////////////////////////
```

A.3. List of publications

- Fabian M. Hecht, Andreas R. Bausch (2016) Kinetically guided colloidal structure formation, *Proceedings of the national academy of sciences of the United States of America*, 113(31), 8577-8592, doi: 10.1073/pnas.1605114113
- Joanna Deek, F. M. Hecht, L. Rossetti, K. Wißmiller, A.R. Bausch (2016) Mechanics of soft epithelial keratin networks depend on modular filament assembly kinetics, *Acta Biometrialia*, 43, 218-229, doi:10.1016/j.actbio.2016.07.010

List of Figures

2.1. Fractals in theory and experiment 4
2.2. Comparison of DLCA and RLCA 6
2.3. Principle of structure formation by DNA coated colloids 10
2.4. Examples for structures self-assembled with micron sized DNA coated colloids 11
2.5. Overview of biochemical reaction networks 13
2.6. Transient structure formation 14
2.7. Schematic of the static structure formation processes investigated in this thesis 17
2.8. Schematic of the dynamic structure formation processes investigated in this thesis 18

3.1. Monodispersity and sedimentation 23
3.2. Graphical User Interface (GUI) for the Matlab particle counting algorithm . 25
3.3. Connectivity-based clustering algorithm 26
3.4. Fractal analysis of gels and clusters 27
3.5. Storage modulus measured during PAM polymerization 30
3.6. Acryl-glass mold for 3D hybrid-gel molding 31
3.7. Fluorescence signal calibration for RNA detection 33
3.8. Native polyacrylamide gelectrophoresis (PAGE) 34

4.1. Morphological comparsion of different fractal gels formed by a binary system of DNA coated colloids 36
4.2. Controlling the cluster size in a binary heterocoagulation experiment 38
4.3. Geometrical classification of binary heterocoagulates into three regimes . . 39
4.4. Time evolution in binary heterocoagulation for different $X_{\alpha-\beta}$ 40
4.5. Time evolution of different key parameters of binary heterocoagulation . . 42
4.6. Analytic model for binary heterocoagulation at high stoichiometries 44
4.7. Ternary aggregation of equally sized microspheres in the compact regime . 46
4.8. Ternary aggregation of differently sized microspheres 47
4.9. Hierarchical 5-component heterocoagulation process 49
4.10. 90°-light scattering on binary microsphere coagulates 50

4.11. Elasticity of hybrid polymer-DNA coated colloid gels 52
4.12. Toughness of hybdrid polymer-DNAcc gels 53
4.13. Printing and 3D molding of hybrid polymer-DNA coated colloid gels 54
4.14. Binary heterocoagulation of 10 nm sized gold nanoparticles on different scales for different stoichiometries $X_{\alpha-\beta}$ 55
4.15. Extinction spectra of nanoparticle clusters for different stoichiometries $X_{\alpha-\beta}$ 56
4.16. Comparison of experimental and simulation data for binary heterocoagulation at $X_{\alpha-\beta} = 18$ 58

5.1. Fluorescence bulk measurements of RNA polymerization by T7 RNA polymerase 60
5.2. Quantity and specificity of RNA production by T7 RNA polymerase 62
5.3. RNA degradation by RNAseH 65
5.4. RNA pulse generation by T7 RNA polymerase and RNAseH 67
5.5. Coagulation of DNA coated colloids induced by RNA 68
5.6. Time course measurements of DNA coated colloid coagulation caused by RNA production of T7 RNA polymerase 69
5.7. Disintegration of pre-formed DNAcc clusters linked by RNA-DNA duplexes 71
5.8. Transient structure formation of DNA coated colloids by T7 RNA polymerase and RNAseH 73
5.9. Temperature switchable structure formation by DNA coated colloids 75

A.1. Polymerization of RNA by T7 RNA polymerase i

Bibliography

[1] Schroeder, M. R. (2009). (Dover Publications, Mineola, N.Y.), Dover ed. edition. 2.1.1.1, 2.1.1.1, 3.1.1.5

[2] Brieskorn, E. (1996). (Vieweg, Braunschweig/Wiesbaden). 2.1.1.1

[3] Mandelbrot, B. (1967) *Science (New York, N.Y.)* 156, 636–638. 2.1.1.1, 2.1

[4] Mashiah, A, Wolach, O, Sandbank, J, Uziel, O, Raanani, P, & Lahav, M. (2008) *Acta haematologica* 119, 142–150. 2.1.1.1

[5] Dokukin, M. E, Guz, N. V, Woodworth, C. D, & Sokolov, I. (2015) *New journal of physics* 17, 033019. 2.1.1.1

[6] Lieleg, O, Schmoller, K. M, Cyron, C. J, Luan, Y, Wall, W. A, & Bausch, A. R. (2009) *Soft Matter* 5, 1796–1803. 2.1.1.1

[7] Pourahmadazar, J, Ghobadi, C, & Nourinia, J. (2011) *IEEE Antennas and Wireless Propagation Letters* 10, 484–487. 2.1.1.1

[8] Losa, G. A, Merlini, D, Nonnenmacher, T. F, & Weibel, E. R. (2005). (Birkhäuser Verlag Basel, Basel). 2.1.1.1

[9] S R Forrest & T A Witten Jr. (1979) *Journal of Physics A: Mathematical and General* 12, L109. 2.1.1.1

[10] T. A. Witten, Jr. and L. M. Sander. (1981) *Physical review letters* 47, 1400–1403. 2.1.1.1

[11] Weitz, D. A & Oliveria, M. (1984) *Physical Review Letters* 52, 1433–1436. 2.1.1.1, 2.1.1.2

[12] Mandelbrot, B. B. (1977). (Freeman, New York). 2.1.1.1

[13] Sorensen, C. M. (2011) *Aerosol Science and Technology* 45, 765–779. 2.1.1.2, 2.1.1.2, **??**, 3.1.1.5

[14] Schaefer, D. W, Martin, J. E, Wiltzius, P, & Cannell, D. S. (1984) *Physical Review Letters* 52, 2371–2374. 2.1.1.2

[15] Family, F & Landau, D. P. (1984). (Elsevier Science, Oxford). 2.1.1.2

[16] Martin, J. E & Hurd, A. J. (1987) *Journal of Applied Crystallography* 20, 61–78. 2.1.1.2

[17] Dobbins, R. A & Megaridis, C. M. (1987) *Langmuir* 3, 254–259. 2.1.1.2

[18] Vicsek, T. (1992). (World Scientific, Singapore and New Jersey), 2nd ed. edition. 2.1.1.2

[19] Lattuada, M, Wu, H, Hasmy, A, & Morbidelli, M. (2003) *Langmuir* 19, 6312–6316. 2.1.1.2

[20] Gimel, J. C, Nicolai, T, & Durand, D. (1999) *Journal of Sol-Gel Science and Technology* 15, 129–136. 2.1.1.2

[21] Hasmy, A, Foret, M, Anglaret, E, Pelous, J, Vacher, R, & Jullien, R. (1995) *Journal of Non-Crystalline Solids* 186, 118–130. 2.1.1.2

[22] Derjaguin, B. V & Landau, L. (1941) *Acta physicochim. URSS* 1941, 633. 2.1.1.2

[23] Verwey, E & Overbeek, J. T. G. (1948) *Elsevier*. 2.1.1.2

[24] Lin, M. Y. (1990) *Physical Review A* 41, 2005–2020. 2.1.1.2, **??**

[25] Sorensen, C. M & Chakrabarti, A. (2011) *Soft Matter* 7, 2284. 2.1.1.2, 2.1.1.2, **??**

[26] D. A. Weitz, J. S. Huang, M. Y. Lin, and J. Sung. (1985) *Physical review letters* 54, 1416–1419. 2.2

[27] Meakin, P. (1992) *Physica Scripta* 46, 295. 2.1.1.2

[28] Stauffer, D & Aharony, A. (1994). (CRC press). 2.1.1.2

[29] Weitz, D. A, Huang, J. S, Lin, M. Y, & Sung, J. (1984) *Physical Review Letters* 53, 1657–1660. 2.1.1.2, 4.1.1

[30] Rottereau, M, Gimel, J. C, Nicolai, T, & Durand, D. (2004) *The European Physical Journal E* 15, 141–148. 2.1.1.2, 4.1.1

[31] Lach-hab, M, González, A. E, & Blaisten-Barojas, E. (1998) *Phys. Rev. E* 57, 4520–4527. 2.1.1.2

[32] Lattuada, M, Wu, H, Hasmy, A, & Morbidelli, M. (2003) *Langmuir* 19, 6312–6316. 2.1.1.2

[33] Puertas, A. M, Fernández-Barbero, A, & De las Nieves, F. J. (2000) in *Trends in Colloid and Interface Science XIV*, ed. Buckin, V. (Springer Berlin Heidelberg, Berlin, Heidelberg), pp. 55–58. 2.1.1.2, 2.1.2

[34] Kim, A. Y, Hauch, K. D, Berg, J. C, Martin, J. E, & Anderson, R. A. (2003) *Journal of Colloid and Interface Science* 260, 149–159. 2.1.1.2

[35] López-López, J. M, Schmitt, A, Moncho-Jordá, A, & Hidalgo-Álvarez, R. (2006) *Soft Matter* 2, 1025–1042. **??**, 2.1.2, 3.1.1.5

[36] Rottereau, M, Gimel, J. C, Nicolai, T, & Durand, D. (2004) *The European Physical Journal E* 15, 133–140. **??**

[37] Sorensen, C. M. (2001) *Aerosol Science and Technology* 35, 648–687. **??**, 3.1.1.5

[38] M. v. Smoluchowski. (1916) *Zeitschrif für physikalische Chemie*. 2.1.2, 4.1.2, 4.1.4

[39] Islam, A. M, Chowdhry, B. Z, & Snowden, M. J. (1995) *Advances in colloid and interface science* 62, 109–136. 2.1.2

[40] Meakin, P & Djordjevic, Z. B. (1986) *Journal of Physics A: Mathematical and General* 19, 2137. 2.1.2

[41] AlSunaidi, A, Lach-hab, M, González, A. E, & Blaisten-Barojas, E. (2000) *Physical Review E* 61, 550–556. 2.1.2

[42] Hogg, R, Healy, T. W, & Fuerstenau, D. W. (1966) *Transactions of the Faraday Society* 62, 1638. 2.1.2

[43] Maroto, J. A & de las Nieves, F. J. (1998) *Colloids and Surfaces A: Physicochemical and Engineering Aspects* 132, 153–158. 2.1.2

[44] Yu, W. L & Borkovec, M. (2002) *The Journal of Physical Chemistry B* 106, 13106–13110. 2.1.2

[45] Watson, J. D & Crick, F. (1953) *Nature* 171, 737–738. 2.3, 2.2

[46] Valignat, M.-P, Theodoly, O, Crocker, J. C, Russel, W. B, & Chaikin, P. M. (2005) *Proceedings of the National Academy of Sciences of the United States of America* 102, 4225–4229. 2.3, 2.2

[47] Di Michele, L & Eiser, E. (2013) *Physical Chemistry Chemical Physics* 15, 3115. 2.2

[48] Alivisatos, A. P, Johnsson, K. P, Peng, X, Wilson, T. E, Loweth, C. J, Bruchez, JR, M. P, & Schultz, P. G. (1996) *Nature* 382, 609–611. 2.2

[49] Mirkin, C. A, Letsinger, R. L, Mucic, R. C, & Storhoff, J. J. (1996) *Nature* 382, 607–609. 2.2, 2.2

[50] Lee, J, Hernandez, P, Lee, J, Govorov, A. O, & Kotov, N. A. (2007) *Nature Materials* 6, 291–295. 2.2, 4.5

[51] Redl, F. X, Cho, K.-S, Murray, C. B, & O'Brien, S. (2003) *Nature* 423, 968–971. 2.2

[52] Urban, J. J, Talapin, D. V, Shevchenko, E. V, Kagan, C. R, & Murray, C. B. (2007) *Nature Materials* 6, 115–121. 2.2

[53] Simmel, F. C. (2013) *Chemie in unserer Zeit* 47, 164–173. 2.2

[54] Di Michele, L, Varrato, F, Kotar, J, Nathan, S. H, Foffi, G, & Eiser, E. (2013) *Nature Communications* 4, 2007. 2.4

[55] Wang, Y, Zheng, X, Ducrot, E, Yodh, J. S, Weck, M, & Pine, D. J. (2015) *Nature communications* 6, 7253. 2.4, 2.2

[56] Wang, Y, Wang, Y, Breed, D. R, Manoharan, V. N, Feng, L, Hollingsworth, A. D, Weck, M, & Pine, D. J. (2012) *Nature* 491, 51–55. 2.4, 2.2

[57] McGinley, J. T, Jenkins, I, Sinno, T, & Crocker, J. C. (2013) *Soft Matter* 9, 9119. 2.4, 2.2

[58] Pal, S, Deng, Z, Ding, B, Yan, H, & Liu, Y. (2010) *Angewandte Chemie* 122, 2760–2764. 2.2

[59] Thompson, D. G, Enright, A, Faulds, K, Smith, W. E, & Graham, D. (2008) *Analytical chemistry* 80, 2805–2810. 2.2

[60] Biancaniello, P, Kim, A, & Crocker, J. (2005) *Physical Review Letters* 94. 2.2

[61] Dreyfus, R, Leunissen, M. E, Sha, R, Tkachenko, A, Seeman, N. C, Pine, D. J, & Chaikin, P. M. (2010) *Physical review. E, Statistical, nonlinear, and soft matter physics* 81, 041404. 2.2

[62] Rogers, W. B & Crocker, J. C. (2011) *Proceedings of the National Academy of Sciences* 108, 15687–15692. 2.2

[63] Rogers, W. B & Crocker, J. C. (2011) *Proceedings of the National Academy of Sciences* 108, 15687–15692. 2.2

[64] Kim, A. J, Biancaniello, P. L, & Crocker, J. C. (2006) *Langmuir* 22, 1991–2001. 2.2

[65] Park, S. Y, Lytton-Jean, Abigail K. R., Lee, B, Weigand, S, Schatz, G. C, & Mirkin, C. A. (2008) *Nature* 451, 553–556. 2.2

[66] Nykypanchuk, D, Maye, M. M, van der Lelie, Daniel, & Gang, O. (2008) *Nature* 451, 549–552. 2.2

[67] Zhabotinsky, A. M. (1964) *Biofizika* 1964, 306–311. 2.3.1

[68] Kim, J & Winfree, E. (2011) *Molecular Systems Biology* 7. 2.3.1, 2.3.1, 2.5, 2.3.3, 5.4

[69] Panda, S, Hogenesch, J. B, & Kay, S. A. (2002) *Nature* 417, 329–335. 2.3.1, 2.5

[70] Nakajima, M, Imai, K, Ito, H, Nishiwaki, T, Murayama, Y, Iwasaki, H, Oyama, T, & Kondo, T. (2005) *Science* 308, 414–415. 2.3.1, 2.5

[71] Mori, T, Williams, D. R, Byrne, M. O, Qin, X, Egli, M, Mchaourab, H. S, Stewart, P. L, & Johnson, C. H. (2007) *PLoS Biol* 5, e93. 2.3.1

[72] Elowitz, M. B & Leibler, S. (2000) *Nature* 403, 335–338. 2.3.1, 2.5

[73] Atkinson, M. R, Savageau, M. A, Myers, J. T, & Ninfa, A. J. (2003) *Cell* 113, 597–607. 2.3.1

[74] Stricker, J, Cookson, S, Bennett, M. R, Mather, W. H, Tsimring, L. S, & Hasty, J. (2008) *Nature* 456, 516–519. 2.3.1

[75] Wlotzka, B & McCaskill, J. S. (1997) *Chemistry & Biology* 4, 25–33. 2.3.1

[76] Seelig, G, Soloveichik, D, Zhang, D. Y, & Winfree, E. (2006) *Science (New York, N.Y.)* 314, 1585–1588. 2.3.1

[77] Zhang, D. Y, Turberfield, A. J, Yurke, B, & Winfree, E. (2007) *Science (New York, N.Y.)* 318, 1121–1125. 2.3.1

[78] Montagne, K, Plasson, R, Sakai, Y, Fujii, T, & Rondelez, Y. (2011) *Molecular Systems Biology* 7. 2.3.1, 5.4

[79] Takinoue, M, Kiga, D, Shohda, K.-I, & Suyama, A. (2008) *Physical review. E, Statistical, nonlinear, and soft matter physics* 78, 041921. 2.3.1, 5.4

[80] Noireaux, V, Bar-Ziv, R, & Libchaber, A. (2003) *Proceedings of the National Academy of Sciences of the United States of America* 100, 12672–12677. 2.3.1

[81] Ackermann, J, Wlotzka, B, & McCaskill, J. S. (1998) *Bulletin of Mathematical Biology* 60, 329–354. 2.3.1

[82] Simpson, Z. B, Tsai, T. L, Nguyen, N, Chen, X, & Ellington, A. D. (2009) *Journal of the Royal Society, Interface / the Royal Society* 6 Suppl 4, S523–33. 2.3.1

[83] Takinoue, M, Kiga, D, Shohda, K.-I, & Suyama, A. (2009) *New Generation Computing* 27, 107–127. 2.3.1, 2.3.2

[84] Reusser, E. J & Field, R. J. (1979) *Journal of the American Chemical Society* 101, 1063–1071. 2.3.1

[85] Loose, M, Fischer-Friedrich, E, Ries, J, Kruse, K, & Schwille, P. (2008) *Science* 320, 789–792. 2.3.1

[86] Chang, J. B & Ferrell, JR, J. E. (2013) *Nature* 500, 603–607. 2.3.1

[87] Schnakenberg, J. (1978) *Berichte der Bunsengesellschaft für physikalische Chemie* 82, 672. 2.3.1

[88] Cross, M. C & Hohenberg, P. C. (1993) *Reviews of Modern Physics* 65, 851–1112. 2.3.1

[89] Caudron, M, Bunt, G, Bastiaens, P, & Karsenti, E. (2005) *Science* 309, 1373–1376. 2.3.1

[90] Karsenti, E. (2008) *Nat Rev Mol Cell Biol* 9, 255–262. 2.3.1

[91] Kondo, S. (2002) *Genes to Cells* 7, 535–541. 2.3.1

[92] Boekhoven, J, Hendriksen, W. E, Koper, G. J. M, Eelkema, R, & van Esch, J. H. (2015) *Science (New York, N.Y.)* 349, 1075–1079. 2.6, 2.3.2, 5.4

[93] Fialkowski, M, Bishop, Kyle J. M., Klajn, R, Smoukov, S. K, Campbell, C. J, & Grzybowski, B. A. (2006) *The journal of physical chemistry. B* 110, 2482–2496. 2.3.2

[94] Liedl, T & Simmel, F. C. (2005) *Nano Lett* 5, 1894–1898. 2.3.2

[95] Yurke, B, Turberfield, A. J, Mills, A. P, Simmel, F. C, & Neumann, J. L. (2000) *Nature* 406, 605–608. 2.3.2

[96] Dittmer, W. U, Kempter, S, Rädler, J. O, & Simmel, F. C. (2005) *Small* 1, 709–712. 2.3.2

[97] Dittmer, W. U & Simmel, F. C. (2004) *Nano Lett* 4, 689–691. 2.3.2

[98] Zhang, D. Y, Hariadi, R. F, Choi, H. M. T, & Winfree, E. (2013) *Nature communications* 4, 1965. 2.3.2

[99] von Maltzahn, G, Min, D.-H, ZHANG, Y, Park, J.-H, Harris, T. J, Sailor, M, & Bhatia, S. N. (2007) *Advanced Materials* 19, 3579–3583. 2.3.2

[100] Lagzi, I, Kowalczyk, B, Wang, D, & Grzybowski, B. A. (2010) *Angewandte Chemie (International ed. in English)* 49, 8616–8619. 2.3.2

[101] Sousa, R & Mukherjee, S. (2003) in *Progress in Nucleic Acid Research and Molecular Biology*, Progress in Nucleic Acid Research and Molecular Biology, ed. Moldave, K. (Elsevier textbooks, s.l.) Vol. 73, pp. 1–41. 2.3.3

[102] Chen, Y. C & Jeng, S. T. (2000) *Bioscience, biotechnology, and biochemistry* 64, 1126–1132. 2.3.3

[103] Anand, V. S & Patel, S. S. (2006) *The Journal of biological chemistry* 281, 35677–35685. 2.3.3, 2.3.3

[104] Martin, C. T, Esposito, E. A, Theis, K, & Gong, P. (2005) in *Progress in nucleic acid research and molecular biology*, Progress in Nucleic Acid Research and Molecular Biology, ed. Moldave, K. (Academic Press, S.l.) Vol. 80, pp. 323–347. 2.3.3

[105] Hogrefe, H. H, Hogrefe, R. I, Walder, R. Y, & Walder, J. A. (1990) *Journal of Biological Chemistry* 265, 5561–5566. 2.3.3

[106] Kanaya, S & Crouch, R. J. (1983) *Journal of Biological Chemistry* 258, 1276–1281. 2.3.3

[107] Berkower, I, Leis, J, & Hurwitz, J. (1973) *Journal of Biological Chemistry* 248, 5914–5921. 2.3.3

[108] Karwan, R, Blutsch, H, & Wintersberger, U. (1983) *Biochemistry* 22, 5500–5507. 2.3.3

[109] Karwan, R & Wintersberger, U. (1988) *Journal of Biological Chemistry* 263, 14970–14977. 2.3.3

[110] Dobosy, J. R, Rose, S. D, Beltz, K. R, Rupp, S. M, Powers, K. M, Behlke, M. A, & Walder, J. A. (2011) *BMC biotechnology* 11, 80. 2.3.3

[111] Loo, J. F. C, Wang, S. S, Peng, F, He, J. A, He, L, Guo, Y. C, Gu, D. Y, Kwok, H. C, Wu, S. Y, Ho, H. P, Xie, W. D, Shao, Y. H, & Kong, S. K. (2015) *The Analyst* 140, 4566–4575. 2.3.3

[112] Michaelis, L, Menten, M. L, Johnson, K. A, & Goody, R. S. (2011) *Biochemistry* 50, 8264–8269. 2.3.3

[113] Biancaniello, P. L, Crocker, J. C, Hammer, D. A, & Milam, V. T. (2007) *Langmuir* 23, 2688–2693. 2.4

[114] Zadeh, J. N, Steenberg, C. D, Bois, J. S, Wolfe, B. R, Pierce, M. B, Khan, A. R, Dirks, R. M, & Pierce, N. A. (2011) *Journal of computational chemistry* 32, 170–173. 3.1.1.1

[115] Zhou, X, Zhu, D, Liao, Y, Liu, W, Liu, H, Ma, Z, & Xing, D. (2014) *Nature Protocols* 9, 1146–1159. 3.1.1.2

[116] Dinsmore, A. D, Weeks, E. R, Prasad, V, Levitt, A. C, & Weitz, D. A. (2001) *Applied Optics* 40, 4152. 3.1.1.5

[117] Crocker, J. C & Grier, D. G. (1996) *Journal of Colloid and Interface Science* 179, 298–310. 3.1.1.5

[118] Gao, Y & Kilfoil, M. L. (2009) *Optics Express* 17, 4685. 3.1.1.5

[119] cytodiagnostics. (2017) Gold nanoparicle properties. 3.1.2.1

[120] Thompson, R. F, Walker, M, Siebert, C. A, Muench, S. P, & Ranson, N. A. (2016) *Methods (San Diego, Calif.)* 100, 3–15. 3.1.2.4

[121] Rubinstein, M & Colby, R. H. (2010). (Oxford Univ. Press, Oxford), Reprinted. edition. 3.1.3.1

[122] Hecht, F. M & Bausch, A. R. (2016) *Proceedings of the National Academy of Sciences of the United States of America* 113, 8577–8582. 4

[123] Stanley, H. E & Meakin, P. (1988) *Nature* 335, 405–409. 4.1.3

[124] Langmuir, I. (1918) *Journal of the American Chemical Society* 40, 1361–1403. 4.1.4

[125] Gaster, R. S, Xu, L, Han, S.-J, Wilson, R. J, Hall, D. A, Osterfeld, S. J, Yu, H, & Wang, S. X. (2011) *Nature Nanotechnology* 6, 314–320. 4.1.4, 4.1.4

[126] Cussler, E. L. (2009). (Cambridge University Press, Cambridge and New York), 3rd ed. edition. 4.1.4

[127] Deutch, J. M. (1973) *The Journal of Chemical Physics* 59, 1669. 4.1.4

[128] Mie, G. (1908) *Annalen der Physik* 330, 377–445. 4.4.1, 4.4.3

[129] Witten, T. A, Rubinstein, M, & Colby, R. H. (1993) *Journal de Physique II* 3, 367–383. 4.4.2

[130] Qin, K & Zaman, A. A. (2003) *Journal of Colloid and Interface Science* 266, 461–467. 4.4.2

[131] Benedikt Buchmann. (09/2016) Masterarbeit (Technische Universität München, Garching). 4.4.3

[132] Jacobs, W. M, Reinhardt, A, & Frenkel, D. (2015) *Proceedings of the National Academy of Sciences* 112, 6313–6318. 4.5

[133] Wei, B, Dai, M, & Yin, P. (2012) *Nature* 485, 623–626. 4.5

[134] Ke, Y, Ong, L. L, Shih, W. M, & Yin, P. (2012) *Science* 338, 1177–1183. 4.5

[135] Timo Krüger. (2015) Masterarbeit (Ludwig-Maximilians-Universität München, München). 4.5, 4.16

[136] Tikhomirov, G, Hoogland, S, Lee, P. E, Fischer, A, Sargent, E. H, & Kelley, S. O. (2011) *Nature Nanotechnology* 6, 485–490. 4.5

[137] Liu, J & Lu, Y. (2006) *Advanced Materials* 18, 1667–1671. 4.5

[138] Peterson, M. E, Daniel, R. M, Danson, M. J, & Eisenthal, R. (2007) *The Biochemical journal* 402, 331–337. 5.1.1.1

[139] Martin, C. T, Muller, D. K, & Coleman, J. E. (1988) *Biochemistry* 27, 3966–3974. 5.1.1.1

[140] Mathews, C. K, van Holde, K. E, & Ahern, K. G. (2000). (Benjamin Cummings, San Francisco, Calif.), 3rd ed. edition. 5.1.2